GPO PRICE $ _____

CFSTI PRICE(S) $ _____

Hard copy (HC) 4.00

Microfiche (MF) 1.00

ff 653 July 65

FACILITY FORM 602

N66-13000 (ACCESSION NUMBER)

149 (PAGES)

CR-68374 (NASA CR OR TMX OR AD NUMBER)

1 (THRU)

(CODE)

28 (CATEGORY)

SOLAR-POWERED ELECTRIC PROPULSION SPACECRAFT

BI-MONTHLY REPORT

NO. 3

HUGHES AIRCRAFT COMPANY
SPACE SYSTEMS DIVISION

J. H. Molitor for
Robert H. Stivers
Program Manager, Electric
Propulsion Program Office

Prepared for JPL under
Contract No. 951144
under NAS 7-100
September 1965

TABLE OF CONTENTS

INTRODUCTION

This is the third Bi-Monthly Report issued under Contract Number 951144 with the Jet Propulsion Laboratory. It is a report of the progress occurring during the month of July and August 1965.

Spacecraft design concept shown herein reflect the non-deployable engine array as stipulated by JPL. Low thrust mission analysis have been extended to include fly-by heliocentric transfer trajectory from 1971 to 1975.

There was an interim report on Power Conditioning and Control issued July 1965.

The next report will be the final report and will include a reliability and cost comparison between the final electric propulsion spacecraft and an all-chemical spacecraft.

II. TECHNICAL DISCUSSION

A. MISSION ANALYSIS

The main objective of the mission is to deliver a scientifie payload and a reliable telecommunications system into an orbit around the planet Mars. Such a delivery can be accomplished by either an all chemical system or by use of a solar electric powered final stage spacecraft. The purpose then to be fulfilled in this study is a comparison of the chemical and the solar electric mission within the constraints stipulated by the contracting agency.

1. Solar Electric Spacecraft Performance Analysis

As pointed out in the 1st Bimonthly Report, the purpose of the low thrust mission studies is to (1) determine the payload capability of an electrically propelled spacecraft and subsequently compare it to an all chemical vehicle and (2) establish the optimum design points for the propulsion system. It was also stated that although the total mission objective was a Mars Orbiter, the specific role which the ion propulsion system will play in accomplishing this objective must still be decided. The various possible mission profiles for the ion propulsion stage are Optimum Coast Rendezvous, Zero Coast Rendezvous, Minimum Time Flyby, and Flyby. Each of these mission profiles were to be studied for effects of departure date, launch year, hyperbolic excess, flight time, specific impulse, and thrust orientation.

During the first reporting period, the mission analysis was limited to the zero coast rendezvous mission and primarily to the 1971 launch year so that the propulsion and spacecraft system designs could proceed. The 350 day, 1971, zero coast rendezvous profile was chosen as the design model mission. The results of these analyses established the following design points for an electrically propelled spacecraft launched by a SATURN IB/CENTAUR:

1. Hg Bombardment Engine
2. Specific Impulse - 4000 sec.
3. Power Requirement - 48 kW
4. Propellant Weight - 1600 lbs.
5. Thrust Vector thru 50^{o}

The results of an equivalent analysis considering an ATLAS/CENTAUR launch vehicle is shown in Fig. A.1-1. The optimized propulsion system design points for the 400 day, 1971, zero coast rendezvous profile are:

1. Hg Bombardment Engine
2. Specific Impulse - 3800 sec.
3. Power Requirement - 8.5 kW
4. Propellant Weight - 360 lbs.
5. Thrust Vector thru 12^{o}

For this particular mission a payload (i.e., initial weight at Earth escape minus propellent and complete propulsion system) greater than 62% of the initial spacecraft weight (or 1580 lbs) would be placed into some elliptical capture orbit about Mars.

In the 2nd Bimonthly Report the mission analyses were extended to include the Optimum Coast, Zero Coast, and Flyby mission profiles for the launch years of 1969, 1971, 1973, 1975, and 1977. These missions (with a few exceptions) were studied under the following conditions:

1. Departure Date - determine optimum and effect of launch window.
2. Hyperbolic Excess - zero.
3. Flight Time - 150 days to 500 days.
4. Specific Impulse - 3000 sec to 6000 sec.
5. Thrust Orientation - optimum.

The results of these analyses, which were obtained as a direct output of the JPL low thrust variable power trajectory program, were presented in the form of performance maps for low acceleration, high specific impulse propulsion systems. The use of these maps has been described in the 1st Bimonthly Report and will not be repeated here. However, as stated, these data are completely independent of propulsion system constraints and can be used to evaluate the effectiveness of any low thrust device.

These trajectory data have been used to determine the payload capability of ion propulsion systems and their optimum design points. In the 2nd Bimonthly Report the results of an analysis of the zero coast rendezvous missions were given. A similar analysis of the flyby missions has been completed and will be presented here.

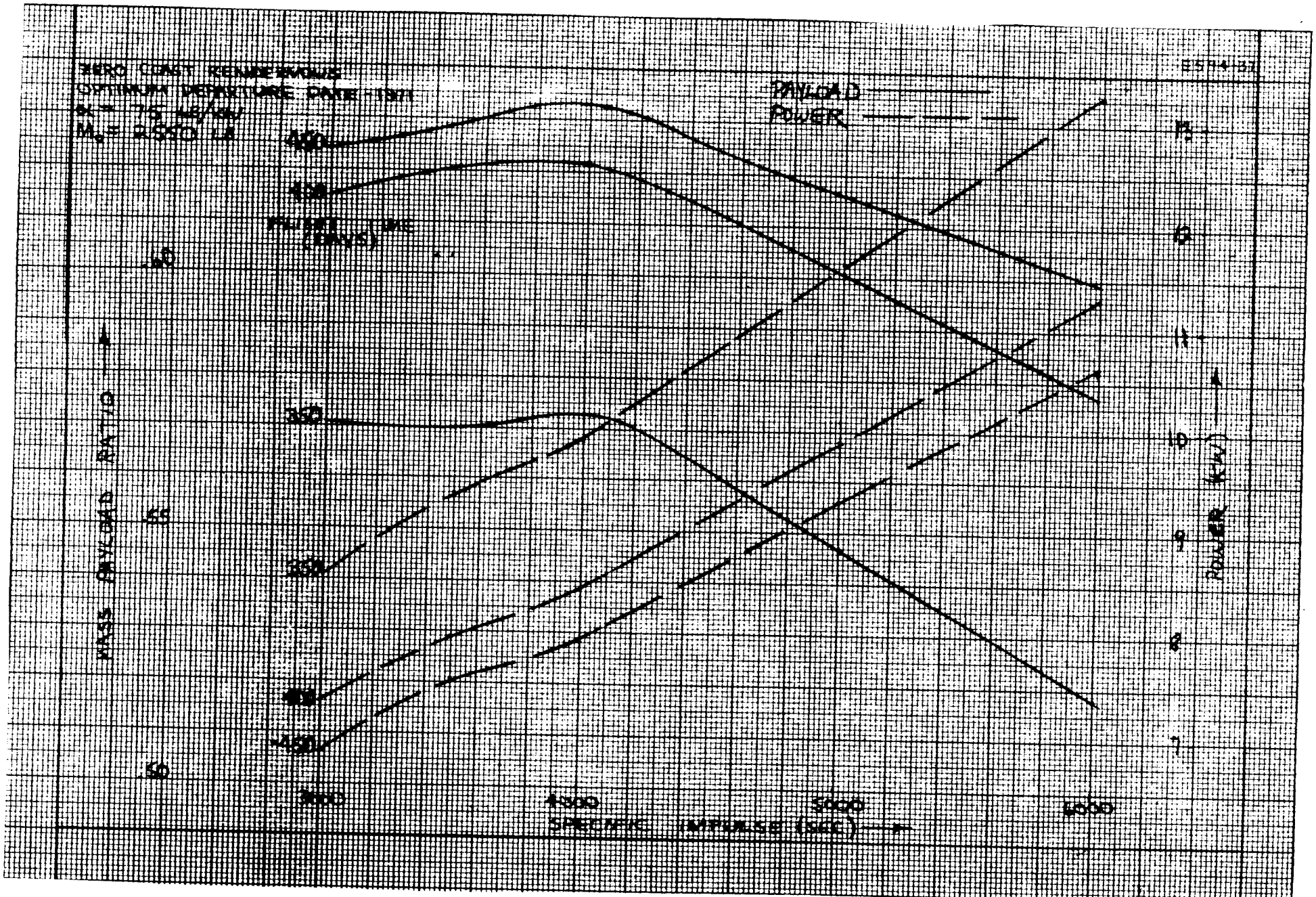

Fig. A.1-1. 1971 Zero coast rendezvous.

Figures A.1-2, A.1-3 and A.1-4 show the power requirements and optimum specific impulse for flyby missions in the years 1971, 1973, and 1975, respectively. Optimum I_{sp} is defined here as that specific impulse at which the sum of the propulsion system and propellant masses are minimized. The term payload mass on these figures is, therefore, defined as that mass brought to the vicinity of the target planet Mars less the mass of the electric propulsion system. Since the spacecraft in these flyby mission profiles will approach Mars with some relative volocity the actual orbital payload must be determined by considering the chemical rocket required to match the velocities of the spacecraft and the planet. Values of the approach velocities are given in Table A.1-I for missions corresponding to those in Figs. A.1-2, A.1-3 and A.1-4. When data was available, the values at optimum I_{sp} were presented.

TABLE A.1-I

APPROACH VELOCITIES

Launch Year	Flight Time (days)	Specific Impulse (sec)	Approach Velocity (m/sec)
1971	250	3.5	2772
	350	4.0	2832
1973	250	3.5	3160
	300	4.0	2043
	350	4.0	1583
1975	250	4.0	4771
	300	4.0	3108
	350	5.0	2326

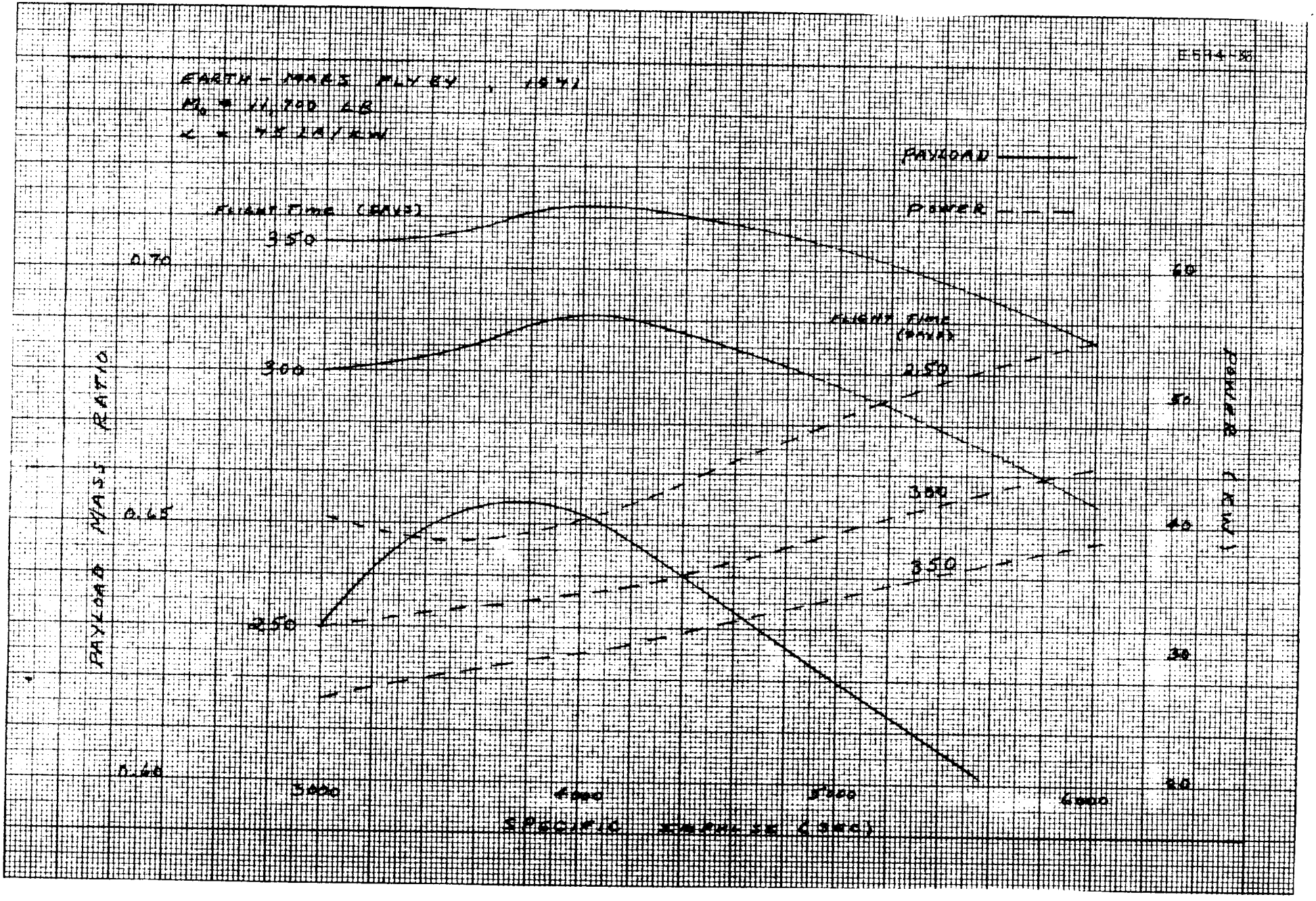

Fig. A.1-2. 1971 Flyby.

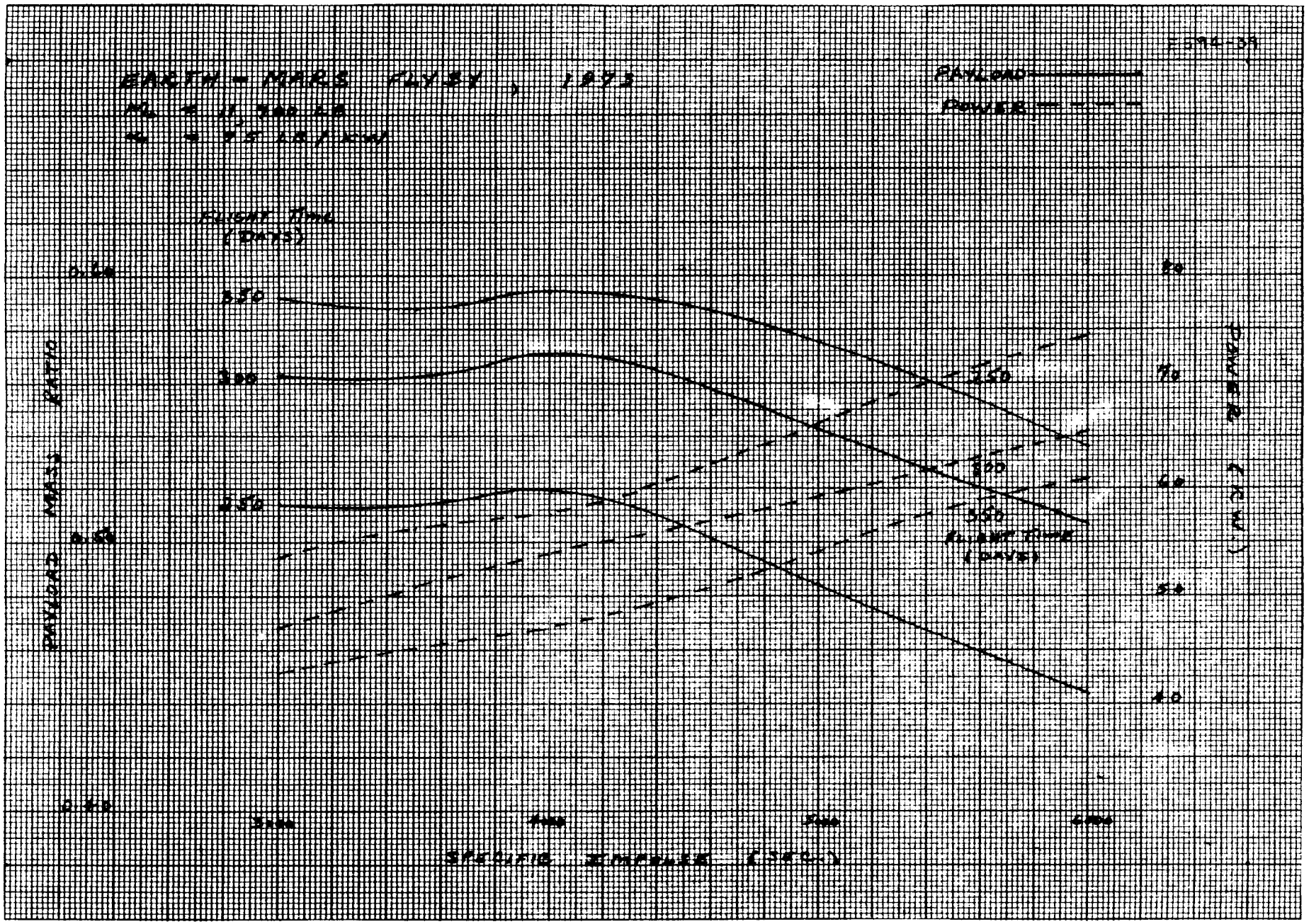

Fig. A.1-3. 1973 Flyby.

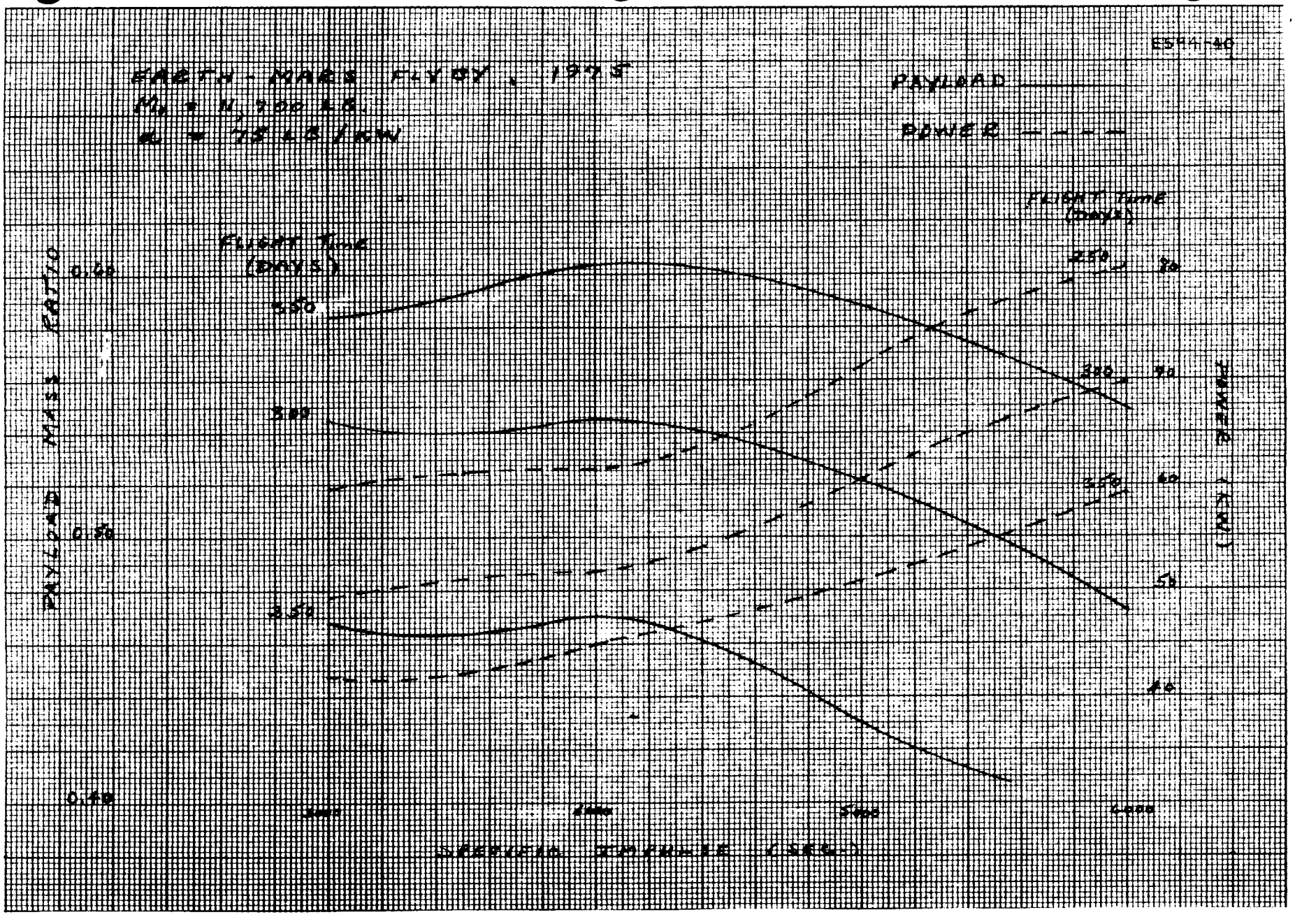

Fig. A.1-4. 1975 Flyby.

B. PROPULSION SYSTEM STUDIES AND HARDWARE

The propulsion system studies which have been performed during this phase of the program have consisted of (1) a study of the effect of power level on the design and operating characteristics of the Hg pool cathode electron-bombardment ion engine and its associated feed system, (2) a conceptual design of a modularized pool cathode engine system, (3) a preliminary analysis of the thermal, mechanical, and electrical integration problems associated with a modularized ion engine system, and (4) a study of the thrust vector displacement in redundant thrustor arrays. The design verification hardware described in this report includes thrustor, feed system, power conditioning and controls.

1. Scaling Study

In order to determine the optimum engine module size for a high power ion propulsion system, the variation of subsystem characteristics with power level must be determined. Also these scaling studies are used to define the optimum design parameters for subsystems at any power level and guarantee that the interpolation and/or extrapolation of existing data during the design phase is done on a realistic basis.

a. Thrustor

In order to establish the relation between power level and engine design parameters, the pool cathode thrustor was scaled over a range of power levels in a manner similar to that presented in Ref. 1 for the oxide cathode engine. The chief differences between the oxide and pool cathodes which affect the scaling studies are:

(1) heat rejection requirement

(2) beam distribution

It can be shown that the same engine diameter versus engine power relationship which was derived for the oxide cathode (Ref. 1) may be used for the pool cathode. However, the engine weight versus power relation is much steeper for the pool cathode.

The engine diameter versus engine power relation derived in Ref. 1 (repeated here as Fig. B. 1-1) was based on engine designs qualified both with respect to perveance and life considerations. These considerations require a knowledge of beam distribution, represented by a factor called the "peak to average" ratio. This ratio for the late model oxide engines is at the most 2:1. Data (Fig. B. 1-2) on the pool cathode engine (Ref. 2) shows beam distributions on the order of 3:1. This increase in beam distribution, however, may be accommodated by just an increase in accel electrode thickness. With this one modification, we can still expect the same power versus engine size relationship as before. It is possible to expect the pool cathode beam distribution to eventually become as good as that of the oxide cathode engine. The oxide engine has had much development which has led to the improved beam distribution which it now exhibits (See for example Ref. 3). Pool cathode engines, on the other hand, are fairly new and have as yet not been optimized with respect to beam distribution. If the pool cathode distribution were improved to 2:1, the engine requirements would be identical with those of the oxide engine and the accel electrode would not need to be modified.

As shown in Ref. 1 lifetime is proportional to the square of current density. Hence, if the local current density goes up by a factor of 3/2, the lifetime decreases by a factor of 2. This factor of 2 can be canceled by simply making the specified accel thickness 3.0 mm instead of the original 1.5 mm indicated in Ref. 1. The hole size and electrode spacing remain the same. Hence, the relationship in Fig. B. 1-1 is used in conjunction with the other aspect of the pool cathode engine; cathode heat rejection.

A pool cathode can be expected to have a total heat rejection requirement of 2% of the total engine power (the cathode heat load is ion bombardment plus thermal radiation). A cathode upper temperature limit of 130°C is assumed for the calculations which follow. This has been found to be a safe operating temperature for cathodes currently being tested in the laboratory. However, new cathode designs

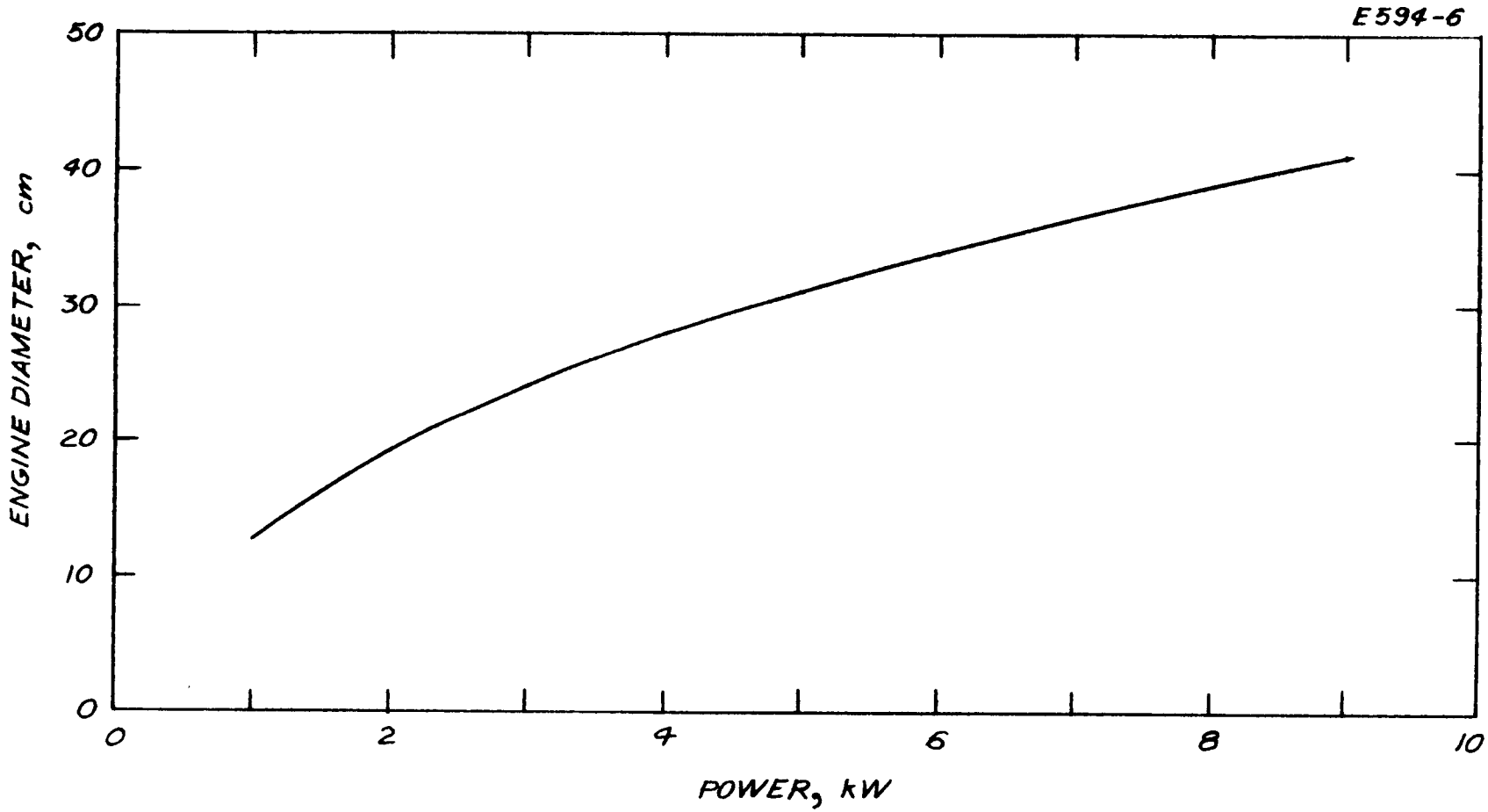

Fig. B.1-1. Engine diameter versus engine power for oxide cathode and pool cathode engines. I_{sp} = 4000 sec.

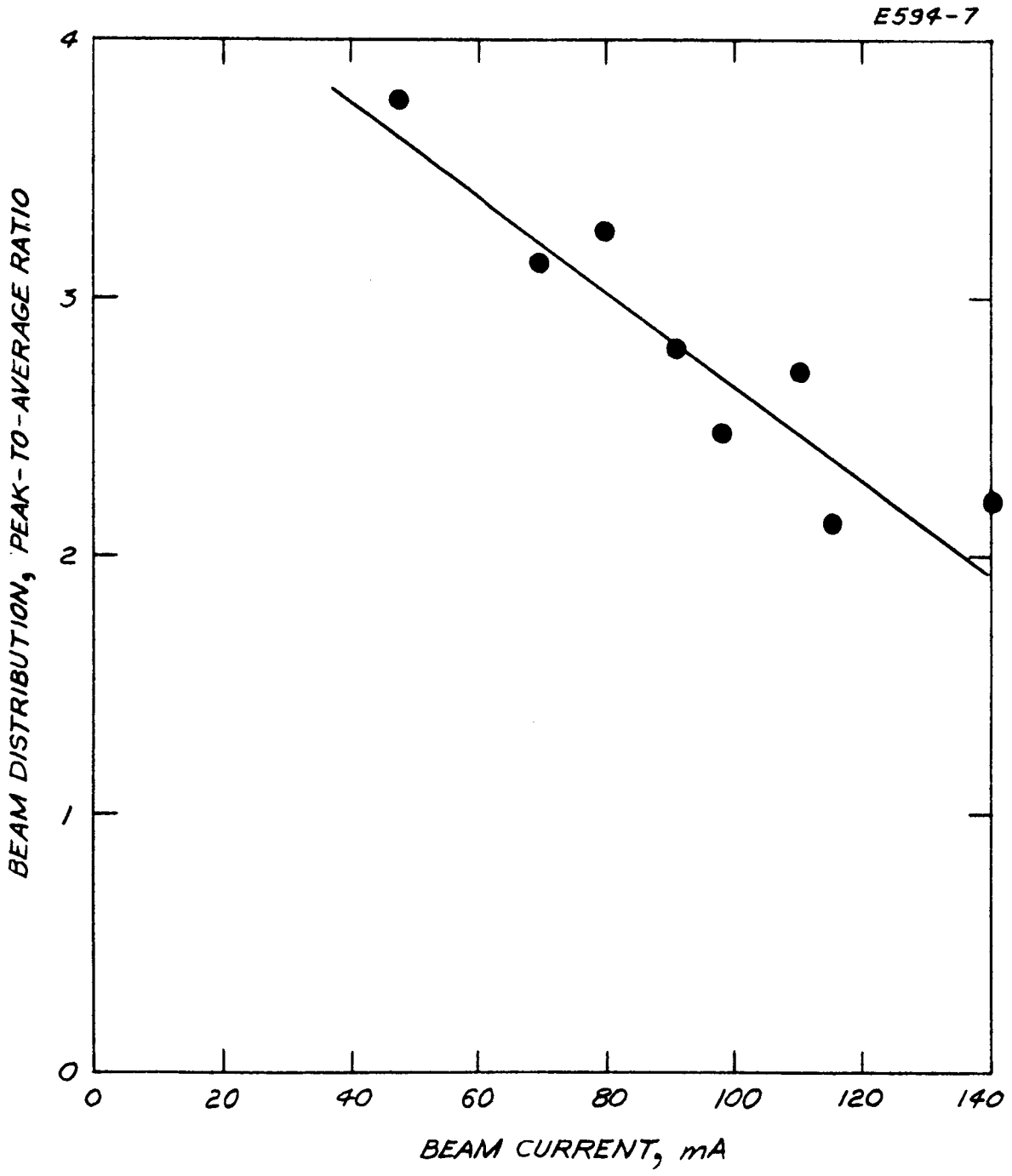

Fig. B.1-2. Beam probe data for 10 cm pool cathode engine.

indicate that it may be possible to build a pool cathode which has no temperature limit. In that case, the weight penalties which result from radiator cooling of the cathode would be eliminated. Even if the temperature requirement cannot be eliminated completely, reductions in radiator weight can be obtained by improvements which allow the cathode upper temperature limits to be raised. This would allow a higher radiator temperature and a higher temperature drop from radiator to cathode, resulting in a lowering of the radiator area and thickness requirement.

When considering a heat rejection system, it is necessary to have the complete spacecraft system in mind. In other words, cathode heat rejection is classified as an "interface" problem between propulsion system and spacecraft. For example, if a spacecraft is able to tolerate the heating effect of the rejected power, then control of the cathode temperature is fairly easy. On the other hand, if it is assumed the vehicle can accommodate none of the engine heat, a constraint is imposed on the heat rejection system. This causes the heat rejection system to be somewhat heavier, since a direct heat path to space must be provided. In either event, satisfactory cathode temperature control may be maintained with a simple passive heat rejection system: an aluminum radiator.

There are three possible radiator configurations. Requirements of the particular spacecraft design determine which radiator system is most applicable. The three systems are identified as follows: (1) front-type, (2) side-type, and (3) rear-type radiator.

The front-type radiator system finds application where the thrustor array is counter-sunk within the vehicle, with the constraint that no heat be dumped into the vehicle. Figure B.1-3 shows this configuration schematically. In this configuration, the over-all array dimensions must be increased to allow exposure of the radiating area (which is at the rear of the engines). The radiating area required for this design is approximately twice the area of the engine cross-section.

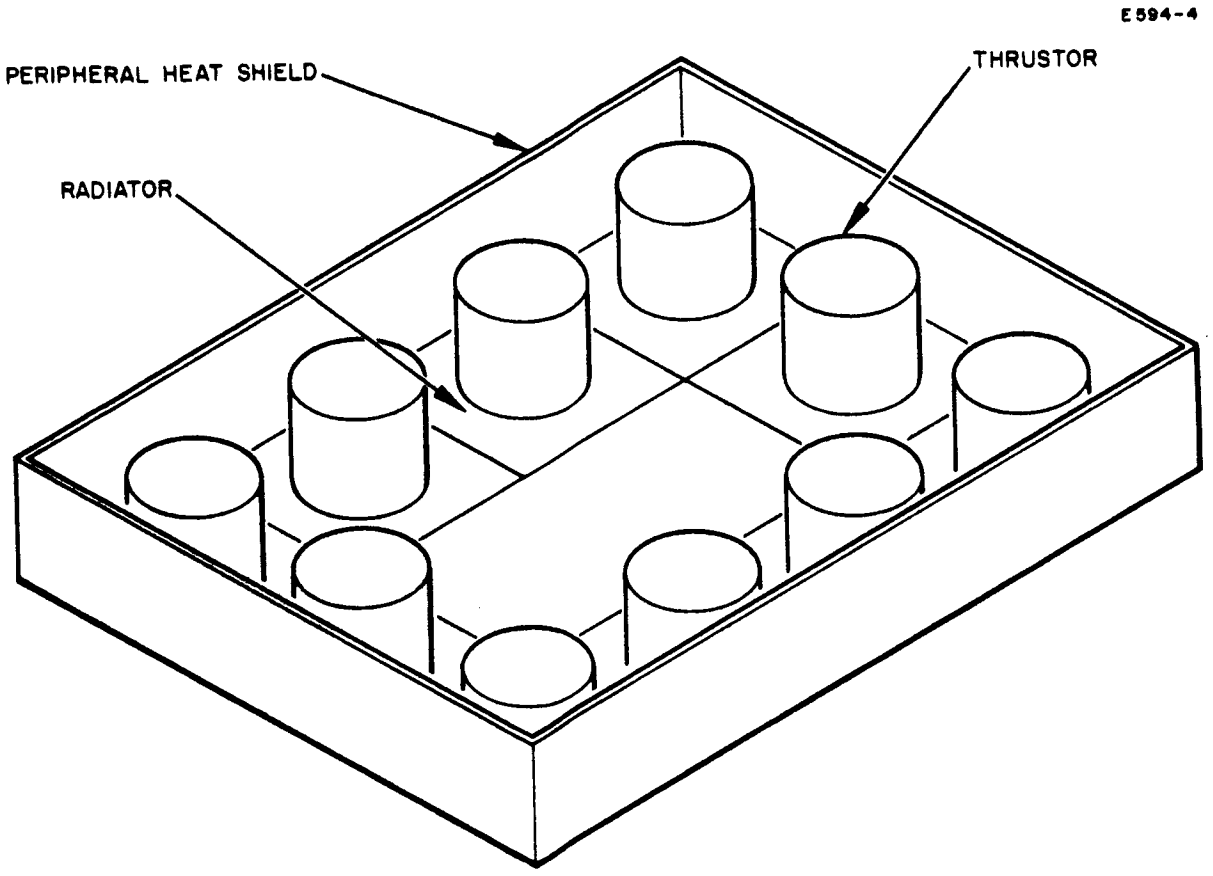

Fig. B.1-3. Engine array utilizing front-type radiator.

The following calculations demonstrate the weight requirement for the front type of radiator. The results are general, for any size engine. The following nomenclature is first defined (see Fig. B.1-4):

C = cathode diameter, 1.0 cm
d = beam diameter, cm
D = over-all engine diameter, 1.4 d
Q = heat rejection per engine, $125(d/35)^2$, W
k = thermal conductivity of aluminum, 2 W/cm-degree.
t_b = radiator base thickness, cm
t_r = radiator thickness, cm
$\mathcal{D}$ = over-all diameter of engine plus radiator.

Since the area of the radiator is twice the area of the engine

$$\frac{\pi}{4}\mathcal{D}^2 = 3\frac{\pi}{4}D^2, \text{cm}^2 \qquad (1)$$

$$\mathcal{D}/D = 1.73 \ .$$

The first calculation is to determine the mean radiator operating temperature (T_r). This is accomplished with the following equation

$$Q = \eta \epsilon A_r \sigma T_r^4 \qquad (2)$$

where

A_r = radiating area, $2(\pi D^2/4)$
ϵ = emissivity, 0.8
η = radiator effectiveness, 0.5 .

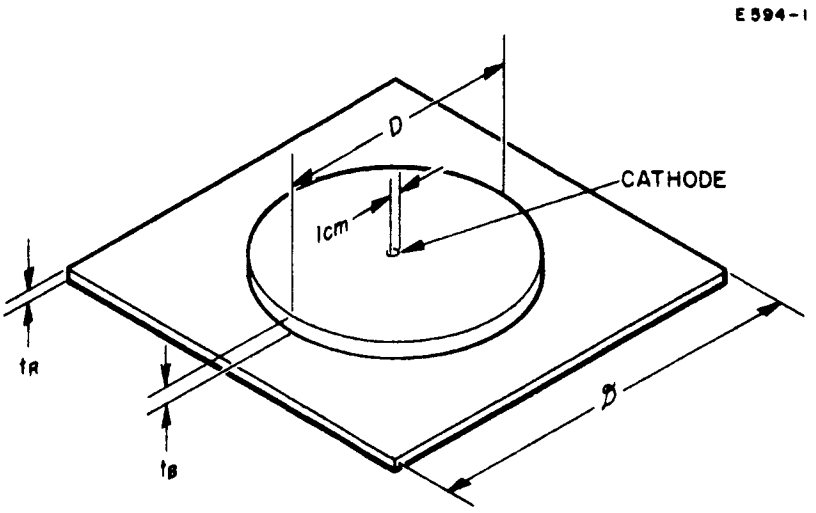

(a) FRONT-TYPE

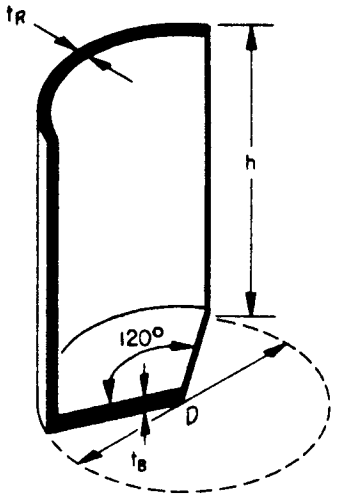

(b) SIDE-TYPE

Fig. B.1-4. Radiator configurations and dimension nomenclature.

Solving for T_r

$$(T_r/1000)^4 = \frac{Q}{(0.5)(0.8)\left(\frac{\pi}{2}\right)D^2 (5.67)} = \frac{125\,(d/35)^2}{(0.5)(0.8)\frac{\pi}{2}(1.4d)^2 (5.67)}$$

$$= 0.015$$

$$T_r = 350^\circ K = 80^\circ C \quad .$$

It is noticed that this result is independent of engine size.

The temperature drop across the base (ΔT_b) is given as a function of beam diameter, by the following calculation

$$\Delta T_B = \frac{Q \ln \frac{D}{C}}{2\pi k\, t_B} = \frac{(d/35)^2 (125)(3.5^*)}{2\pi (2)\, t_B}$$

$$\Delta T_B = \frac{3}{t_B}\left(\frac{d}{10}\right)^2 {}^\circ C \quad . \tag{3}$$

Next, the temperature drop across the radiator is related to beam diameter

$$\Delta T_r = \frac{Q \ln \not{O}/D}{2\pi k\, t_r} = \frac{(d/35)^2 (125)(0.55)}{2\pi (2)\, t_r}$$

$$\Delta T_r = \frac{1}{2t_r}\left(\frac{d}{10}\right)^2 {}^\circ C \quad . \tag{4}$$

Since the maximum cathode temperature is $130^\circ C$, the following relation determines the maximum tolerable temperature drop between radiator and cathode

---

*Average value of $\ln (D/C)$ for $20 < D < 50$ cm.

$$T_r + \frac{\Delta T_r}{2} + \Delta T_b = 130^{\circ}C$$

$$\frac{\Delta T_r}{2} + \Delta T_b = 50^{\circ}C \quad . \tag{5}$$

Using eqs. (3), (4), and (5), one relationship between t_b and t_r arises

$$\left(\frac{d}{10}\right)^2 \left(\frac{3}{t_b} + \frac{1}{4t_r}\right) = 50^{\circ}C \quad . \tag{6}$$

To solve for the direct relation between t_b and t_r, another equation is required. This other relation arises from the condition of minimum radiator system weight. Radiator weight is given by

$$Wt = \frac{\rho}{454}\left[\left(\frac{\pi}{4} D^2\right)t_b + \left(\frac{2\pi}{4} D^2\right)t_r\right] \text{ lbs} \tag{7}$$

where ρ = density of aluminum = 2.7 gms/cc. The radiator weight relation may be reduced to the following form

$$Wt = \frac{2.7}{454}\left(\frac{\pi}{4}\right)(1.4\ d)^2\ (t_b + 2t_r)$$

$$Wt = \left(\frac{d}{10}\right)^2\ (t_b + 2t_r) \quad . \tag{8}$$

To impose the condition of minimum weight, we differentiate both sides of eq. (8) with respect to t_b and set the result equal to zero

$$\frac{\partial}{\partial t_b}(Wt) = \left[1 + 2\ \frac{\partial t_r}{\partial t_b}\right]\ \left(\frac{d}{10}\right)^2$$

$$\frac{\partial t_r}{\partial t_b} + \frac{1}{2} = 0 \quad . \tag{9}$$

Differentiating eq. (6)

$$\frac{\partial t_r}{\partial t_b} = -12\left(\frac{t_r}{t_b}\right)^2 \quad . \tag{10}$$

Substituting eq. (1) into eq. (9)

$$t_b = 5\, t_r \quad . \tag{11}$$

This is the condition for minimum weight. The result is independent of engine size, and indicates that in all cases the radiator base thickness should be five times the thickness of the radiator itself (see Fig. B.1-4).

Substituting eq. (11) into eq. (6) yields the direct dependence of radiator thickness t_r (and also t_b) on engine size

$$\left(\frac{d}{10}\right)^2 \left[\frac{3}{5t_r} + \frac{1}{4t_r}\right] = 50^\circ C$$

$$t_r = 0.017\left(\frac{d}{10}\right)^2 \text{ cm} \quad . \tag{12}$$

A plot of eq. (12) is given in Fig. B.1-5 (lower curve). The left-hand axis is t_r and the right-hand axis for t_b, is established by the relation $t_r = 5t_r$.

Radiator weight is now directly obtainable from eq. (8) since t_b and t_r are known. The result is presented in Fig. B.1-6 (middle curve). To show that this result makes smaller engines look more desirable, we divide radiator weight by engine power (using Fig. B.1-1). This results in the specific weight addition to the system associated with the radiator (Fig. B.1-7, middle curve). For engines less than 20 cm, radiator specific weight can be held to less than 1 lb/kW.

The next type of radiator system to be considered is the side-type configuration. This system is applicable in a space vehicle which incorporates a surface mounted propulsion system (Fig. B.1-8). This

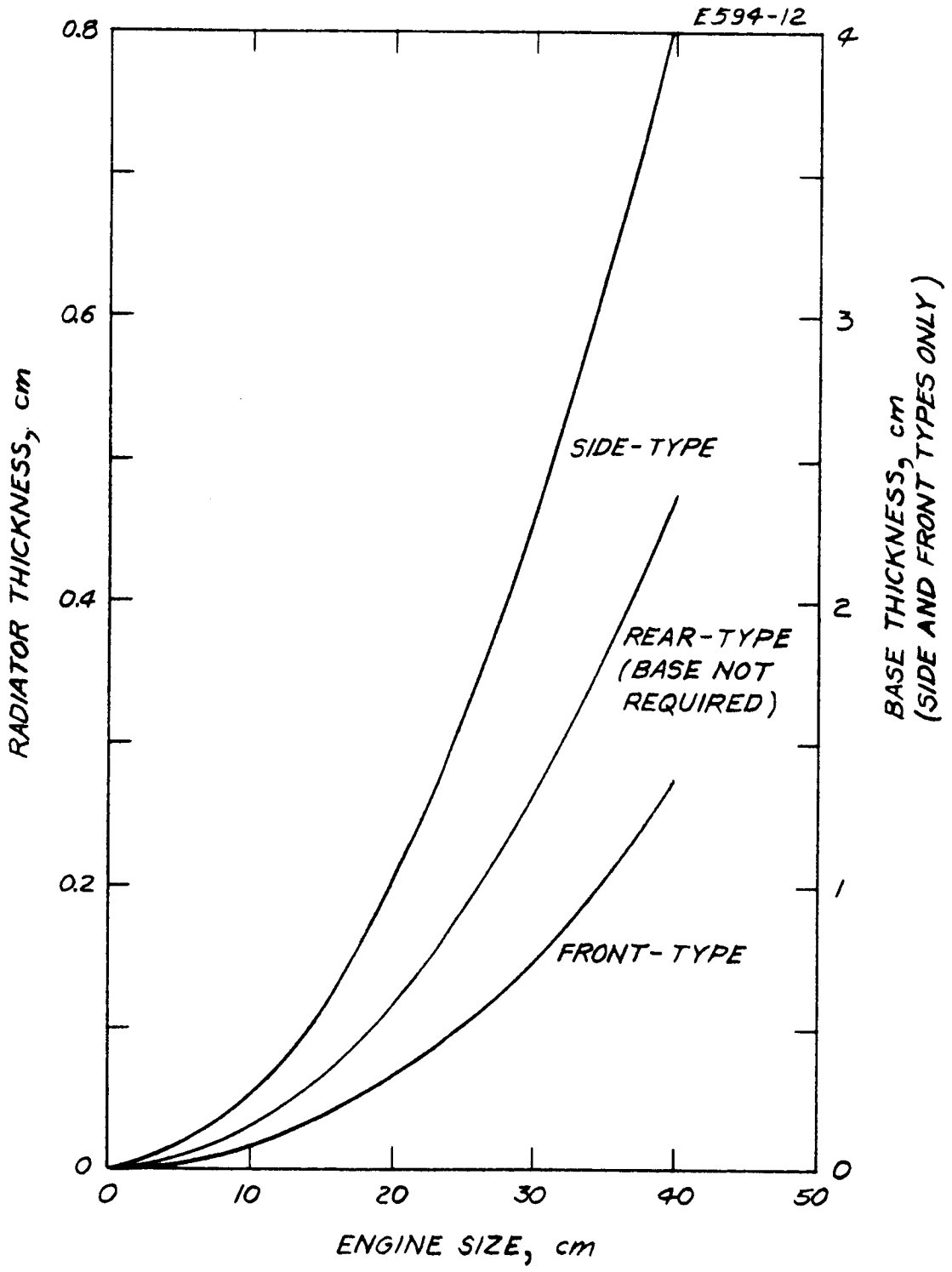

Fig. B.1-5. Pool cathode engine thermal radiator thickness versus engine size.

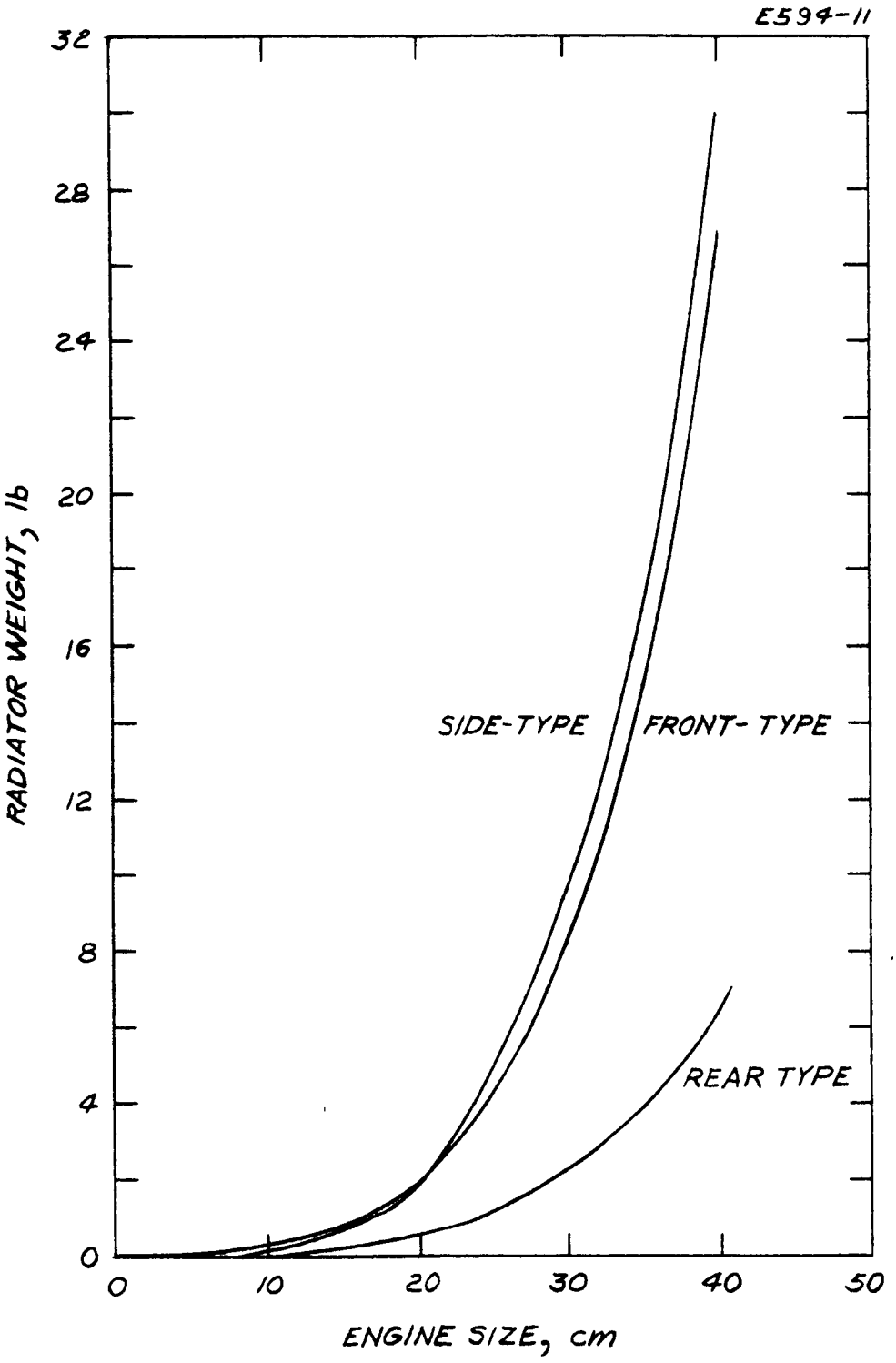

Fig. B.1-6. Pool cathode engine thermal radiator weight versus engine size.

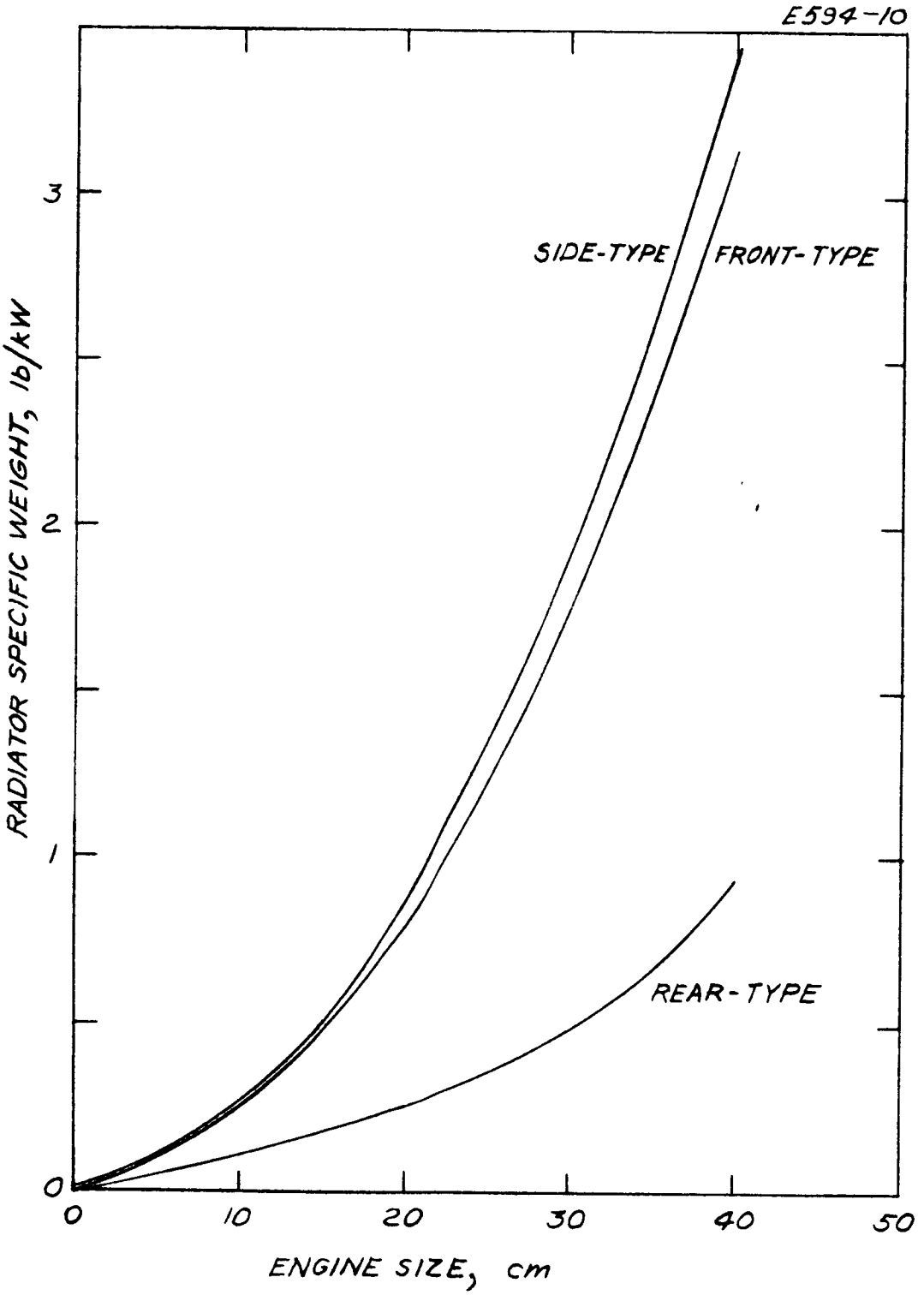

Fig. B.1-7. Pool cathode engine thermal radiator specific weight versus engine size.

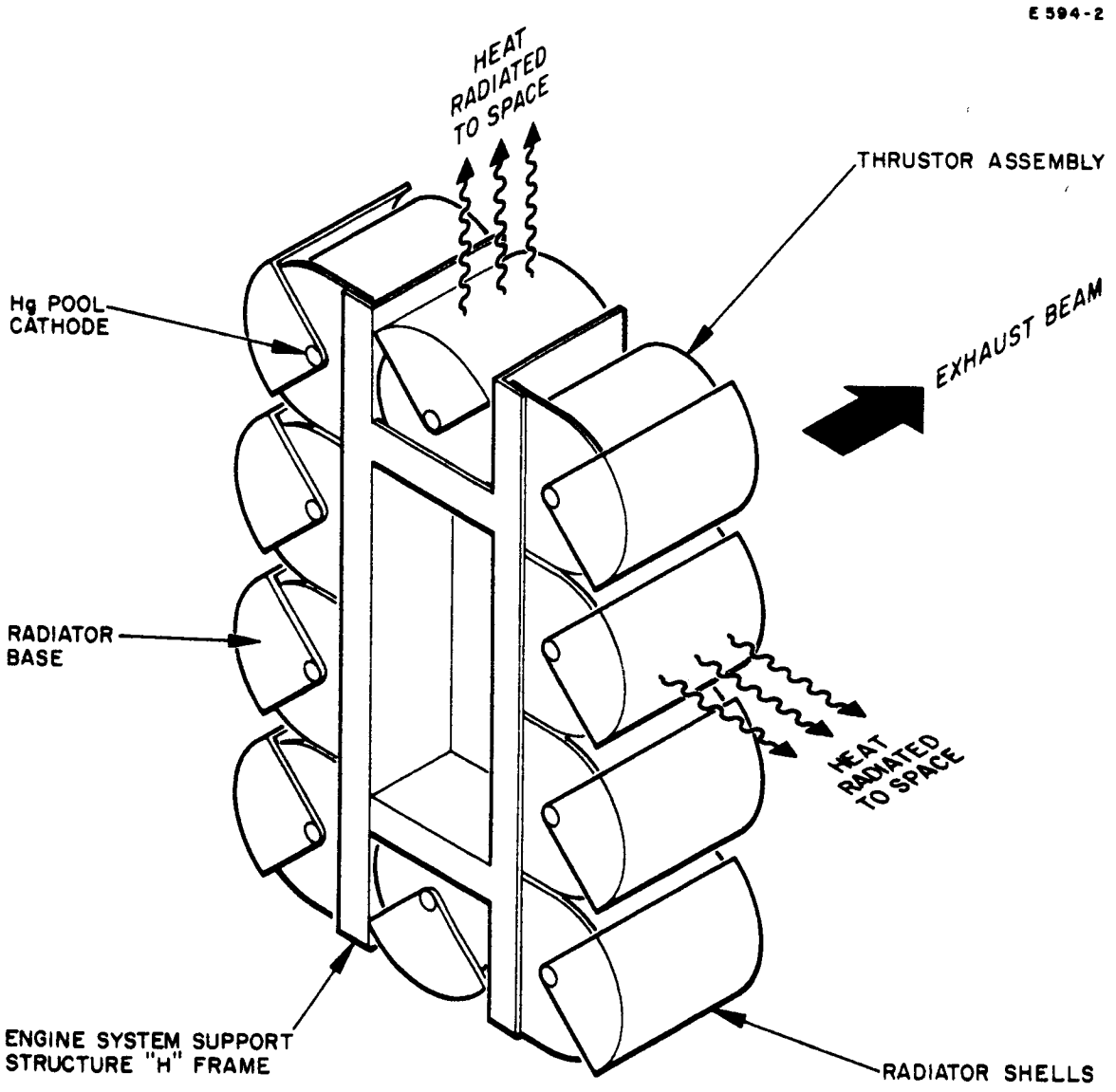

Fig. B.1-8. Array of 6 kW pool cathode engine modules utilizing side-type radiators.

radiator system also satisfies the constraint that no engine heat be accepted by the vehicle. The following calculations indicate that the total weight requirement for the side radiator arrangement is similar to the front-type. Less radiating area is required, since the radiators are directly exposed to space and hence are more efficient ($\eta = 1$).

Similar considerations as spelled out above for the front radiator show that the side radiator operating temperature is also 80°C. The base temperature drop for the side radiator is calculated by

$$\Delta T_b = \frac{3 \ln (D/C)}{2\pi k\, t_b} Q \quad . \tag{13}$$

The factor of 3 appears because only one third of the base area is utilized for conduction. Substituting values in eq. (13)

$$\Delta T_b = \frac{(3)\,(3.5)\,(d/35)^2\,125}{2\pi\,(2)\,t_b}$$

$$\Delta T_b = \frac{9}{t_b}\left(\frac{d}{10}\right)^2 \tag{14}$$

The temperature drop across the radiator of the side-type configuration is

$$\Delta T_r = \frac{3hQ}{2k\pi D t_r}$$

where h = height of engine (h = d). Evaluating

$$\Delta T_r = \frac{3d(125)\,(d/35)^2}{(2)\,(2)\,\pi\,(1.4d)\,t_r} = \frac{2}{t_r}\left(\frac{d}{10}\right)^2 \quad . \tag{15}$$

Again using eq. (5) to assure that the cathode temperature remains below 130°C

$$\left(\frac{d}{10}\right)^2 \left(\frac{9}{t_b} + \frac{1}{t_r}\right) = 50^\circ C \quad . \tag{16}$$

The weight equation in this case is

$$Wt = \left[\left(\frac{\pi D}{3}\ \ln\right) t_r + \left(\frac{1}{3}\ \frac{\pi}{4}\ D^2\right) t_b\right] \frac{2.7}{454}$$

which reduces to

$$Wt = \left(\frac{d}{10}\right)^2 \left(t_r + \frac{t_b}{3}\right) 0.84 \quad . \tag{17}$$

Using the minimum weight criteria, as demonstrated above, yields the same five to one ratio between t_b and t_r. Replacing t_b with $5t_r$ in eq. (16)

$$\left(\frac{d}{10}\right)^2 \left(\frac{9}{5t_r} + \frac{1}{t_r}\right) = 50$$

$$t_r = 0.056 \left(\frac{d}{10}\right)^2 \text{ cm} \quad . \tag{18}$$

Using eq. (18) and (11), both t_b and t_r are plotted in Fig. B.1-5 (upper curve). The resulting weight and specific weight curves are shown in Fig. B.1-6 and B.1-7, respectively.

Of the three types of radiators considered for engines of the 48 kW system, the rear-type radiator is by far the lightest weight system. However, it takes a particular spacecraft configuration to utilize this mode of heat rejection (see Fig. B.1-9). If heat is not to be accommodated by the spacecraft, then the rear of the engines must be exposed to free space. Thus, the rear radiator may be employed only under one of the following spacecraft conditions:

(1) The propulsion system is extended away from the vehicle when operating.

(2) A void exists through the spacecraft (Fig. B.1-9) (arch structure)

(3) Cathode heat rejection may be accommodated by the vehicle.

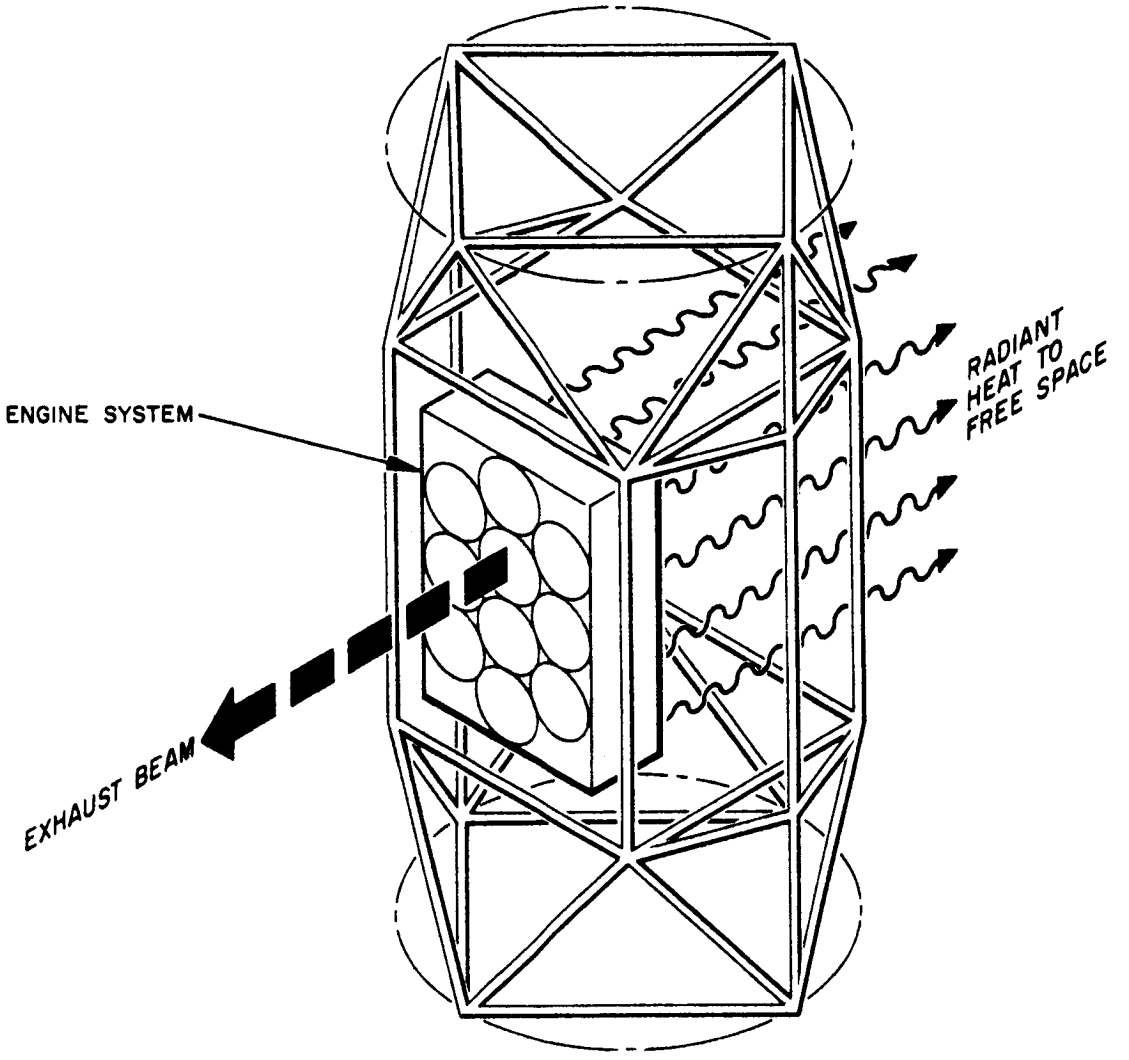

Fig. B.1-9. Spacecraft structural configuration for pool cathode engine system using rear-type radiators.

Radiator weight for the rear-type configuration is determined by the following calculations. The radiating area per engine is equal to that of the engine cross-section

$$A_r = \frac{\pi}{4} D^2 \tag{19}$$

As shown above, a radiating area of this amount produces a radiator temperature of 80°C independent of engine size. For the rear-type system (as shown later in Fig. B.1-10) the base plate and radiating area are one and the same. In other words, there is no additional aluminum required as a path from cathode to radiator, as in the front and side-type radiator systems. The radiator is in the immediate vicinity of the cathode, providing a more efficient system. This is why the weight of the rear-type radiator system turns out to be so much lower than that of the other two alternative systems. The temperature drop across the radiator is calculated by the following equation

$$\Delta T = \frac{Q \ln (D/C)}{2\pi k t_r} \quad . \tag{20}$$

Replacing the parameters with their values, eq. (20) yields

$$\Delta T = \frac{3}{t_r} \left(\frac{d}{10}\right)^2 {}^{\circ}C \ . \tag{21}$$

Since the cathode maximum temperature is 130 °C

$$80 + \frac{\Delta T}{2} = 130^{\circ}C$$

$$\frac{\Delta T}{2} = 50^{\circ}C \quad . \tag{22}$$

From eqs. (21) and (22)

$$\frac{3}{2t_r}\left(\frac{d}{10}\right)^2 = 50$$

$$t_r = \frac{3}{(2)(50)}\left(\frac{d}{10}\right)^2 = 0.03\left(\frac{d}{10}\right)^2 \text{ cm} \quad . \qquad (23)$$

This relation is shown in Fig. B.1-5. The weight for a rear-type radiator is then obtained by

$$Wt = \frac{2.7}{454}\left(\frac{\pi}{4} D^2 t_r\right)$$

$$Wt = \frac{2.7}{454}\left(\frac{\pi}{4}\right)(1.4)^2 d^2 t_r = 0.915\left(\frac{d}{10}\right)^2 t_r \text{ lbs} \quad .$$

See Fig. B.1-6 for the weight plot of the rear-type radiator.

Although the rear-type system is by far the lightest and most compact of those considered, it also presents the greatest spacecraft interface problem. Because of the requirement that heat be rejected from the rear of the engines, the rear radiator type system presents the most difficult mounting problem.

One other consideration in these radiative cooling systems is the requirement to shield the radiators from the major engine heat losses. The major losses are those associated with the power generated in the arc discharge. There is no problem in implementing this shielding. The usual laminated foil shields may be placed between thrustor body and radiator within a fairly close space. Each of the above three schemes has a different requirement for the total heat shielded area required, as seen in Figs. B.1-4 and B. 1-10. The front radiator requires the most shielding and the rear radiator requires the least.

Certain experimental verification of passive cooling of the pool cathode has been demonstrated in a thermal mock-up. Various heaters were used to simulate both the arc and cathode heat generation. The rear-type configuration was used in this experiment. Figure B.1-10 is a photo of the apparatus, utilizing a 20 cm bombardment engine. It is noticed that a space has been reserved between engine and radiator. This was to allow for feed system components which are now out-dated. This space is no longer required because of the more compact feed equipment now being developed.

The heat shielding shown in the photo is illustrative of that required by any of the three radiator configurations. The results of the thermal simulation experiment are presented in Fig. B.1-11. The upper curve corresponds to a one amp beam, while the lower two are for a half amp beam.

Although the rear-type radiator arrangement is both the lightest and most compact, its use imposes the most severe constraint on the spacecraft system. The constraint will either be a sacrifice of usable spacecraft volume, a spacecraft heat load penalty, or engine deployment (see Fig. B.1-9).

It is because of this interface constraint that the other two alternatives (side and front radiators) are given detailed consideration. It has already been demonstrated that the radiator weight versus engine size relation is almost identical for the front and side systems. The remaining consideration is over-all dimensions for the array of engines required to produce the 48 kW. It turns out that for an array of many small engines a front-type radiator is more desirable, whereas for an array of a few large engines, a side-type is preferable. Figure B.1-12 shows the comparative sizes of the arrays. The small dimension in all cases is held constant at five feet, since this is the maximum available distance consistent with the current spacecraft configuration. It is desired to keep the large dimension as small as possible from thrust alignment considerations (see section B.4). For a 6 kW module array, the side-type radiator system is seen to be almost twice as compact as the front-type. On the other hand, for a 1.5 kW module array the front-type radiator configuration is one foot smaller than the side type. In both cases, however, the optimum arrangement is five by seven feet.

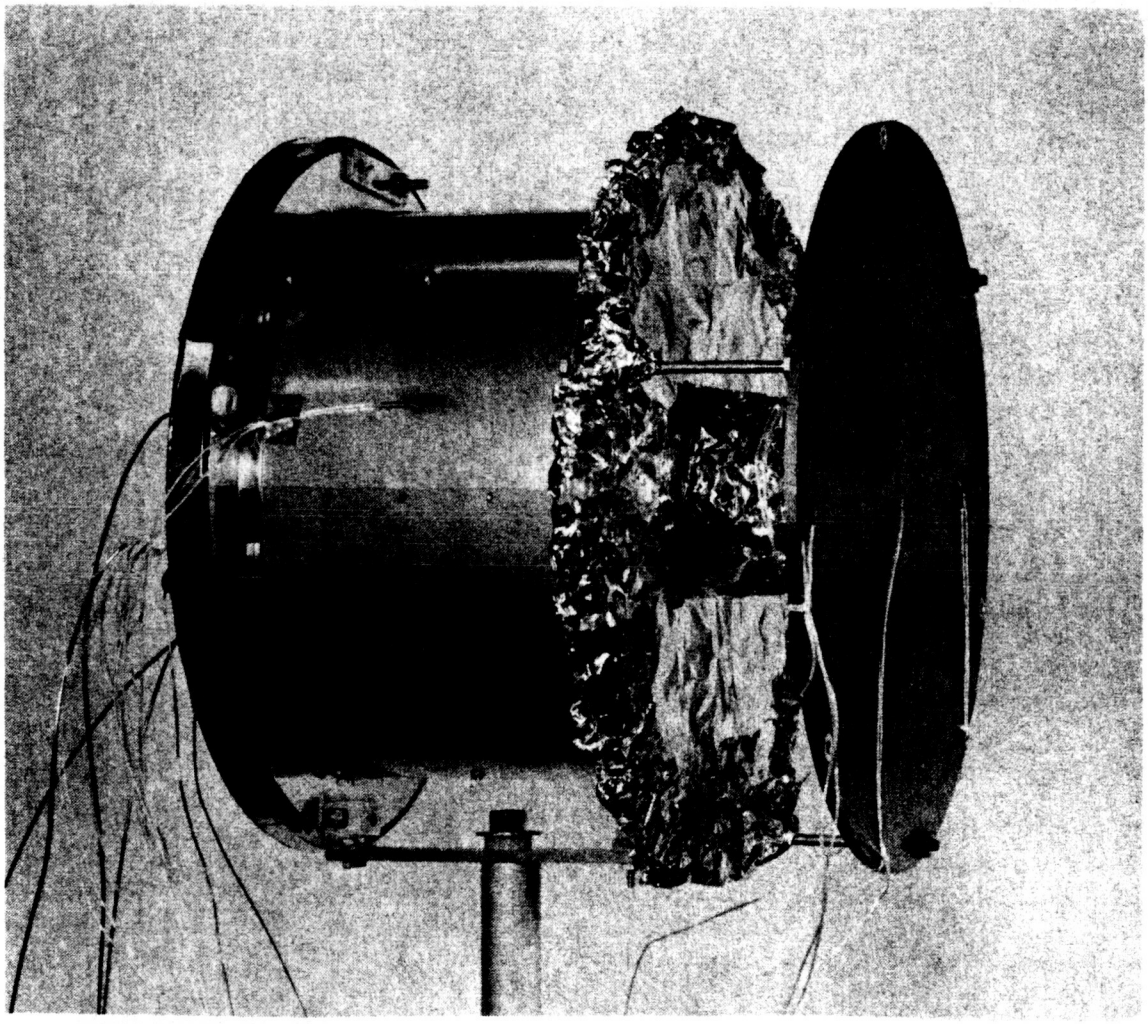

Fig. B.1-10. Pool cathode engine with rear radiator used in thermal similation test.

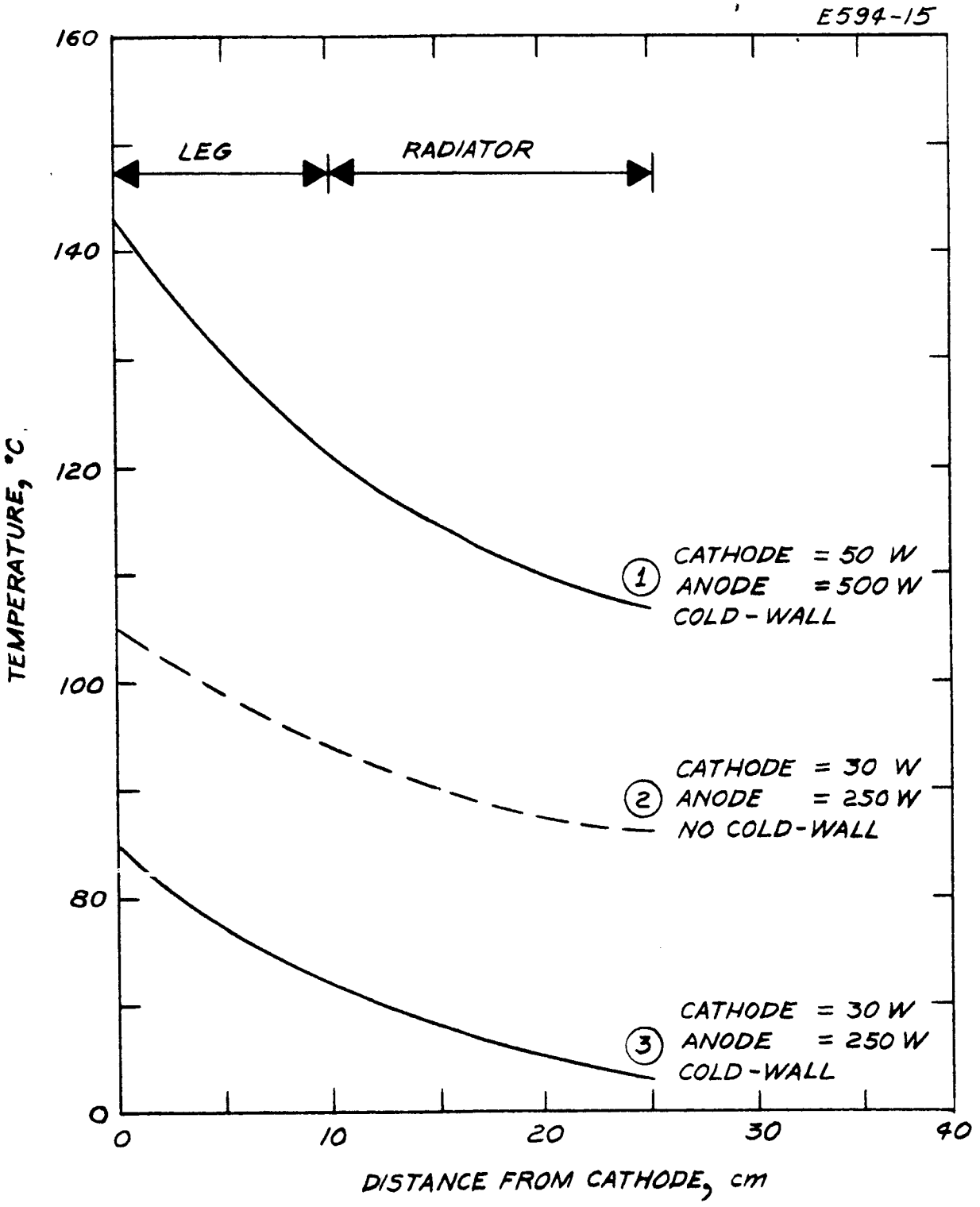

Fig. B.1-11. Aluminum heat sink temperature profiles from pool cathode engine thermal simulation test.

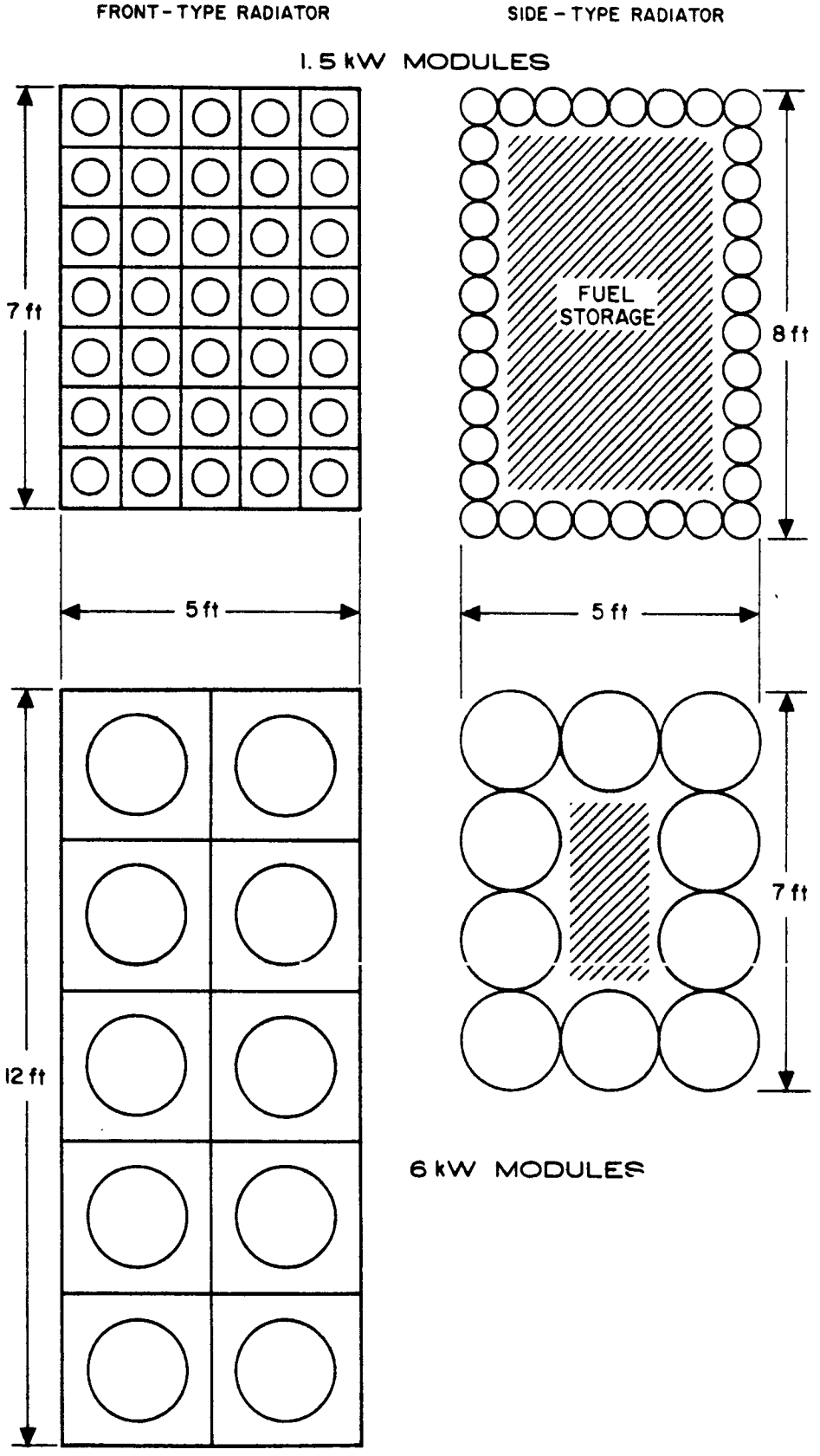

Fig. B.1-12.
Comparison of side and front radiator arrays for both large and small engines (48 kW system).

The optimum pool-cathode thrustor module size will be selected, based on the weight-reliability criterion as discussed in Ref. 1. Therefore, the functional relationship between thrustor power level and thrustor weight must be found. To obtain this relationship, we start with that established for the oxide engine in Ref. 1. Then we add to it the weight due to the increased thickness of the accel electrode. Lastly, the weight of the radiator is added. These effects are demonstrated in Fig. B.1-13, where all three possible radiators have been considered. It is seen that the pool cathode percent weight increase is much less for small engines than for large.

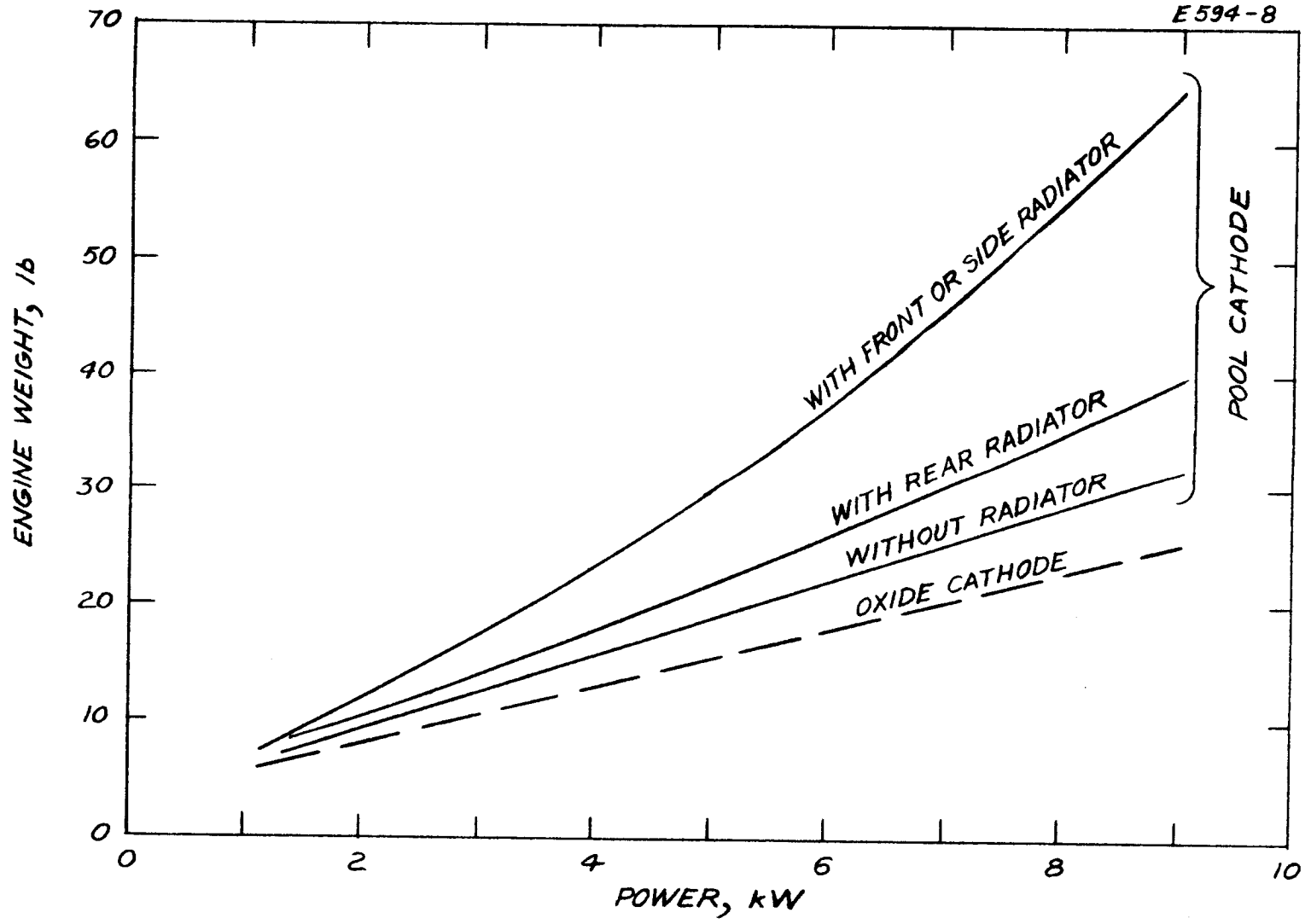

Fig. B.1-13. Engine weight versus engine power for Hg bombardment engine. I_{sp} = 4000 sec.

REFERENCES

1. Solar-powered Electric Propulsion Spacecraft, Bi-Monthly Report No. 2, Hughes Aircraft Co., Contract No. 951144 (JPL), July 1965.

2. Fabrication and Testing of Liquid-Mercury Cathodes in an Electron Bombardment Ion Thrustor, Quarterly Report No. 1, Hughes Aircraft Co., Contract No. 3-6262 (NASA), October 1964.

3. Accel Grid Tests on an Electron Bombardment Ion Rocket, W. R. Kerslake, NASA TN D1168.

b. Feed System

The feed system module for a pool cathode engine is shown schematically in Fig. B.1-14. The unit consists of two basic components: (1) a pressure source, and (2) the mercury reservoir. The unit thus provides a complete feed system. No other components are required, since this system provides good control of the amount of mercury leaving the reservoir. The liquid goes from the reservoir directly to the cathode.

Flow regulation is provided by variation of power on the pressure source heater. The pressure source contains a saturated vapor, such that the pressure change is a strong function of temperature. This portion of the feed system also contains a bellows (see Fig. B.1-14).

A piston interconnects both the pressure source and reservoir sections of the feed system. The reservoir unit is fitted with a "rolling diaphragm." The diaphragm is a flexible, organic material, which is in the shape of a cup. The diaphragm acts to keep the mercury upstream from the piston in the reservoir. The piston acts on the bottom of the cup and during operation of the system the cup becomes inverted with respect to its original position.

Relative dimensions are shown in Fig. B.1-14. The overall length of the reservoir section is 2.5 times the diameter (D_f). The piston occupies a distance of one diameter, and the mercury occupies the remaining 1.5 diameters. The pressure source section length is about twice the reservoir diameter.

A support is provided, connecting the two separate sections of the feed system. The result is an integral unit, not requiring additional mounting accomodations.

Feed system scaling requires estimating the size and weight of the above described unit for a thrustor module of any power level. The total amount of propellant for the model mission is 1600 lb and can be divided into a number of reservoirs equal to the number of engines used.

From the foregoing geometric considerations, usable reservoir volume (V) is given by :

$$V = (\frac{\pi}{4} D_f^2)(1.5\ D_f) = 1.18\ D_f^3 \text{ cc.} \qquad (25)$$

where D_f is the feed system diameter. The density of mercury ρ is :

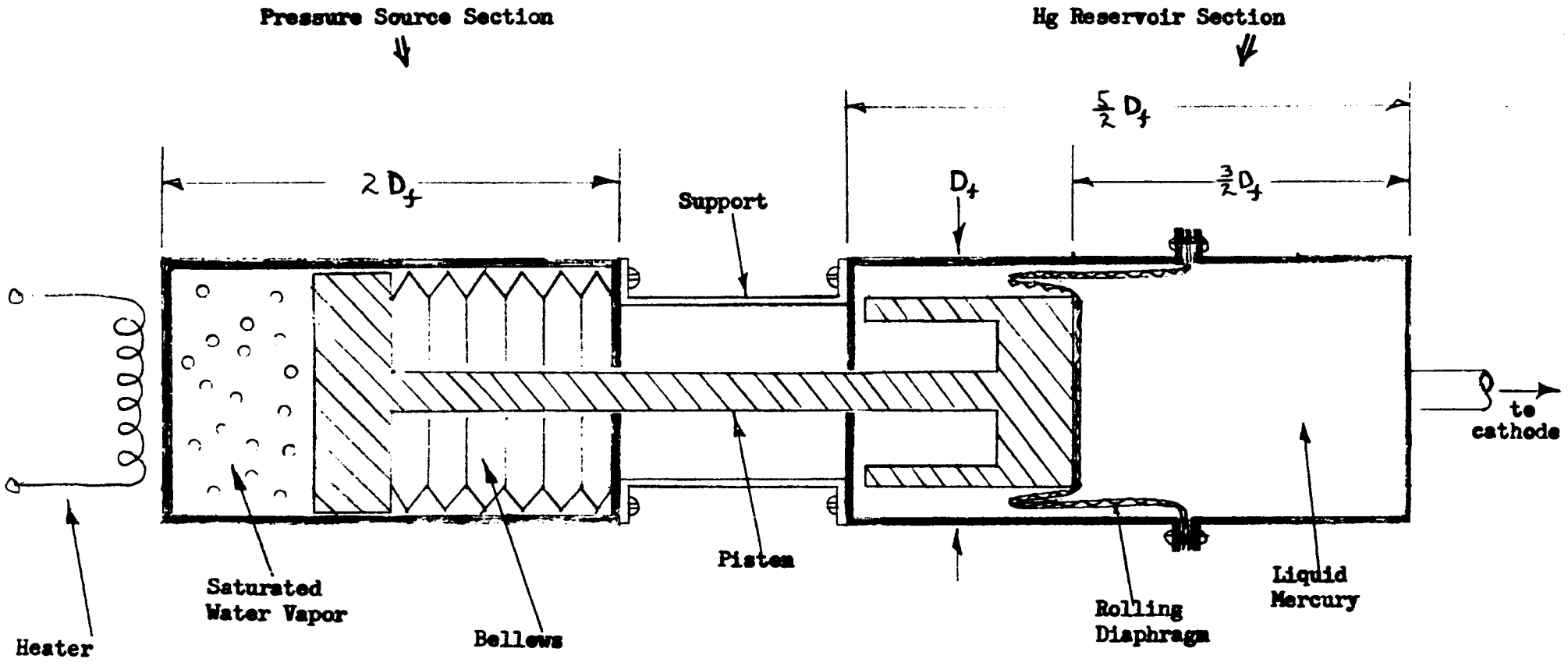

Fig. B.1-14. Vapor pressurized liquid mercury feed system for pool cathode engine.

$$\rho = 13.5 \text{ gms/cc.} = .03 \text{ lbs./cc.}$$

Therefore, the relationship between propellant mass stored M_p and feed system diameter is :

$$M_p = V\rho = (1.18 D_f^3)(.03) = .035 D_f^3 \text{ lbs.} \quad (26)$$

A plot of M_p vs. D_f appears in Fig. B.1-15. The corresponding thrustor module power level (P) for each value of propellant mass is obtained by :

$$P = 48 \left(\frac{M_p}{1600}\right) \text{ KW} \quad (27)$$

which is simply a relation arising from keeping the total power at 48 KW and total propellant at 1600 lbs. This correspondence between M_p and P is shown in the second scale super-imposed on Fig. B.1-15.

The weight of the feed system is mainly in the stainless-steel walls of the reservoir and pressure source containers. This weight is given by :

$$\text{Wt.} = \rho_s A_s t_f \quad (28)$$

where:

A_s = surface area of feed system
t_f = wall thickness = .060" = .15 cm
ρ_s = density of stainless-steel = 8gms/cc. = .018 lbs/cc.

The surface area is given by :

$$A_s = (\pi D_f)(2.5 D_f + 2D_f) = 14 D_f^2 \quad (29)$$

Hence, equation 28 becomes :

$$\text{Wt.} = (.018)(14 D_f^2)(.15) = 4 \left(\frac{D_f}{10}\right)^2 \quad (30)$$

Equation 30 is plotted in Fig. B.1-16. Using Fig. B.1-15, Fig. B.1-16 may be translated into a relation between module power leven and feed system weight (Fig. B.1-17). Specific weight is then shown in Fig. B.1-18.

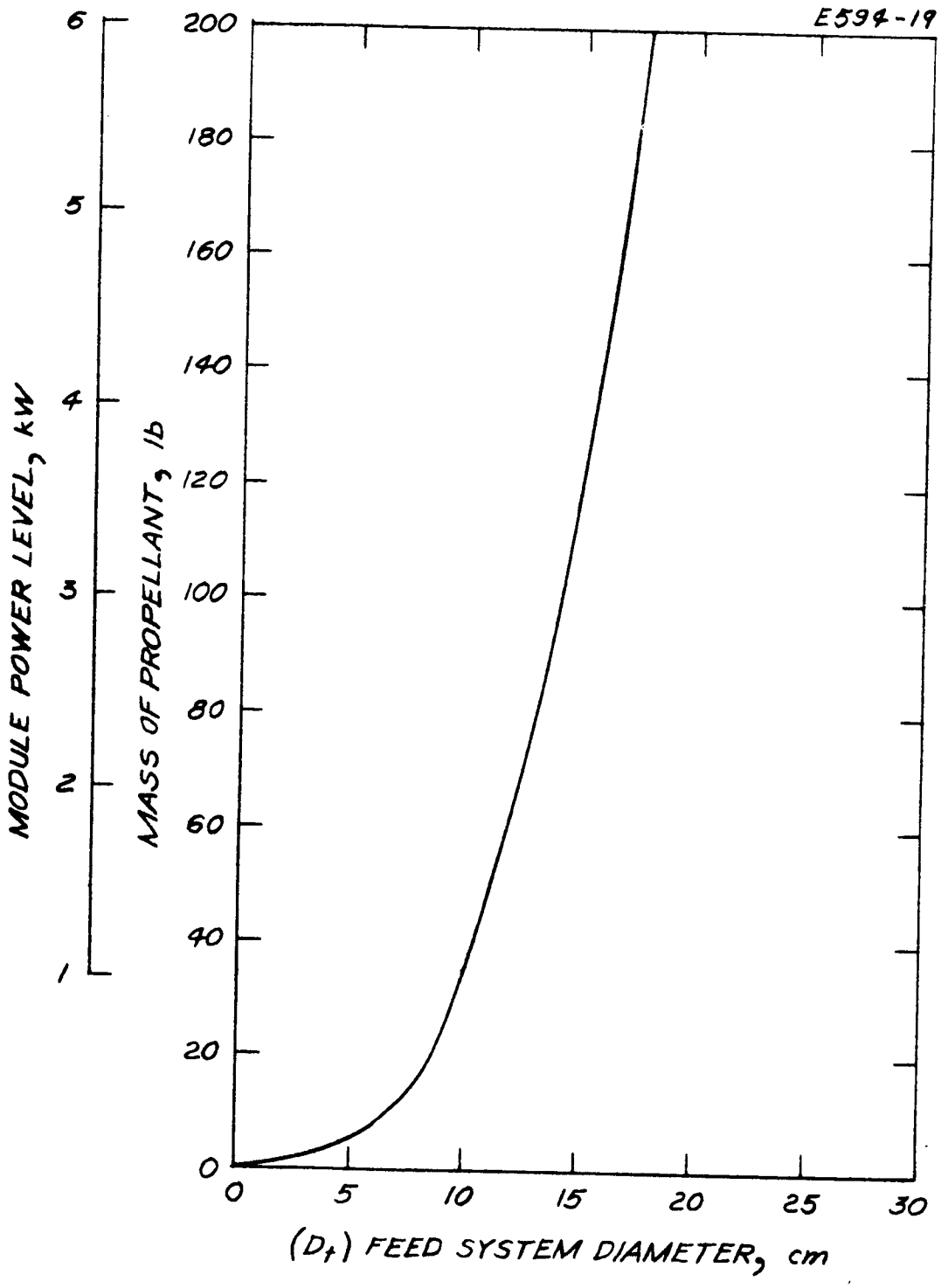

Fig. B.1-15. Mass of propellant versus feed system diameter for pool cathode engine.

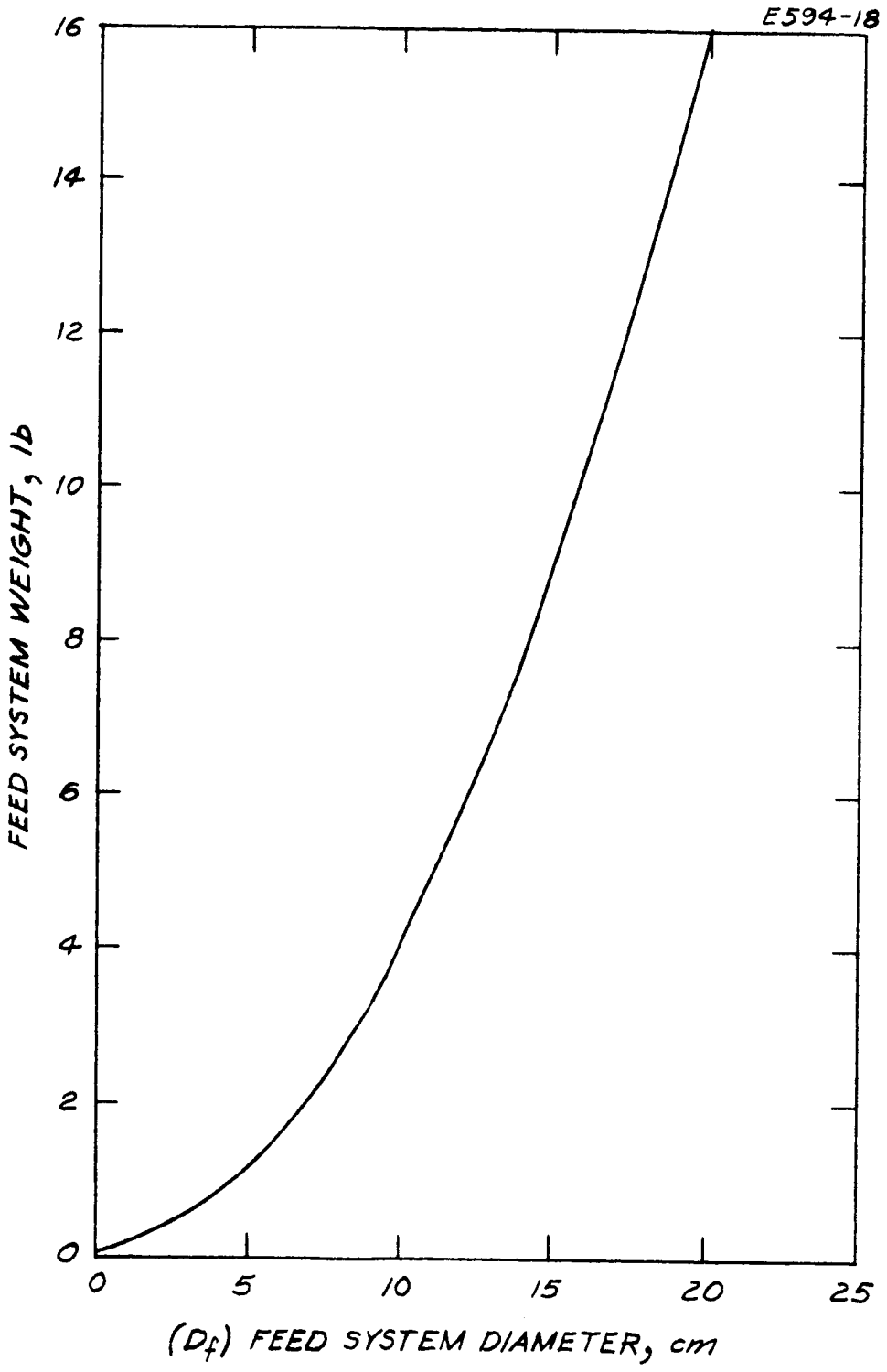

Fig. B. 1-16. Feed system weight versus feed system diameter for pool cathode engine.

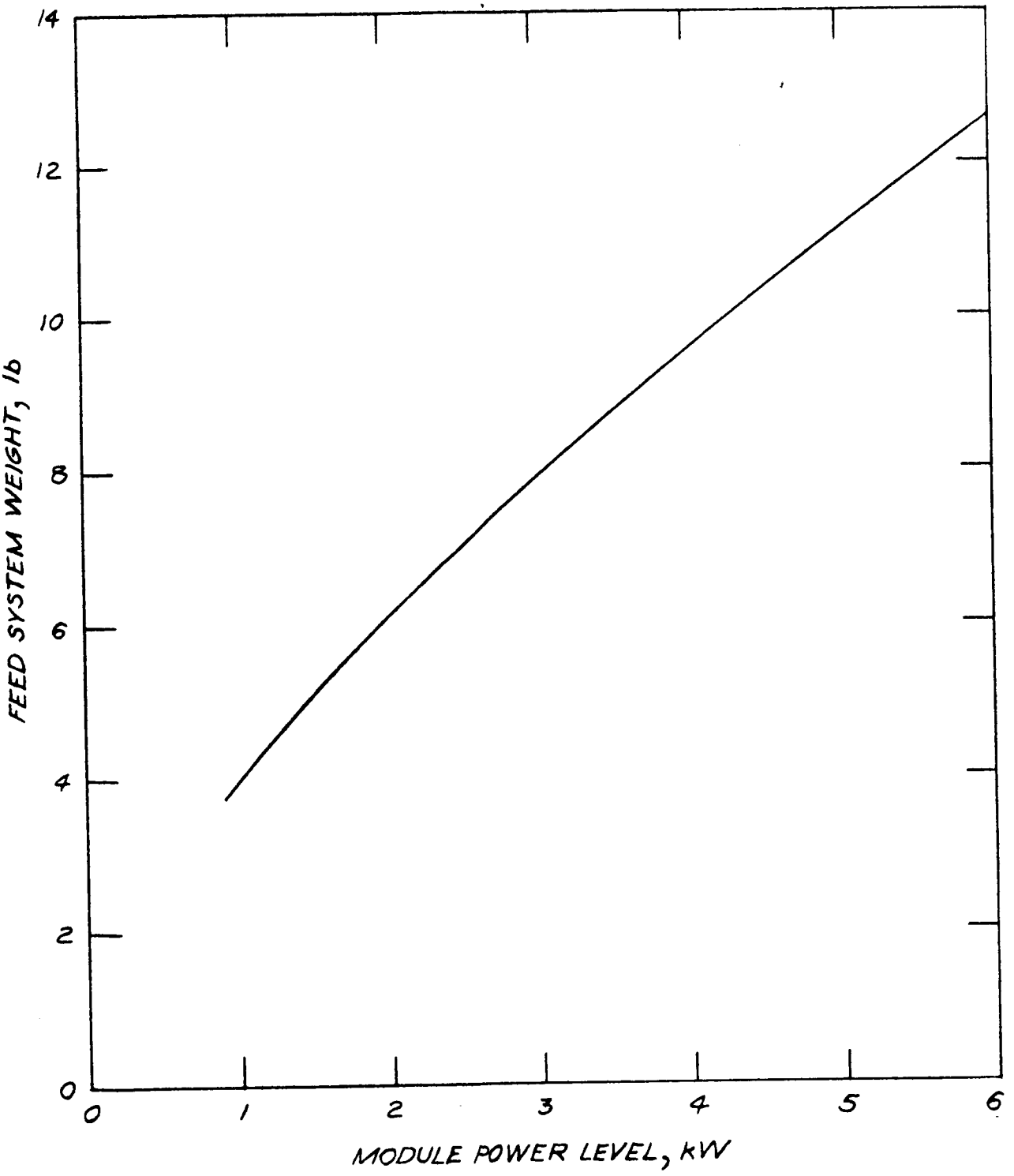

Fig. B.1-17. Feed system weight versus engine power level for pool cathode engine.

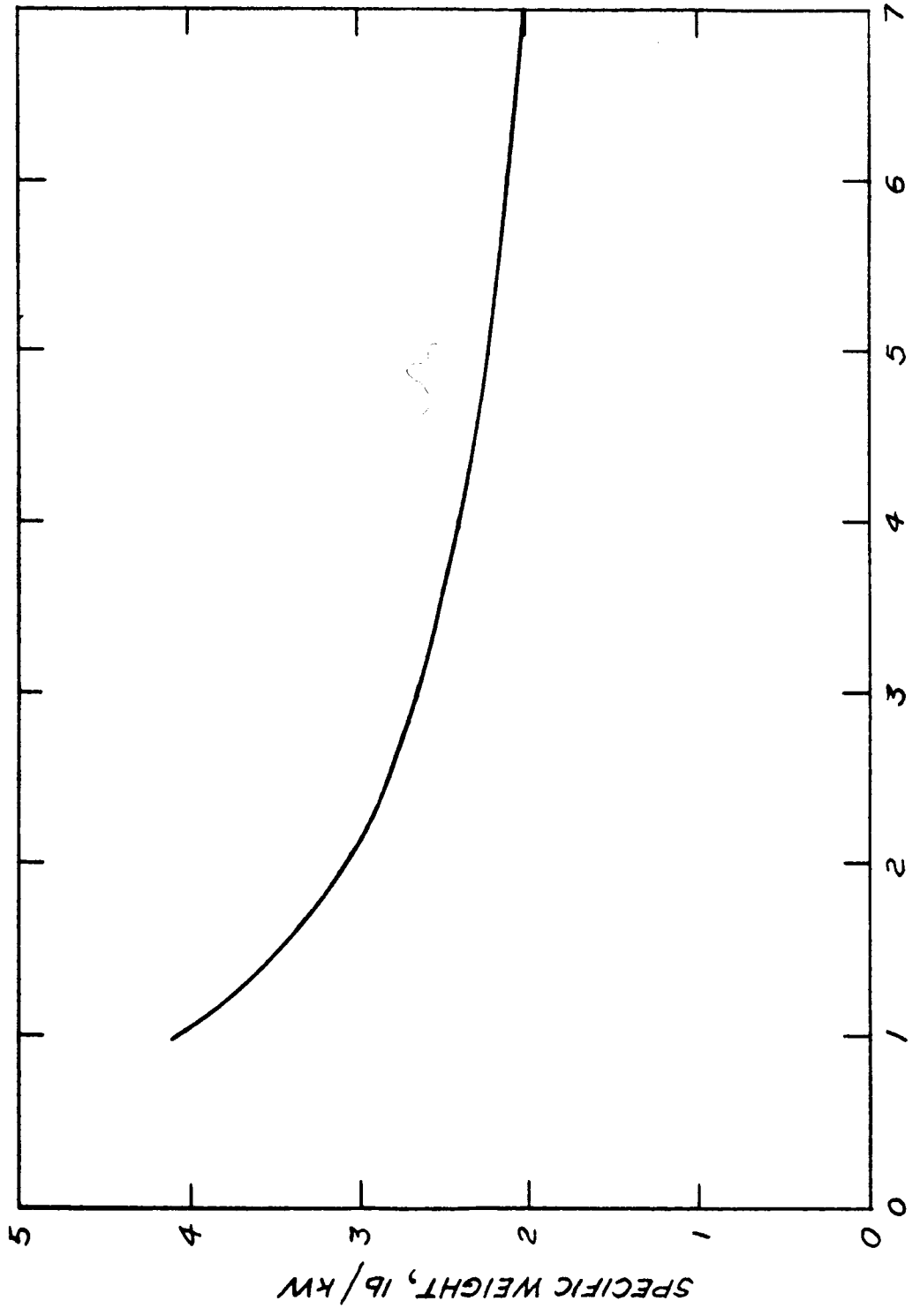

Fig. B.1-18. Feed system specific weight versus engine power level for pool cathode engine.

2. Conceptual Design of Pool Cathode Thrustor and Feed System Array

The conceptual design of the 48 KW system, incorporating a pool cathode thrustor is shown in Fig. B.2-1. A 6KW module size was chosen for convenience, although the optimum pool cathode engine size is not yet determined. Each thrustor has its own separate propellant source, as shown by the arrangement in Fig. B.2-1. This arrangement is necessary to satisfy the requirement for electrical isolation between thrustors. In order to isolate the electrical effects of one engine module from the others, it must be assured that no electrical path exists between engines. This design is directed at the elimination of the electrical path provided via the propellant feed system.

Pool cathode thrustor operation is characterized by a continuous stream of liquid mercury, starting at the propellant reservoir and running right into the thrustor. In other words, the propellant is not vaporized prior to entering the engine. Since liquid mercury is an electrical conductor, a continuous line of mercury connecting the thrustors would provide an undesirable electrical path.

Because of power-matching and reliability considerations, numerous combinations of operating and non-operating engines are possible during the mission. The propellant distribution scheme shown in Fig. B.2-2 will permit selectivity of engine operation while at the same time assuring electrical isolation of each thrustor. The system consists of a separate propellant reservoir for each thrustor, with the capability to exchange mass with other reservoirs. Without this capability for mass transfer, it was determined that the total system propellant required would more than double. With no propellant transfer capability, each engine would require enough fuel to operate during the entire mission. When an engine would be turned off because of power matching requirements, its remaining fuel would not be available to operating engines, but would be wasted. In addition, stand-by engines would require stand-by fuel. The following calculation demonstrates the excess weight penalty for not providing a propellant transfer capability.

A 6 KW module size is considered for convenience. A 6KW thrustor has an output of 2 amps, which corresponds to a fuel expulsion rate of:

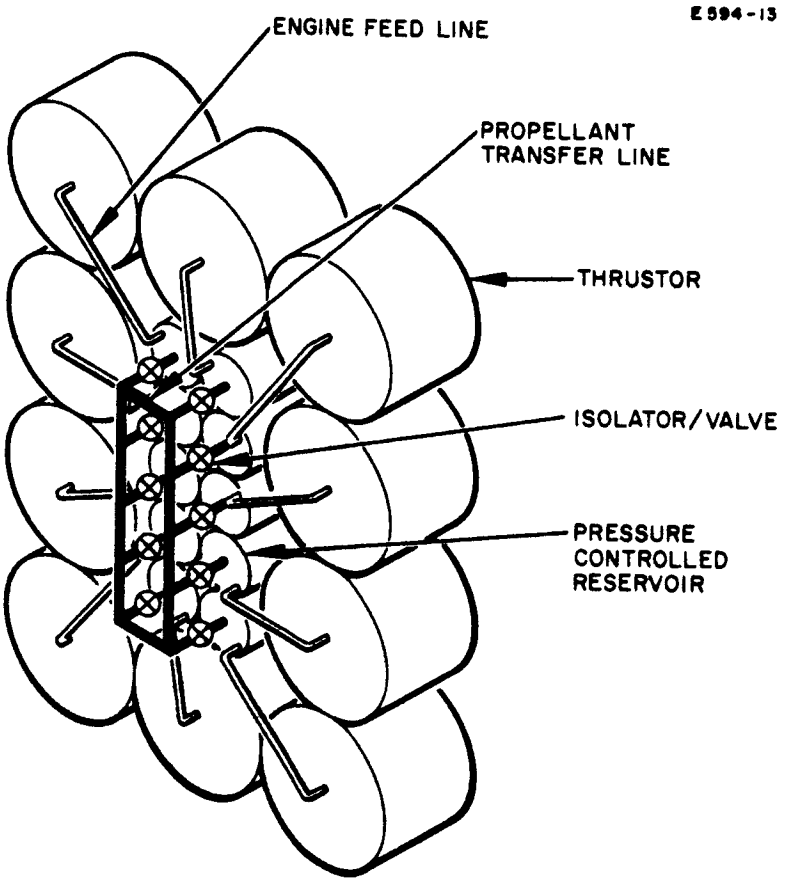

Fig. B.2-1. Conceptual layout of feed system and thrustors for 48 kW pool cathode engine system using 6 kW modules.

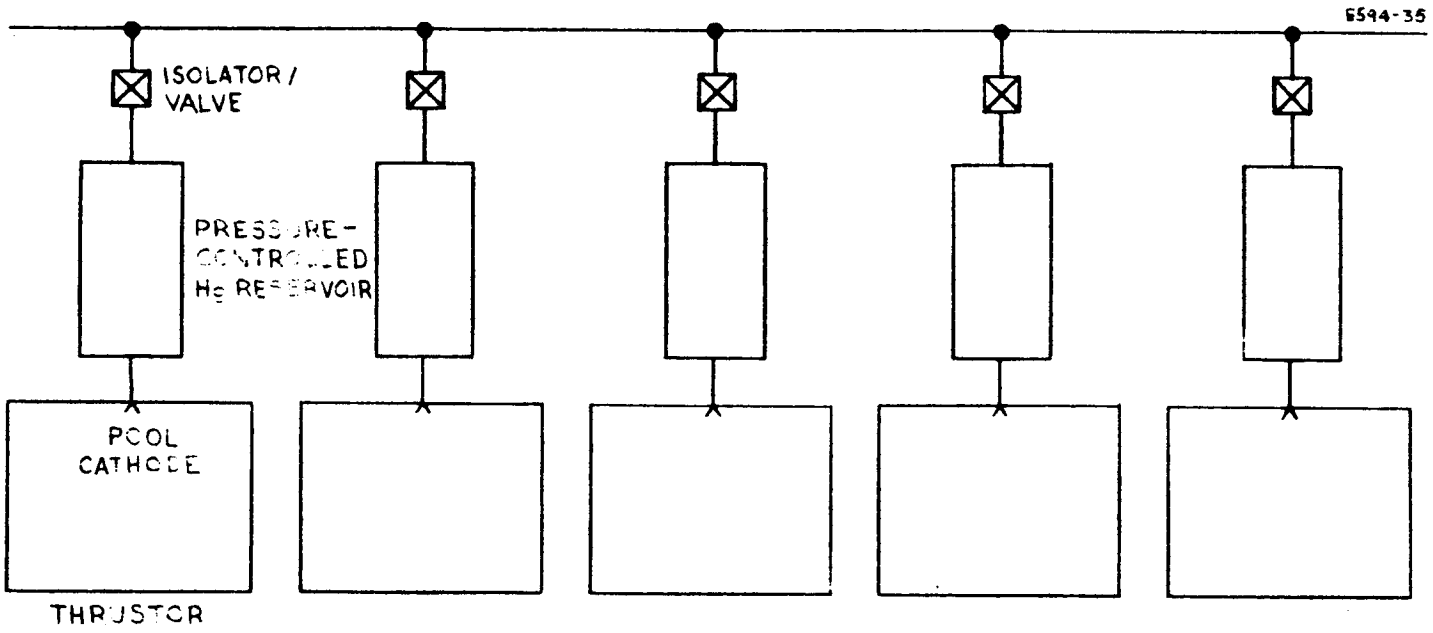

Fig. B. 2-2. Feed system for Hg pool cathode engines that provides electrical isolation.

$$\frac{2 \text{ coulombs/sec}}{1.6 \times 10^{-19} \text{ coulombs/particle}} = 1.25 \times 10^{19} \text{ part./sec.}$$

For an operating period of about one year :

$$\text{one year} \approx 10^4 \text{ hours} = 3.6 \times 10^7 \text{ seconds}$$

The mass required for each engine is then :

$$\text{mass/engine} = (1.25 \times 10^{19})(3.6 \times 10^7) = 4.5 \times 10^{26} \text{ particles.}$$

Since the molecular weight of mercury is 200 :

$$\text{propellant/engine} = \left(\frac{4.5 \times 10^{26} \text{ atoms}}{6.028 \times 10^{23} \frac{\text{atoms}}{\text{mole}}}\right)\left(\frac{200 \text{ gms}}{\text{mole}}\right)\left(\frac{2.2 \times 10^{-3} \text{lbs}}{\text{gm}}\right) = 330 \text{ lbs}$$

The total propellant required for all 10 engines (8 operating and two in stand-by) would be 3300 lbs. This is more than double the actual mission propellant requirement, which is only 1600 lbs. The need for propellant transfer capability is clear.

The interconnection of the propellant tanks and thrustor modules is shown schematically in Fig. B.2-2. In addition to the pressure-controlled reservoir, the only other auxiliary component required is an isolator/valve.

The pressure controlled reservoir is described in detail in Section B.1b. The reservoir is capable of maintaining the propellant at operating pressure (~50 psi) from the initial time when the reservoir is full to near the end of the mission when it is almost empty. In addition, the reservoir has the ability to expel and refill propellant to and from other reservoirs.

The isolator/valve is a normally closed dielectric valve that performs electrical isolation in the closed position. Thus, when mercury is not flowing across this valve, the thrustors are electrically isolated.

The propellant distribution process would proceed as follows:

1. A requirement to shut down an engine and transfer propellant arises (for example, due to a failure).
2. High voltage to that engine is turned off.
3. The isolator/valves of the turned off engine and a standby engine are opened.
4. Propellant is transferred from the tank of the turned off engine to the tank of the standby engine.
5. Both isolator/valves are closed.
6. High voltage to the standby engine is turned on.

The use of isolator/valves in this manner permits continuous operation of the other thrustors during propellant transfer.

3. System Integration Studies

The design of a modularized ion propulsion system poses many thermal, mechanical, and electrical integration problems which must be analyzed and solved prior to any specific definition of the capabilities and limitations of a high power ion propulsion system. The results of these propulsion system studies will have a substantial effect on the design of the various major subsystems as well as the overall spacecraft.

a. Thermal Integration of Thrustor Modules (Oxide)

The operating temperatures of a bombardment thrustor will generally be higher when the engines are clustered than when running separately. When a thrustor is operating alone (Fig. B.3-1(a)), it is free to reject heat from the entire surface area of the engine. On the other extreme,when in a close-packed array (Fig. B.3-1(b)), internal heat generation (arc power) can only be dissipated in the direction of thrust. Because of this reduction in heat rejection capability, thrustor temperatures in the latter case could be expected to rise an additional 200°C.

Under freely radiating conditions, the thrustor anode runs at approximately 500°C. This temperature was experimentally obtained during the thermal simulation described in Section B.1.a. With a 200°C increase due to the close-packed cluster effect, temperatures approaching 700°C might be expected. Referring to Fig. B.3-1(b), it is seen that the shells of the interior thrustors of a close-packed array approach the anode temperature.

For a permanent magnet thrustor, high engine shell temperatures are intolerable. The permanent magnets would be located on the engine shell, and would experience the same increased temperatures discussed above. The Curie point of permanent magnets, above which they lose their permanent magnetization, is considerably below 700°C. There is, therefore, a definite limit on the shell temperature of a permanent magnet thrustor. This problem is eliminated if a spread-out cluster is used, as shown in Fig. B.3-1(c).

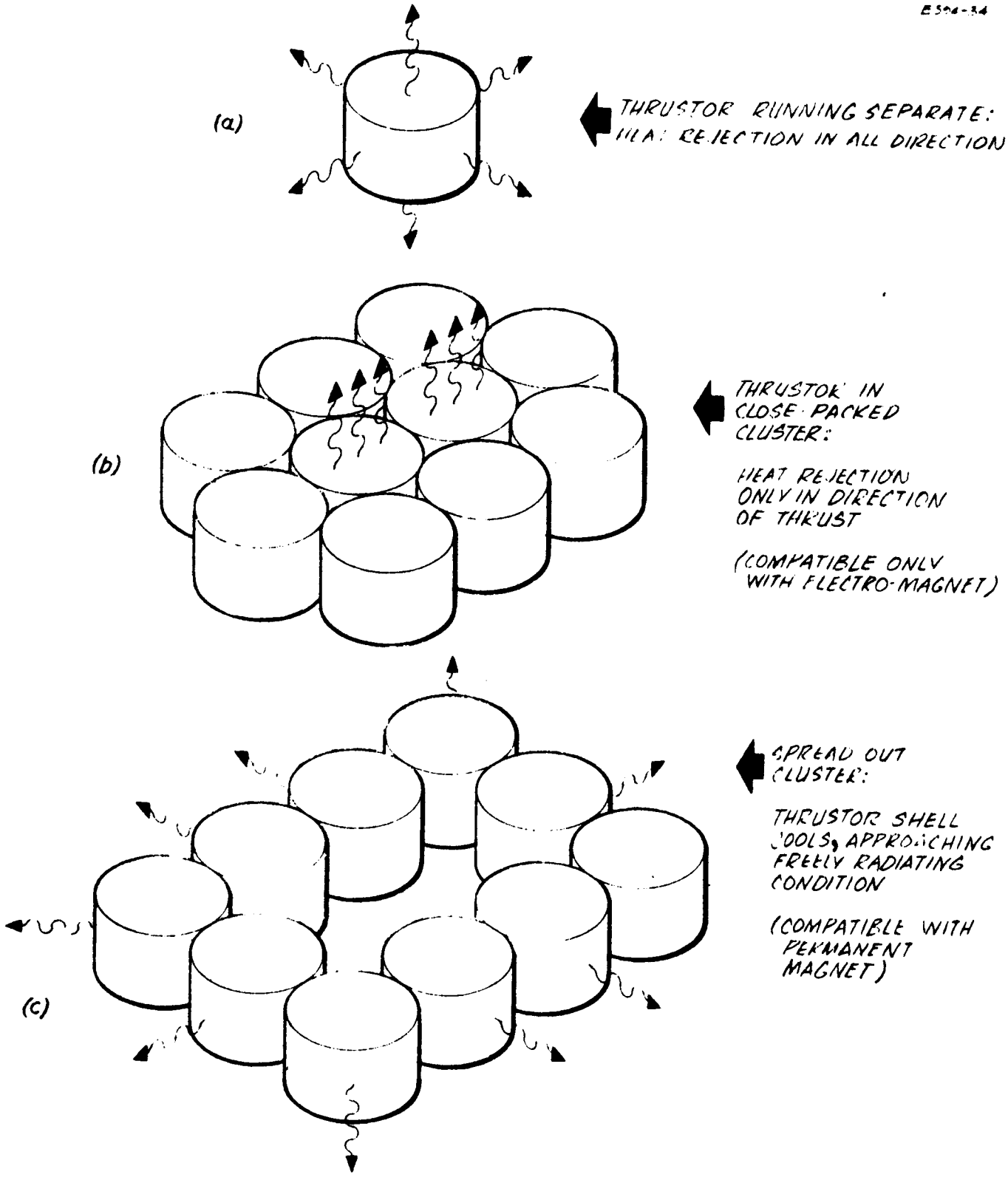

Fig. B. 3-1. Thermal considerations in clustering of thrustor modules.

Here, much of the thrustor surface is exposed to space, approaching the freely radiating condition.

A close-packed cluster is, however, compatible with an electromagnetic bombardment engine. In this case, the same temperature limit does not exist, since there are no permanent magnets. The engines may then be clustered as shown in Fig. B.3-1(b), with no degradation in performance.

The engine temperature, for an interior thrustor in a close-packed array, was calculated as follows. It was first assumed that heat could only be rejected in the direction of the ion beam, through the electrode holes. The holes in the screen electrode were equated to black-body radiating sources, with temperature equal to that of the engine interior. The accel electrode was considered to be a 50% effective radiation shield, impeding the rejection of heat from the thrustor to space. The solid surfaces of the electrodes were assumed perfectly reflective. The total heat being rejected (Q) is the sum of arc and cathode heater losses. For a 6 kW engine, this amounts to 1500 watts.

The following nomenclature is defined (I = radiation incident on a surface, D = radiation departing from a surface):

I_1 = thermal radiation back-scattered on the screen electrode holes

I_2 = radiation back-scattered on screen electrode surface

I_3 = radiation incident on accel electrode

I_4 = radiation incident on accel electrode holes (and rejected into space)

D_1 = thermal radiation departing from screen electrode holes

D_2 = back-scattered radiation reflecting from screen electrode surface

D_3 = radiation reflecting off accel electrode surface

Based on the foregoing assumptions, and using the above nomenclature, the following relationships are self-evident:

$$I_1 = I_2 = 1/2\, D_3 \tag{1}$$

$$I_3 = I_4 = 1/2\,(D_1 + D_2) \tag{2}$$

$$D_1 = \sigma A T^4 \tag{3}$$

$$D_2 = I_2 \tag{4}$$

$$D_3 = I_3 \tag{5}$$

where:

A = open area in screen electrode
T = interior engine temperature
σ = Stefan - Boltzman constant

Equations 1 through 5 are solved for I_4:

$$I_4 = \frac{2}{3}\, \sigma A T^4 \tag{6}$$

As noted above, I_4 represents energy incident on the accel electrode holes, and hence represents the total engine heat rejection Q:

$$Q = I_4 \tag{7}$$

Solving 6 and 7 for T:

$$T^4 = \frac{3}{2} \quad \frac{Q}{\sigma A} \tag{8}$$

For a 35 cm engine (where γ = ratio of holes to total electrode area $\approx .5$):

$$A = \gamma \ \frac{\pi}{4} \ (35)^2 \approx 500 \text{ cm}^2$$

Solving 8:

$$\left(\frac{T}{1000}\right)^4 = \left(\frac{3}{2}\right) \frac{(1500)}{(5.67)(500)} = .793$$

$$T = 944^{\circ}K = 670^{\circ}C$$

This is the estimated engine temperature for a close-packed array.

It may be noted that this resulting temperature is not dependent on module size. As seen from Equation 8, temperature is a function only of C/A. Since C is directly proportional to A (thrustor power is proportional to beam area), Q/A is a constant for any size engine.

$$Q/A = \text{const.} = 3 \text{ watts/cm}^2$$

b. Mechanical

A conceptual design of an ion engine system mounting structure is shown in Fig. B.3-2. In addition, a pictorial view of the thrustor array, propellant tankage and feed system is indicated. The basic system considered for the Saturn 1B/Centaur Spacecraft consists of ten (10) 6 kW, 35 cm. diameter, Hg bombardment thrustor modules, eight (8) 10-1/2 inch. diameter, spherical propellant reservoirs plus associated valves, flow meters, vaporizers, isolators and plumbing.

The arrangement presented herein assumes each thrustor module will be 50 cm. in diameter to account for thrustor components extending beyond the 35 cm. basic thrustor diameter. The ten thrustors are arranged in three rows of 3, 4 and 3 thrustors per row. The propellant tanks are situated aft of the thrustor modules thereby permitting close grouping of thrustor rows and minimizing frontal area. Minimizing frontal area results in proportionately reducing the spacecraft bus "window" for the ion exhaust beam. Although numerous arrangements are possible in the routing of the components and plumbing from tankage to thrustors, the arrangement depicted was prepared attempting to contain the feed system envelope within the frontal envelope of the thrustor array.

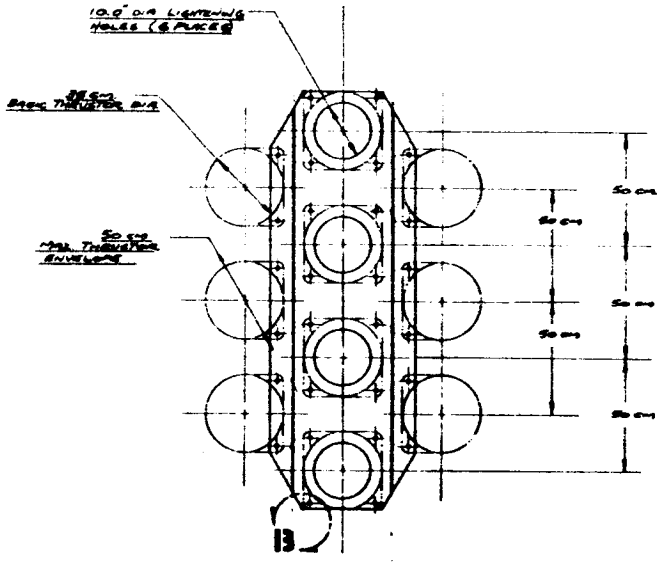

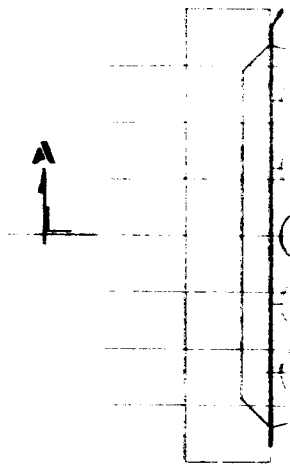

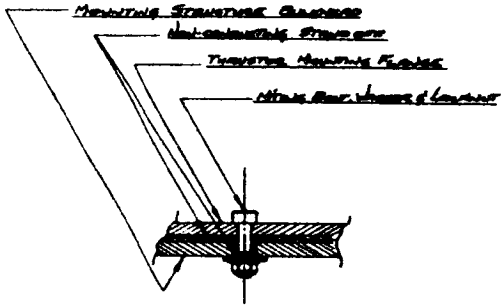

DETAIL B

FULL SIZE

TYPICAL 2 PLACES ON OUTBOARD THRUSTER
4 PLACES ON CENTER THRUSTER

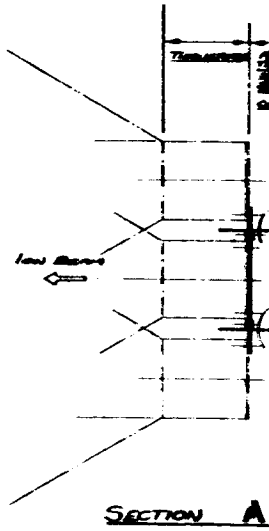

SECTION A

Figu

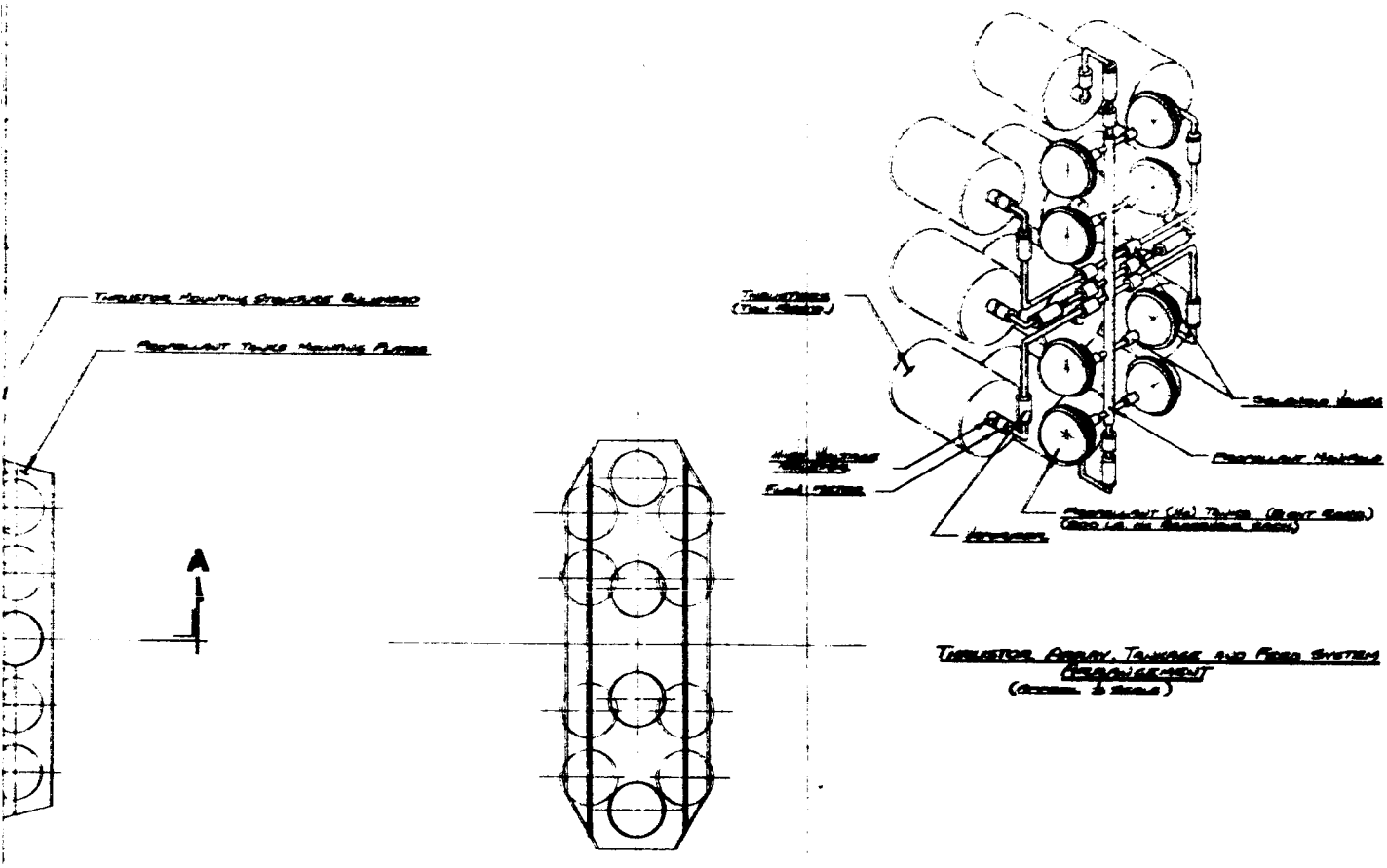

B.3-2 Ion Engine System Mounting Structure

The mounting structure shown consists of a mounting panel to which the ten thrustors are attached using electrical insulating mounting pads and nonconducting standoff attachments. The thrustor mounting panel may be made of aluminum alloy sheet to which are attached two additional plates which serve as support structure for the Hg tanks. A central feed line or "propellant manifold" is located between the two rows of 4 tanks which provides convenient routes to all 10 thrustors. A closure bulkhead aft of the tanks provides a mounting surface for the entire engine package to the spacecraft. The entire envelope is approximately 5 feed wide by 7 feet high by 2-1/2 feet in depth.

Preliminary sizing of the above prescribed mounting structure indicates that utilizing state-of-the-art methods, it could be constructed to be well within five (5) percent of the total ion engine system weight (including propellant) of approximately 2000 lbs. Fabricated aluminum construction was assumed.

The ion engine system mounting structure, in addition to mechanically integrating the engine system, must meet three specific mission requirements, namely:

(1) Survive the boost environment

(2) Provide the capability of being able to orient the thrust vector in 2 degrees of freedom (longitudinally and laterally) to correct for S/C, c.g. - thrust vector misalignments during transit to Mars and,

(3) Permit jettisoning of the entire system upon Martian approach and S/C retro maneuver.

A structural support arrangement which could satisfy all three requirements does not appear attractive since mechanisms to provide capabilities (2) and (3) would be penalized by having to be structurally adequate to survive the high loading (6.5 g's longitudinal and 2.0 g's lateral) imposed during boost. The present design philosophy adopted is to by-pass the engine array translation device and jettison device by caging the entire engine array to the spacecraft structure with an independent support system which would be disengaged once the S/C is in a zero-g environment. Conceptual designs of the above mentioned mechanisms are presently being prepared and will be presented in the final report.

From a spacecraft configuration standpoint, it is desirable to be able to mount the ion engine system external to the spacecraft. External mounting eliminates the need for the structurally undesirable "window" in the bus. It also increases the translation capability for thrust vector-spacecraft c.g. corrections. In addition to the structural and operational advantages listed above, external mounting also facilitates pre-launch maintenance of the engine array. Packaging the engine system in an envelope which would appear as a thin long slab would facilitate mounting the package external to the spacecraft. An arrangement which locates the Hg tanks in the plane of the thrustors in order to minimize the depth of the envelope will be considered in future studies.

c. Electrical

As has previously been shown, the ion propulsion system for the design mission consists of ten ion thrustors and eight independent power conditioning panels. As part of the electrical integration of this system, therefore, consideration must be given to the cabling which connects the power conditioning panels to the thrustors and the switching matrix which allows the transfer of a power conditioning unit to a standby thrustor.

1) Transmission Cable

The electric propulsion system requires an electrical power transmission cable to interconnect the power conditioning and ion engine systems. For the design mission, the transmission cable associated with each of the eight power conditioning panels must have a power handling capability of six kilowatts. The cable must be able to transmit this power at ion engine potentials and currents with reasonable cable power efficiencies and specific weights.

In the 48 kW propulsion system design, eight power transmission cables must be routed from the power conditioning panels to the ion engine modules. In addition, a switching matrix and a cable harness is required to permit the operation of standby ion engines from any one of the eight power conditioning panels. A flexible cable mounting is required to allow the ion engine

array to be translated in two directions during the course of the mission to accommodate a shift in the thrust vector. Also squib actuated cable connectors must be provided to permit disconnecting and jettisoning of the power conditioning panels and ion engine modules at the end for the heliocentric phase of the trajectory. Figure B.3-3 is a drawing of the proposed flexible ribbon power transmission cable. The cable is fabricated from strips of copper foil and would be sandwiched between two layers of teflon film. Approximately eight separate conductors would be required for each individual ion engine. Each copper conductor or strip would require a voltage isolation potential of 100 volts between conductors and 3000 volts between each conductor and ground. Figure B.3-4 indicates the layout of the cable for two thrustor arrays which allows operation of interconnect harness, eight primary ion engines, and two standby ion engines with eight power conditioning panels. As shown, the average length of the transmission cable system is approximately 10 feet.

The detailed cable design is dependent on the ion engine cable conduction current requirements. Table B.3-I is a detailed breakdown of power supply requirements for both the oxide cathode and pool cathode ion engines. Two methods of connecting the power conditioning to the ion thrustor are considered. In case A (Fig. B.3-5), ion engine supply polarities are not considered. In this design, both the high voltage and common ground conductors would require current carrying capacity equal to the sum total of all the ion engine supply currents. In case B, engine polarities are considered and are arranged to minimize the current carrying capacity requirements of the common conductors. In both cases, it is assumed all the ion engine supplies would be d.c. The transmission cable current conduction requirements are seen to vary between 82 and 135 amperes for typical six kilowatt ion engine systems.

Figure B.3-6 shows the resistance and power loss as a function of cable cross sectional area for a 10 foot long ribbon cable. The I^2R power losses are given for cable conduction currents of 82, 94, 97 and 135 amperes. An optimization of

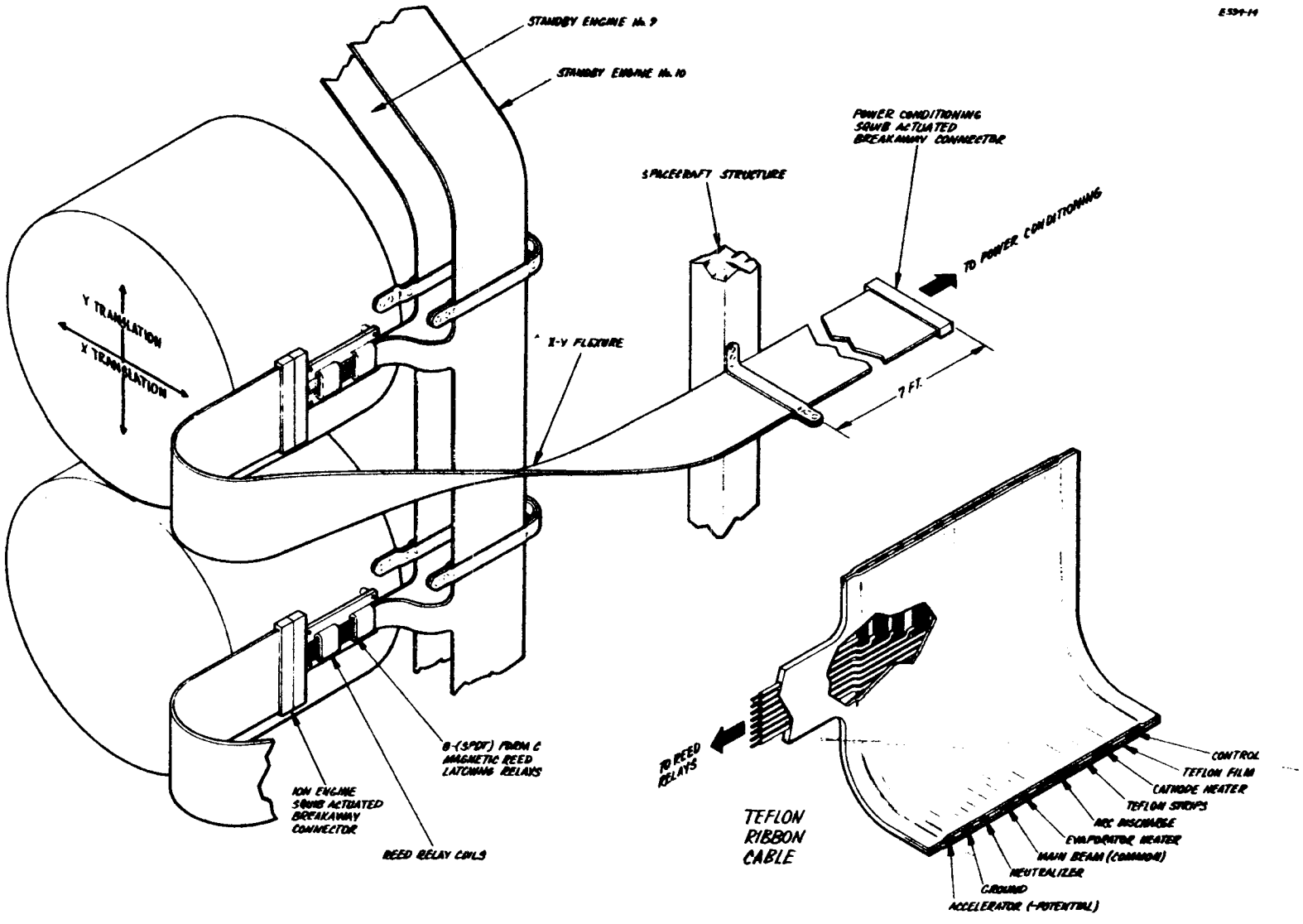

Fig. B.3-3. Ion engine-power conditioning interconnection details.

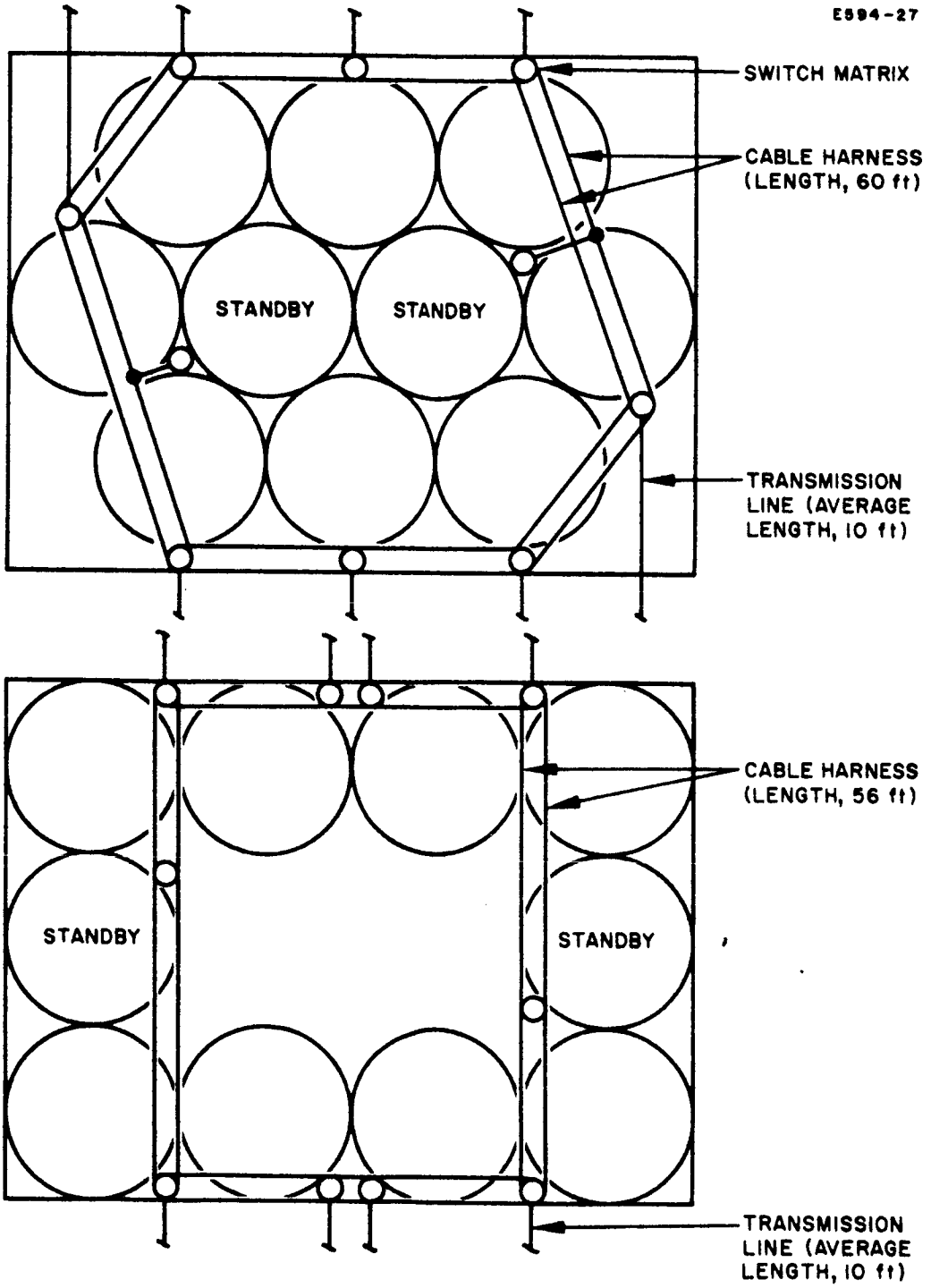

Fig. B. 3-4. Engine array power cabling.

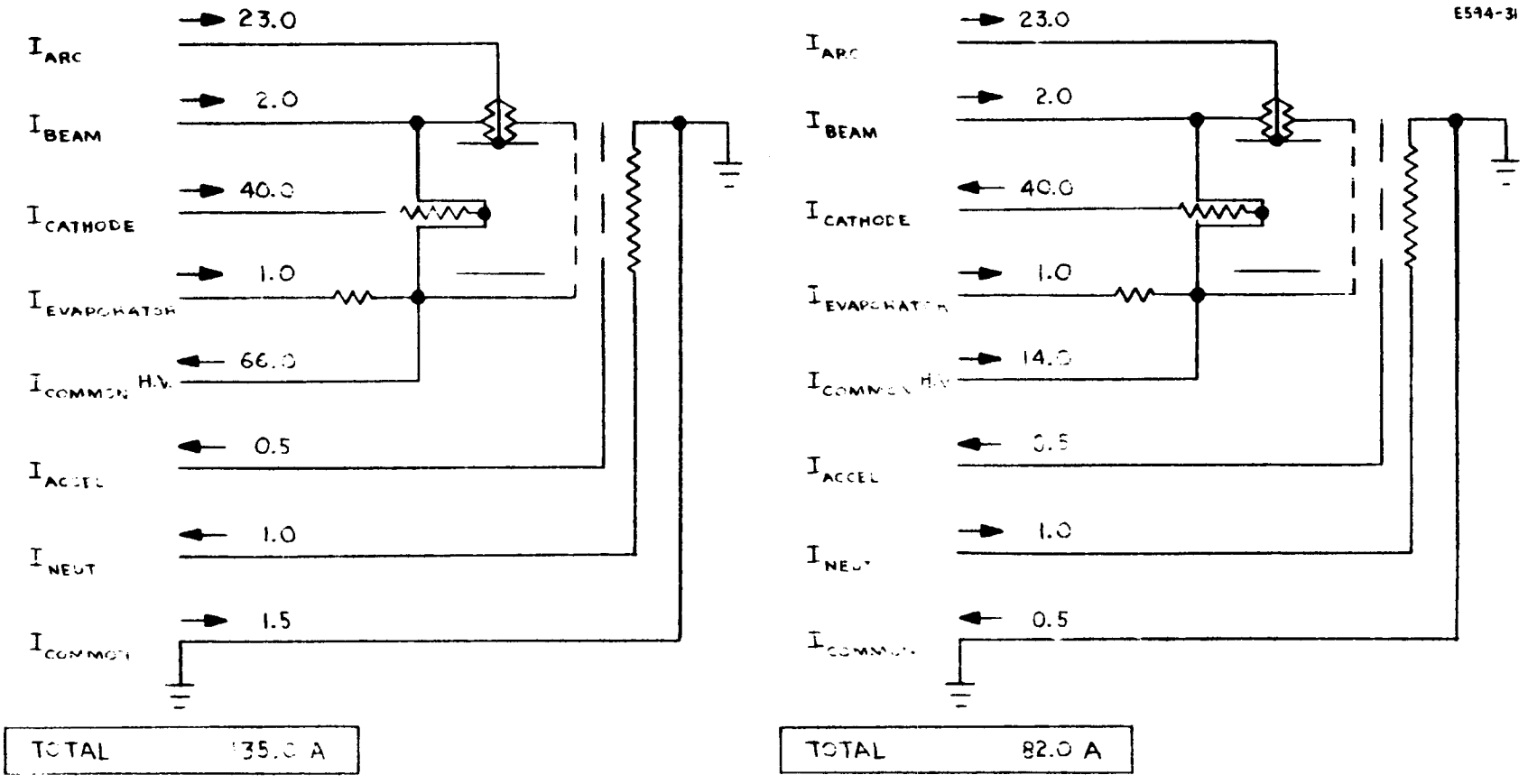

Fig. B.3-5(a). Power conditioning — thrustor current paths.

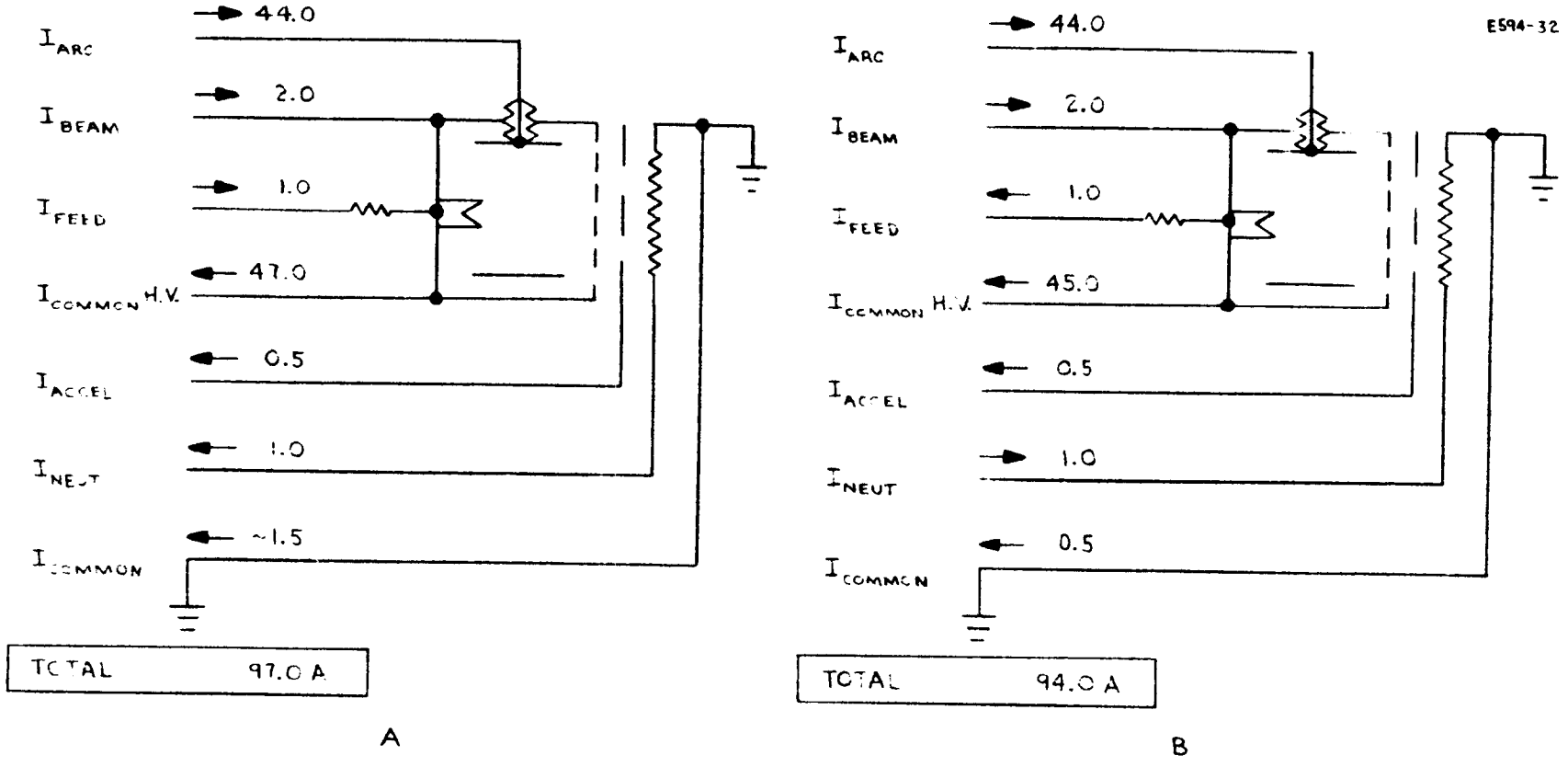

Fig. B.3-5(b). Power conditioning — thrustor current paths.

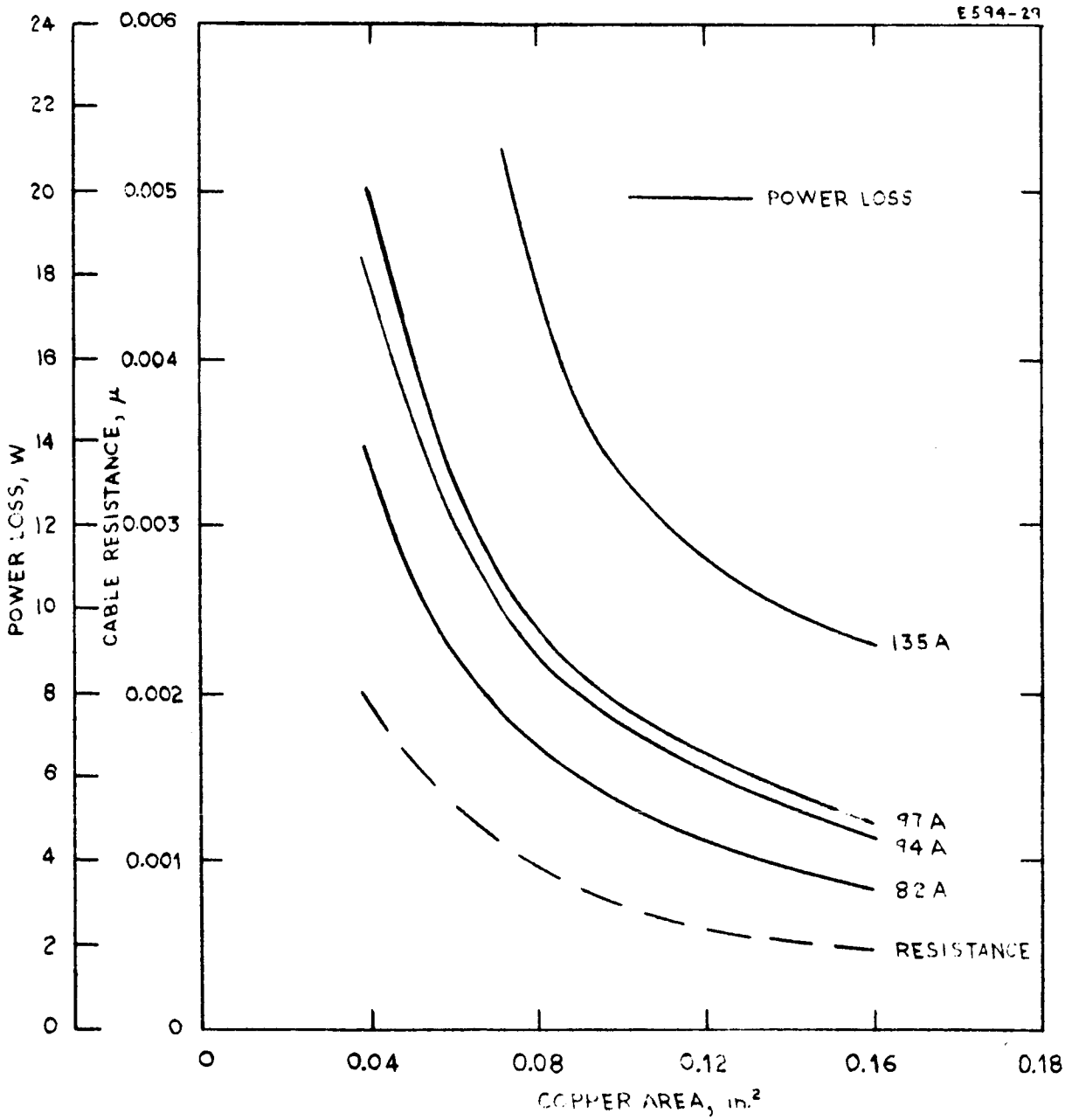

Fig. B.3-6. Ribbon transmission cable electrical characteristics (10 ft cable length).

cable weight is shown in Fig. B.3-7. In general, two weight penalties must be considered. The first is the cable weight versus copper cross sectional area. The second is the weight penalty associated with the I^2R power loss of the cable system. In this latter case, it is assumed that the solar cell system must make up the cable power loss at a weight penalty of 50 lbs/kilowatt. By adding these two curves, the total system weight penalty associated with the ribbon transmission cable can be determined. The minimum weight cable systems for each of the required conduction currents for the ion engine systems are shown in Fig. B.3-8. The maximum cable specific weight is seen to be less than 1 lb/kilowatt for a 10 foot long cable even when designed for an ion engine system that requires a cable current carrying capacity of 135 amperes.

An additional feature offered by a ribbon cable is the possibility of building in a cable capacitance with zero cost in system weight. By vapor depositing a metal film on the outside of the teflon film and connecting this film to spacecraft ground a relatively large capacitance can be built into the system. Assuming the teflon film is .015 inches thick, has a dielectric constant of $k = 2$, and has an area 5 inches wide and 10 feet long results in a cable capacitance of .04μf. This capacitance can be used for filtering and smoothing the ripple associated with d.c. power supplies. Further, the cable capacitance will bypass any high frequency voltage transients generated by ion engine arcs. The cable capacitance will effectively protect the power conditioning system from over voltage transients during ion engine arcing.

2) Switching Circuitry

The power conditioning and ion engine reliability study was undertaken to determine the optimum engine size and the number of redundant systems necessary to meet mission reliability requirements. This study indicated, that for a 48 kilowatt solar power ion propulsion system, the optimum engine size would be six kilowatt. The system would require eight power conditioning systems, and ten ion engine systems. At the start of the mission, eight power conditioning and ion engine systems would be in operation with two ion engines in

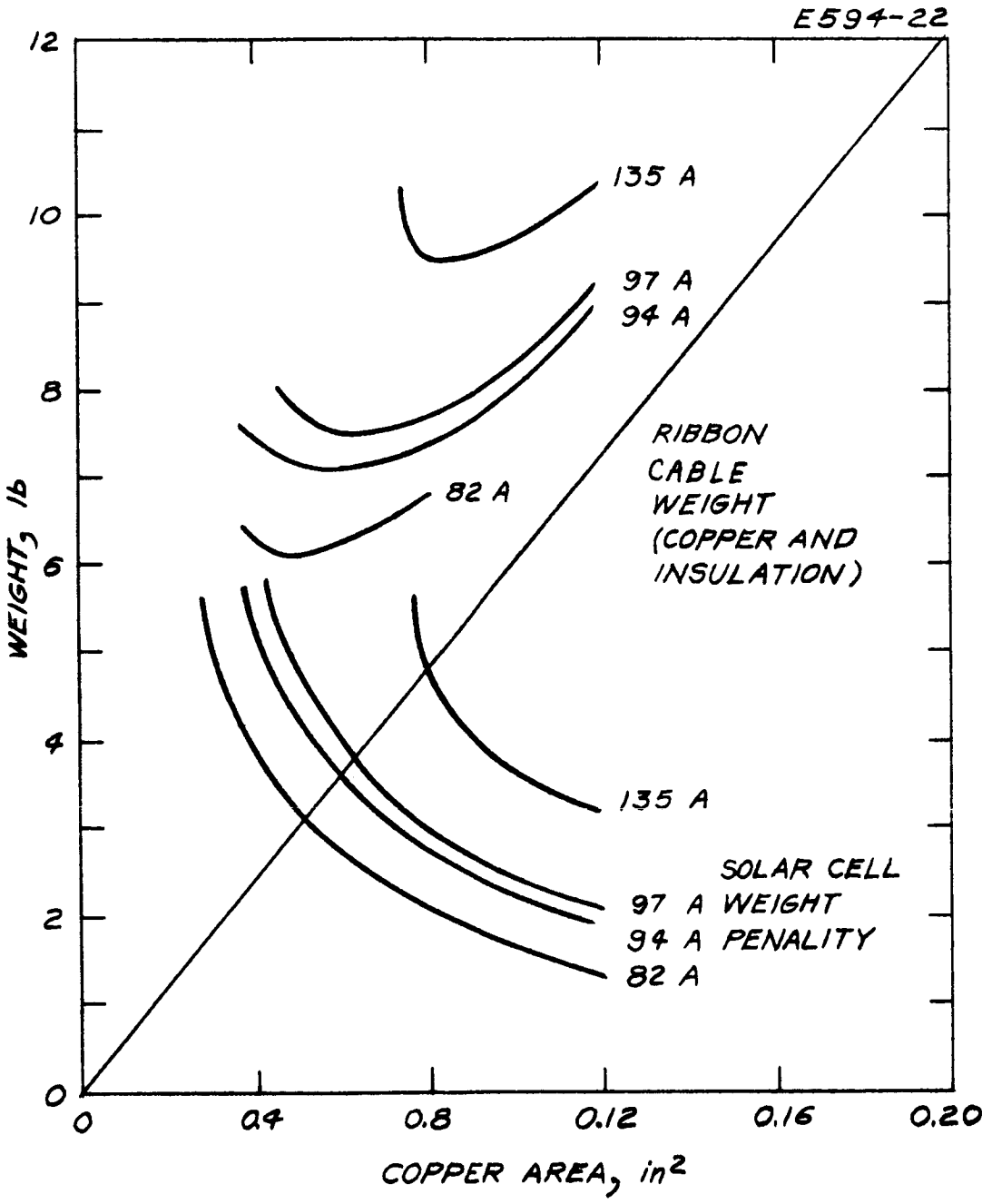

Fig. B.3-7. Transmission cable weight optimization curves.

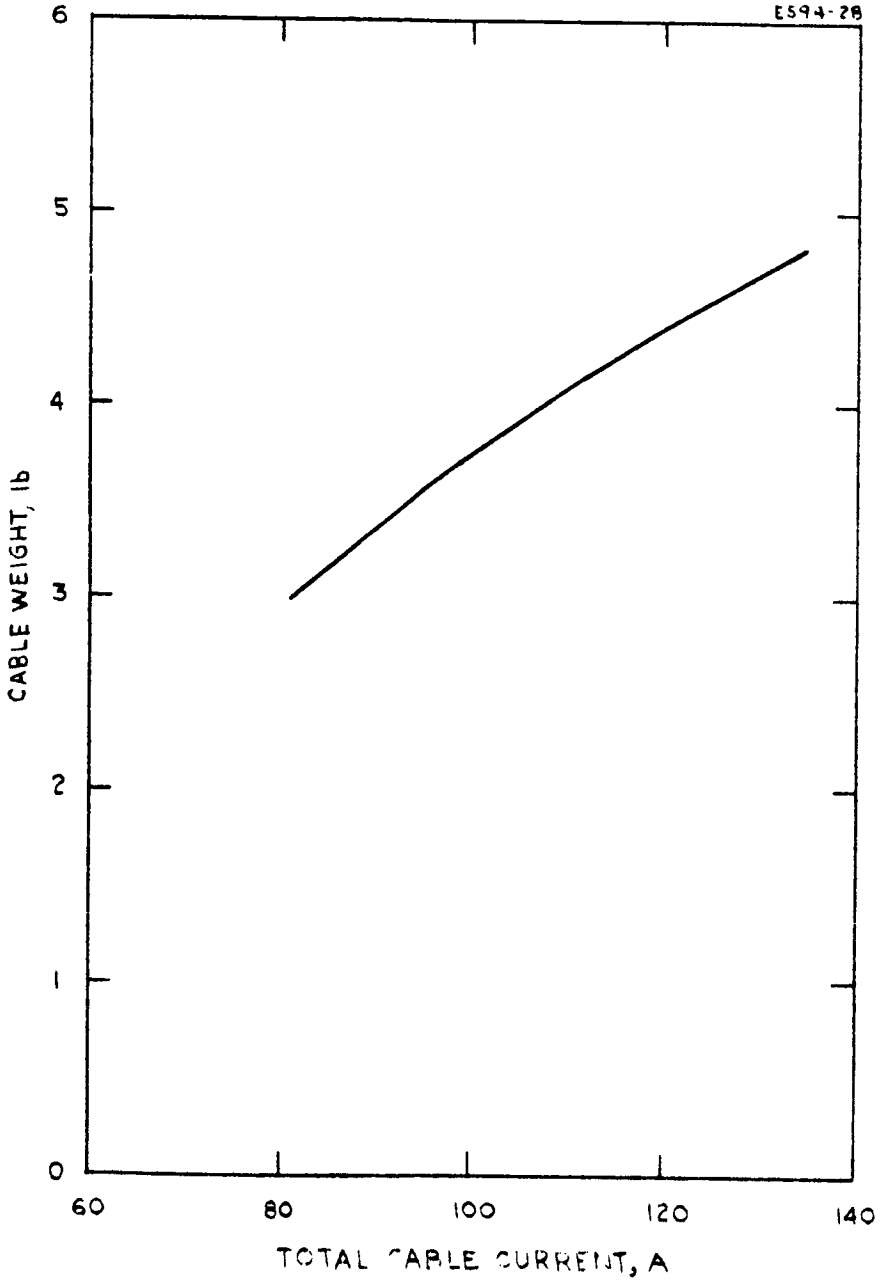

Fig. B. 3-8. Weight of 10 ft transmission cable versus total cable current.

TABLE B.3-I

Ion Engine Power Requirements

Oxide Cathode Engine (6 kW)

Supply	Power (watts)	Voltage (volts)	Current (amps)
Arc Discharge	920	40	23.0
Evaporator	50	50	1.0
Cathode	400	10	40.0
Main Beam	4400	2200	2.0
Neutralizer	50	50	1.0
Accelerator	120	2200	~0.5

Pool Cathode Engine (6 kW)

Supply	Power (watts)	Voltage (volts)	Current (amps)
Arc Discharge	1320	30	44.0
Feed System	50	50	1.0
Main Beam	4400	2200	2.0
Neutralizer	50	50	1.0
Accelerator	120	4400	~0.5

standby. As the mission progresses, solar electrical power output would decrease so that power conditioning and ion engine systems would be shut down. At the end of the mission, only five power conditioning and ion engine systems would be required to be in operation.

With the above constraints, the basic problem is to determine the optimum switching circuitry required to interconnect the power conditioning system to the eight operating and two standby ion engine systems. The basic assumptions used in optimizing the switching circuitry are:

i The reliability of the power conditioning system using the multi-module approach can be raised internally through the use of standby power conditioning modules. (There will be no requirement for a complete standby power conditioning system since the reliability of the individual power conditioning systems can be increased to any desired reliability.)

ii The reliability of the ion engine system can only be increased through standby redundancy techniques.

Based on these assumptions, the standby ion engine systems will not require separate power conditioning systems. When one of the eight operating ion engine systems fails, the power conditioning system will automatically be turned off and the failed ion engine will be switched out of the circuit, subsequently, one of the two standby ion engines will be switched in and the power conditioning will be automatically re-started. Figure B. 3-9 shows a switching circuit which satisfies this constraint. It is the simplest possible switch circuit that can be employed to permit the two standby ion engines to be connected to any of the eight power conditioning systems. The circuit shows the use of 16 transfer switches. In practice, when an ion engine is switched, a total of eight electrical circuits will have to be transferred.

An ideal switch for transferring power between operating and standby ion engine systems would be a glass reed switch. The switch is reliable and has a fast response time. The switch requires zero power to hold the contacts closed if used in a latch reed relay configuration. A pulse to a coil of one polarity closes one set of contacts, a pulse to the

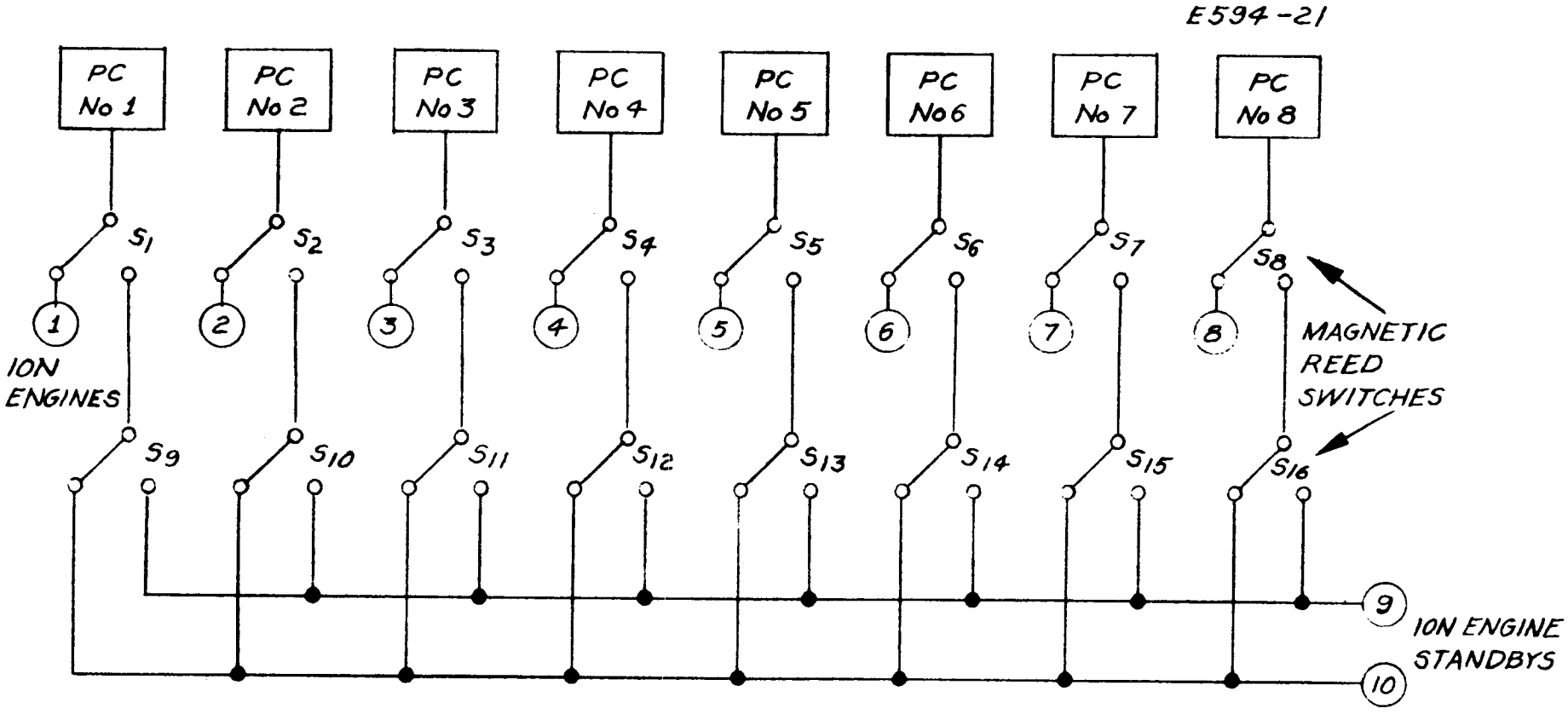

Fig. B. 3-9. Ion engine — power conditioning switching matrix.

same coil of the opposite polarity closes another set of contacts. A latching magnet holds the contacts closed requiring zero coil holding power. The basic glass reed switch consists of overlapping flat cantilevered reeds of ferromagnetic material surrounded by an inert gas or vacuum and sealed in a glass envelope. A small air gap separates the free overlapping ends of the reeds. When a magnetic field is generated parallel to the reeds, the magnetic induction causes the reeds to attract and close. The magnetic reeds are plated with a precious metal which acts as the contact and current path. The arms produce a snap action caused by the rapid flux increase between the contact surfaces as they travel toward each other. After closure, a high contact pressure results from the small non-magnetic gap and the high flux density between the contact surfaces.

Figure B.3-10 shows the switch circuitry required to connect one power conditioning system to one of three ion engine systems. As shown, two eight pole double throw switch relays are required. In this system, the pulse coil surrounds all eight reed switches. Pulsing the coil causes all eight reed switches to close simultaneously. When the reed contacts are closed, the magnetic latching magnet holds the contacts closed until a pulse of opposite polarity resets the switch contacts. In this system, the contacts would not be required to switch any current. If an ion engine failed, the power conditioning would be turned off. The failed ion engine would be switched out and a new ion engine would be switched in its place. The switch operation would be performed at zero power. In operation, the switch would require a voltage isolation between switch contacts equal to the ionizer or accelerator electrode potentials.

Standard, commercially available magnetic reed switches are measured and classified in terms of the open and closed electrical rating of the switch contacts. In the open state the important parameter is the voltage isolation rating of the contacts. In the closed state the important parameter is the maximum current rating of the contacts. In the dynamic or switching state the important parameter is the volt ampere or wattage rating of the circuit power the switch can interrupt without excessive arcing or wear. Table B.3-II compares the state of the art of reed switches with the ion engine switch requirements.

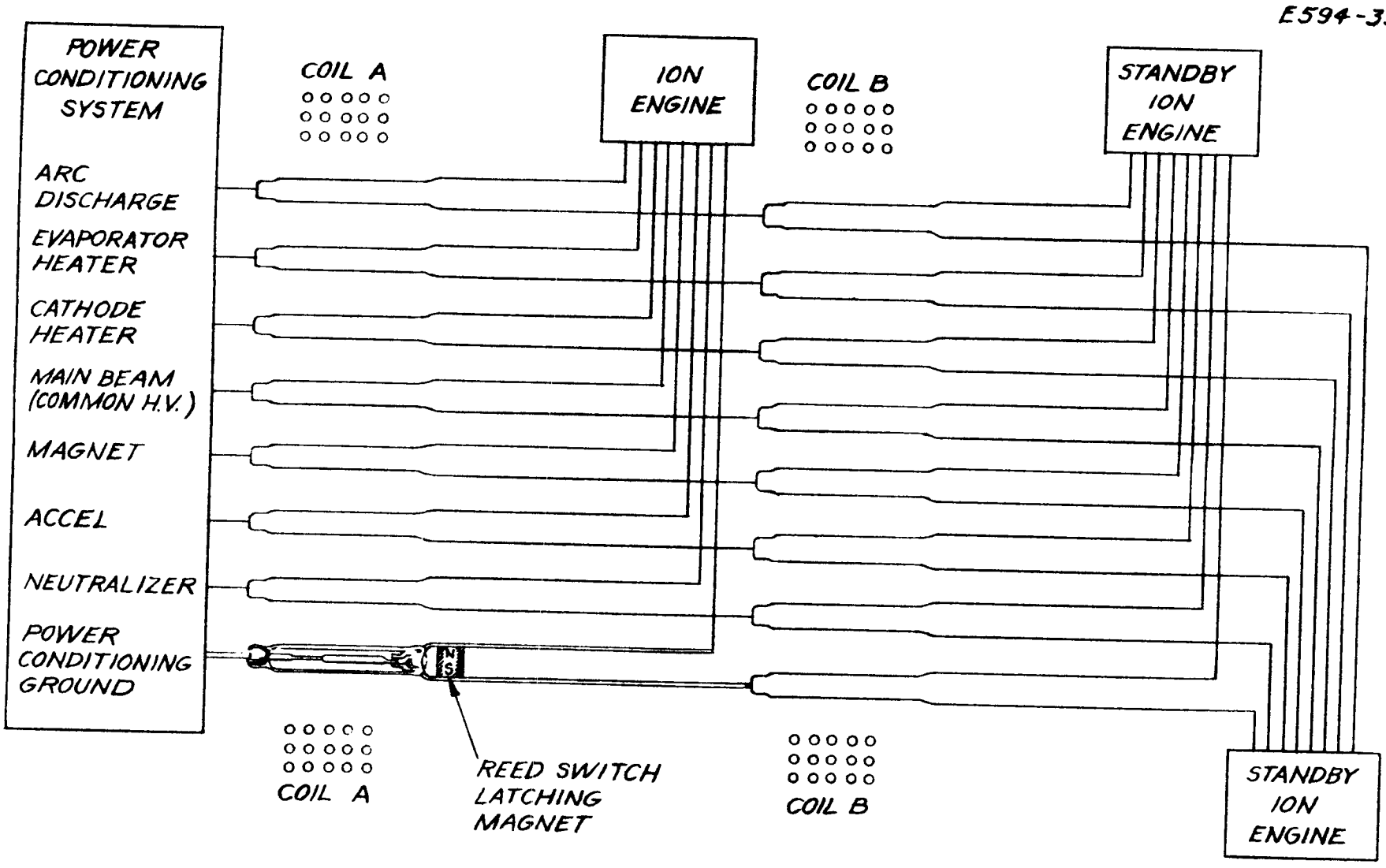

Fig. B. 3-10. Magnetic reed switch circuitry.

TABLE B.3-II

Magnetic Reed Switch Requirements

Type Switch	Circuit Application	Open State Volt Rating	Closed State Current Rating	Dynamic Rating, Volt-amperes
Vacuum	High Voltage	5000 V	1.0 A	100
Inert Gas	High Current	300	10.0	300
Ion Engine Switch Requirements		300	30-40 (arc supply)	0

As shown by Table B.3-II the vacuum or inert gas magnetic reed switch does not meet all the criteria of an ion engine disconnect switch. However, an important factor to consider in switching ion engine circuits is that all switching is performed at zero power. Before a switch cycle is initiated, the power conditioning voltage will automatically be reduced to zero by the ion engine control micro logic. Only after a failed engine is switched out and a standby is switched into the circuit would the power conditioning supply voltage be reapplied to the circuit. For ion engine switch applications, the Form C, single pole double throw, magnetic latching vacuum reed switch would be recommended. Voltage standoff would be no problem. Current handling capability would be increased by using a larger cross sectional area reed and contact to permit higher current ratings in the closed state. If the 30 to 40 ampere current ratings cannot be obtained with one reed switch, this rating can then be obtained by paralleling two or more reeds until the current rating desired is obtained.

A master control programmer would be used to initiate the ion engine switch action. The programmer micro logic circuitry would control the switching state of a transistor drive circuit which in turn would control the polarity of the coil pulse current. The

transistor drive circuit would operate directly from the solar bus power. An eight pole double pole reed relay would weigh approximately 0.2 lbs and would require one watt of electrical power to initiate switch action. As previously pointed out, zero power would be required to hold the contacts closed since latching magnets would be employed. On this basis, the total weight of the switch matrix system required for interconnecting eight power conditioning systems and ten ion engine systems would be 3.2 lbs.

4. Thrust Vector Displacement

In Ref. 1 the procedure for determining the optimum number of operating and standby engines on the basis of a weight-reliability criterion was presented. It was shown that for high power ion propulsion systems modularization of the thrustor system was desirable. A problem which accompanies the modularization of a thrustor system is the shift in the location of the center of thrust should engines be shut down due to a decrease in available power or should an engine fail and a standby unit be substituted. Since the accomodation of this thrust vector shift necessitates a mechanical means for moving the complete array, the required motion must be determined and minimized.

a. Optimum Standby Location

Once a thrustor array consisting of $m + n$ engines (m operating and n in standby initially) is chosen, a problem still exists in choosing the specific engines which should be operating and those which should be standbys such that the maximum thrust vector displacement necessary during the mission is minimized. To solve this problem a procedure for locating standbys in a one dimensional thrustor array was developed and then generalized to a two dimensional array.

1) Location of One Standby In A Linear Thrustor Array

Consider a linear thrustor array (Fig. B. 4-1) consisting of m engines each having equal thrust of one unit and located at the points $x_1, x_2, \ldots, x_m$. Suppose that there is one standby located at

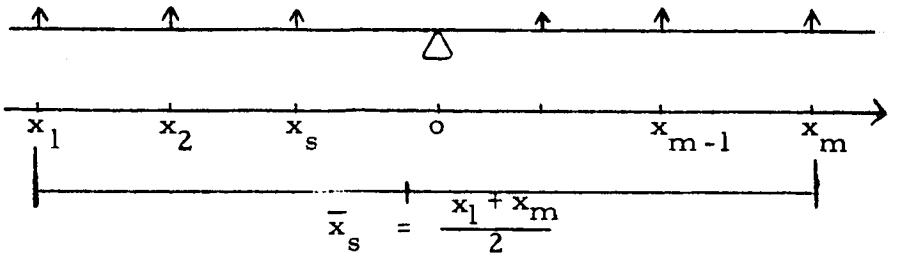

Fig. B. 4-1 Location of Standby In A Linear Thrustor Array

x_s which is to be turned on if a failure in any operating engine occurs. Assume also that the center of thrust is originally at $x = o$. This balanced torque condition is expressed by

$$x_1 + x_2 + x_3 + \ldots\ldots x_m = o \quad \text{or} \quad \sum_{i=1}^{m} x_i = o \qquad (1)$$

If the thrustor at x_j fails the resulting torque is $\sum_{i=1}^{m} (x_i) - x_j$. When the standby at x_s is turned on the array must be translated by an amount Δ_j in order to restore torque balance. The thrust vector displacement Δ_j is found from the new torque balance equation

$$\sum_{i=1}^{m} (x_i + \Delta_j) - (x_j + \Delta_j) + (x_s + \Delta_j) = o \qquad (2)$$

Solving for Δ_j yields

$$\Delta_j = \frac{x_j - x_s}{m} \qquad (3)$$

For a given x_s let $\Delta_M(x_s)$ be the maximum thrust vector displacement possible when j varies from 1 to m. We can write

$$\Delta_M = \max_{j = 1, 2, \ldots, m} \left| \frac{x_j - x_s}{m} \right| \qquad (4)$$

Physically Δ_M is equal to $\frac{1}{m}$ times the distance from the standby to the most distant operating engine. Since the most distant engine from x_s must be one of the end ones it follows that

$$\Delta_M = \max_{j = 1, m} \left| \frac{x_j - x_s}{m} \right| \qquad (5)$$

To minimize this maximum displacement $\Delta_M(x_s)$ we want to find the x_s satisfying

$$\Delta_M(x_s) = \min_{x_s} \left[\max_{j=1,m} \frac{|x_j - x_s|}{m} \right] \tag{6}$$

It can be seen that the desired x_s must be the center of a circle through the points x_1 and x_m, i.e.

$$\bar{x}_s = \frac{x_1 + x_m}{2} \tag{7}$$

Thus a single standby should be placed half way between the two outer most initially operating engines in a linear array.

2) Location of n Standbys In A Linear Thrustor Array

A placement formalism for the case of n standbys following the idea above leads to many possibilities for the optimum location of the standbys. This situation is best illustrated by the example of finding locations for <u>two</u> standbys which minimize the thrust vector displacement in a linear array. Again take a linear array of identical thrustors at $x_1, x_2, \ldots x_m$ along with two standbys s_1 and s_2 at x_{s_1} and x_{s_2} respectively, (See Fig. B. 4-2).

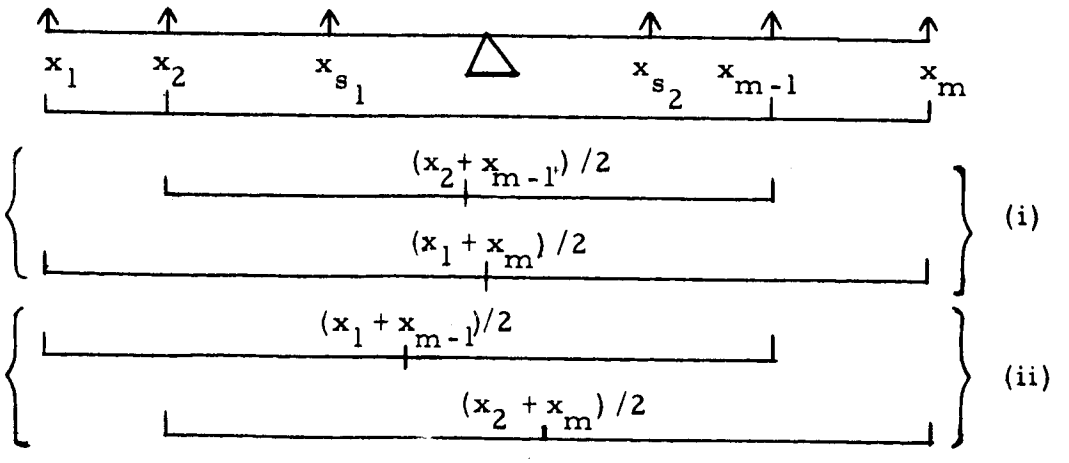

Fig. B-4-2 Locating Two Standbys In A Linear Thrustor Array

Using the midpoint criterion developed in Section 1), two apparent alternatives are to let

$$x_{s_1} = \frac{x_1 + x_m}{2} \quad , \qquad x_{s_2} = \frac{x_2 + x_{m-1}}{2} \tag{8}$$

or

$$x_{s_1} = \frac{x_1 + x_{m-1}}{2} \quad , \qquad x_{s_2} = \frac{x_2 + x_m}{2} \tag{9}$$

as shown in Fig. B. 4-2. It can be shown that the total thrust vector displacement for the worst cases (both x_1 and x_2 fail or both x_{m-1} and x_m fail) is the same for Eqs. (8) and (9). If $\Delta_{1,2}$ and $\Delta_{m-1,m}$ are these displacements, they can be shown to be given by

$$\Delta_{1,2} = -\Delta_{m-1,m} = \frac{x_1 + x_2 - (x_{m-1} + x_m)}{2m} = \Delta_o \tag{10}$$

Two questions which naturally arise are:

1. Are there any more standby locations x_{s_1}, x_{s_2} besides those given in Eqs. (8) and (9) which result in the same displacements as given in Eq. (10) ?
2. Are there any standby locations which give rise to smaller maximum displacements than $\frac{1}{2m} \left| x_1 + x_2 - (x_{m-1} + x_m) \right|$?

Both of these questions can be answered by using the following variational technique.

Let

$$x_{s_1} = \frac{x_1 + x_m}{2} + \delta_1 \quad , \qquad x_{s_2} = \frac{x_2 + x_{m-1}}{2} + \delta_2 \tag{11}$$

The corresponding displacements are then

$$\Delta_{1,2}(\delta_1, \delta_2) = \frac{x_1 + x_2 - (x_{m-1} + x_m)}{2m} - \frac{(\delta_1 + \delta_2)}{m} \qquad (12)$$

$$\Delta_{m-1,m}(\delta_1, \delta_2) = \frac{x_{m-1} + x_m - (x_1 + x_2)}{2m} - \frac{(\delta_1 + \delta_2)}{m} \qquad (13)$$

From Eq. (12) it can be seen that for $(\delta_1 + \delta_2) > o$

$$|\Delta_{1,2}(\delta_1, \delta_2)| > |\Delta_o| \qquad (14)$$

and from Eq. (13) it follows that for $(\delta_1 + \delta_2) < o$

$$|\Delta_{m-1,m}(\delta_1, \delta_2)| > |\Delta_o| \qquad (15)$$

These results imply that

1) All values of x_{s_1} and x_{s_2} such that

(a) $x_{s_1} = \frac{x_1 + x_m}{2} + \delta$, $x_{s_2} = \frac{x_{m-1} + x_2}{2} - \delta$

(b) $x_2 < x_{s_1} < x_{m-1}$ and $x_2 < x_{s_2} < x_{m-1}$

lead to maximum thrust vector displacements of Δ_o .

2) Δ_o is the smallest maximum thrust vector displacement for any standby locations.

By the same type of argument this result can be generalized to n standbys in a linear array.

3. Location of Standbys in a Two Dimensional Array

A procedure for locating standbys in a two dimensional array so that the maximum x and y components of thrust vector displacement are simultaneously minimized is illustrated by the following example. We start with eight operating engines

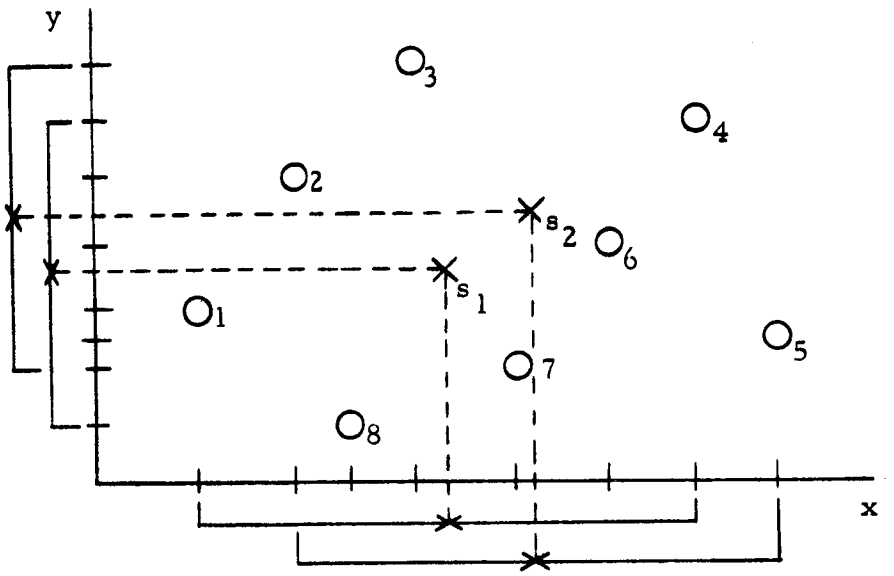

Fig. B. 4-3 Placement of Standbys In A Two Dimensional Array

and want to place two standbys s_1 and s_2 so that the maximum x and y thrust vector displacements are minimized. It is assumed that the x and y axes are given. By projecting the locations of the operating engines on each axis two linear array problems are set. These problems are solved independently by the method in the previous section (See Eq. (9)) as shown in Fig. (B. 4-3). Standby s_1 is turned on if engine 1, 4, or 8 fails and standby s_2 is turned on if engine 2, 5, 3 or 7 fail. The failure of engine 6 would not lead to a maximum thrust vector displacement.

b. Maximum Displacement

Decreasing the number of operating thrustors because of the decreasing available power from the solar cell array as well as engine failure will cause thrust vector displacement. If the power available falls to 50% (e.g., typical of the Mars mission) of its initial value only half the initially operating engines will remain operating at the end of the mission. In Fig. B.4-4 two possible configurations for the proposed ten engine array are shown. If five engines have failed and one is forced to use the remaining five, the center of thrust translates from (o, o) to (-0.8, -0.173) for Fig. B.4-4 (a) and (-0.2, 0.704) for Fig. B.4-4 (b) in the worst possible cases.

It is useful to study the motion of the center of thrust during a complete mission. Suppose that at $t = o$ there are eight operating and two standby engines in the configuration of Fig. B.4-4 (a). As the solar array power falls, the currents in the eight engines are decreased until the system reaches 7/8 of its initial power P_o. Then one engine is turned off and the remaining engines are operated at full capacities. The second engine is turned off when the power falls to $3/4\ P_o$. Using the power curve in Fig. B.4-5 the number of operating engines at any time in the mission is determined. For a successful mission the number of engines available at any point in the mission must be at least equal to the number shown in Fig. B.4-5. Table B.4-I shows the maximum thrust vector displacement for the various possible numbers of available engines in each time interval for which the mission is successful. For example, there could be six available engines during Δt_4. Assume that they are the worst possible 6, say 1, 4, 5, 8, 2, 9. Since there is a choice, we would take engine 4 as the standby and the thrust vector would move 1/2 of an engine diameter in the x direction.

From Table B.4-I, it is seen that thrust vector displacements as large as 0.8 of an engine diameter could arise during a mission. The corresponding unbalanced torque would be 0.3 ft-lbs which is 300 times the allowable value with the present attitude control capabilities. In the next section some upper bounds are obtained for the probabilities that these situations of large thrust vector displacement actually occur.

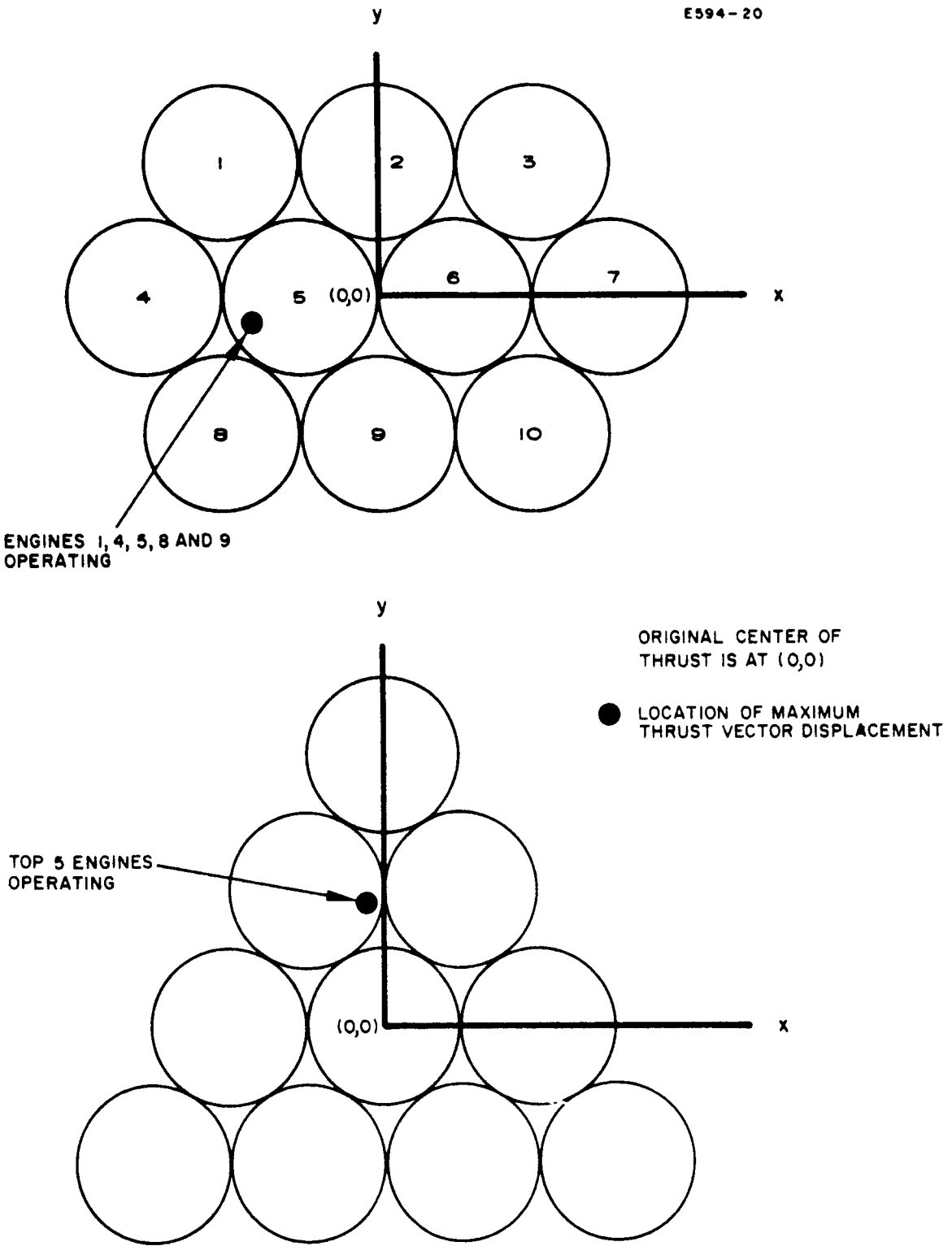

Fig. B.4-4. Thrustor configurations.

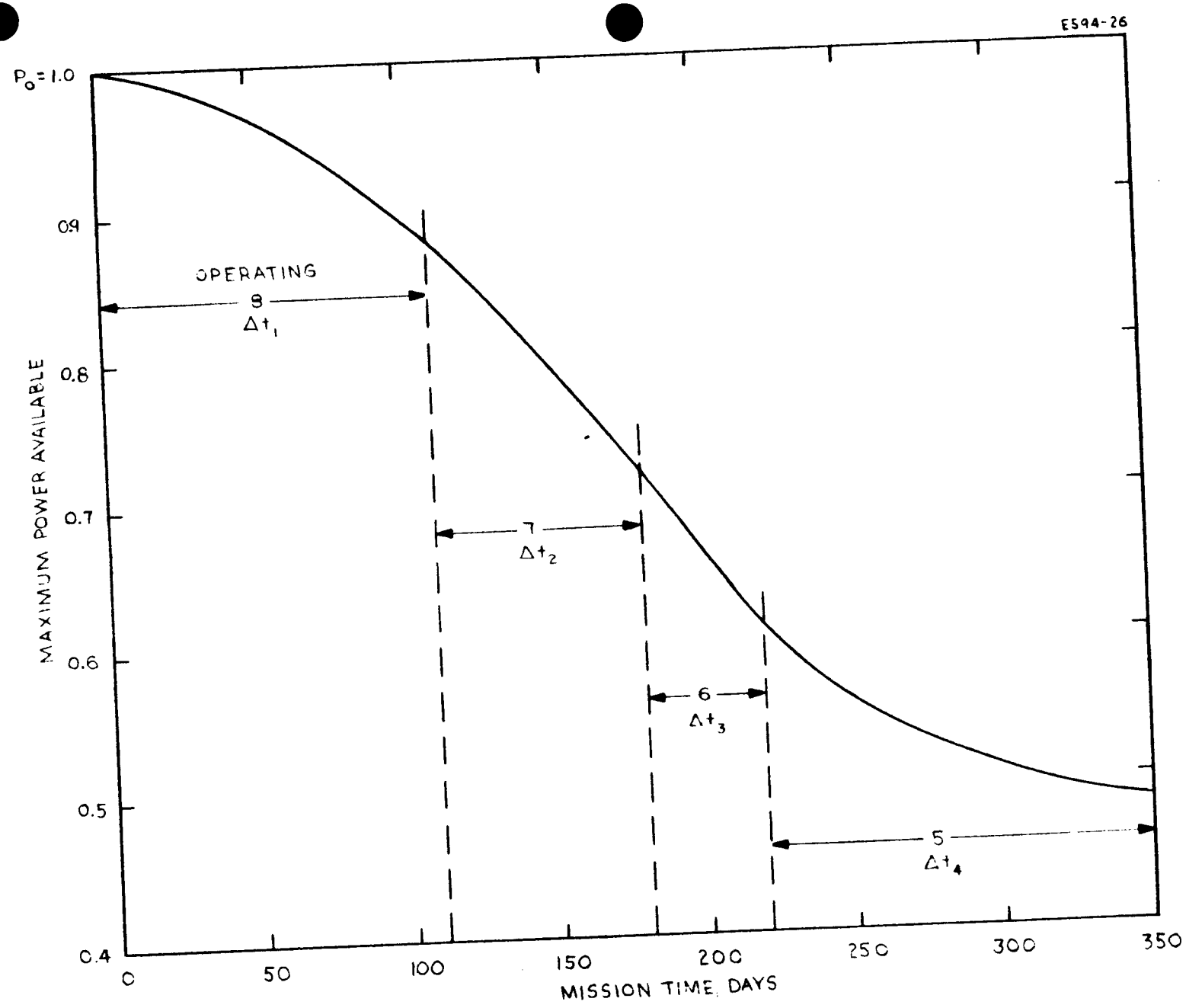

Fig. B.4-5. Maximum available power from solar cell array.

Table B. 4-I

Maximum Thrust Deflection Requirements As A Function Of Engines Required And Available During The Mission

Number of Engines Available	Thrust Deflection as Function of Number of Engines Required							
	Δt_1, 8 operating		Δt_2, 7 operating		Δt_3, 6 operating		Δt_4, 5 operating	
	Δ_x	Δ_y	Δ_x	Δ_y	Δ_x	Δ_y	Δ_x	Δ_y
5	-	-	-	-	-	-	.800	.1732
6	-	-	-	-	.667	0	.400	0
7	-	-	0.5	0	.333	0	0.100	.1732
8	0.25	.1082	.1428	.1237	0	0	0.100	0
9	0	0	.0714	0	0	0	0.100	0
10	0	0	.0714	0	0	0	0.100	0

c. Probability of Large Displacements

Referring to Fig. B. 4-4 (a), it would be useful to know the probability that only engines 1, 2, 4, 5, 8, 9 are left during Δt_4. To evaluate this probability one would have to take into account all the ways in which this event could occur. Moreover, this probability would also depend on the particular switching sequence assumed for the mission. To actually calculate these elementary probabilities and study the effect of different switching sequences on the probabilities of large thrust vector displacement situations, dynamic programing techniques must be used. This analysis has not as yet been done although preliminary study of the events leading to mission success has yielded very useful upper bounds on the elementary probabilities.

Figure B. 4-6 shows all the possible paths (90) to mission success. With eight operating and two standbys initially there can be zero, one or two failures in the first time interval and corresponding numbers of possible failures in subsequent intervals which allow mission success. The probability of a path is equal to the product of the probabilities that the appropriate number of failures occur in each time interval along that path. Since all the paths for success are considered only once, the sum of their probabilities must equal the mission reliability which is 0. 983 in this example. It is interesting to note that paths in which there are a high number of failures have small probabilities and contribute very little to the mission reliability. It will be shown that the large thrust vector displacement situations also have small probabilities.

From the flow diagram (Fig. B. 4-6) we can't determine the probability that a particular six engines will be available in Δt_4, but we can determine the probability that exactly six will be available. This is the sum of the probabilities of all the paths in which a total of four failures occur. These paths are indicated by an asterisk in Fig. B. 4-6. Based on this method the curves in Fig. B. 4-7 have been determined.

From the data in Table B. 4-I of number of engines available vs. thrust vector displacement and the curves of Fig. B. 4-7 which show upper bounds to the probability of having a certain number available, the curves in Fig. B. 4-8 have been made. These curves give bounds to the probabilities that the largest possible thrust vector displacement will occur in each interval. In Fig. B. 4-9 the upper envelope of the four curves of Fig. B. 4-8 has been plotted. Its main signifigance is to show that a useful trade-off can be made of maximum thrust vector displacement and mission reliability. For example, the system can be designed for a maximum thrust vector displacement of only 0. 5 of an engine diameter if the mission reliability is derated by 0. 014.

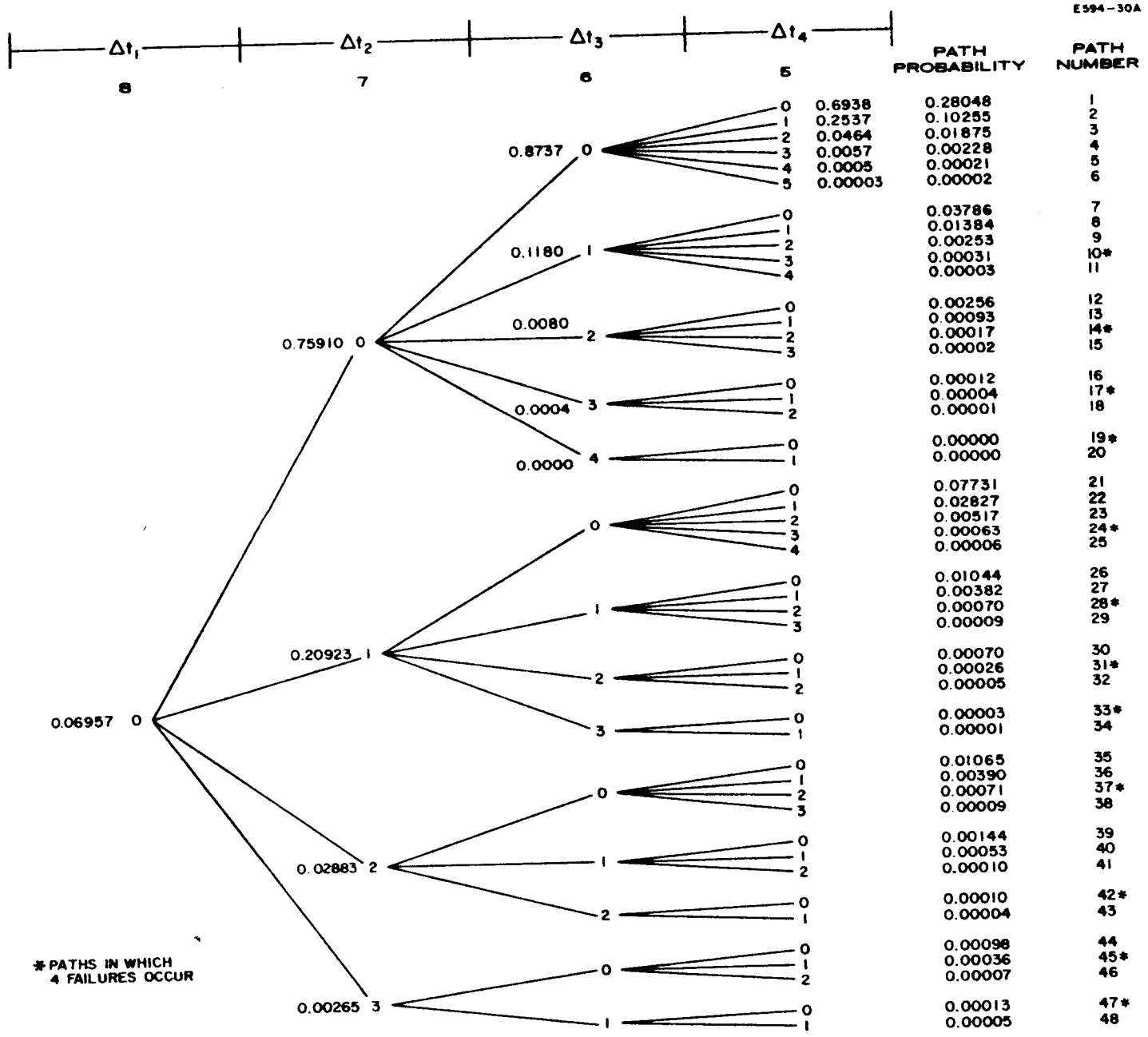

FIGURE B.4-6(a) Detailed Mission Reliability Chart

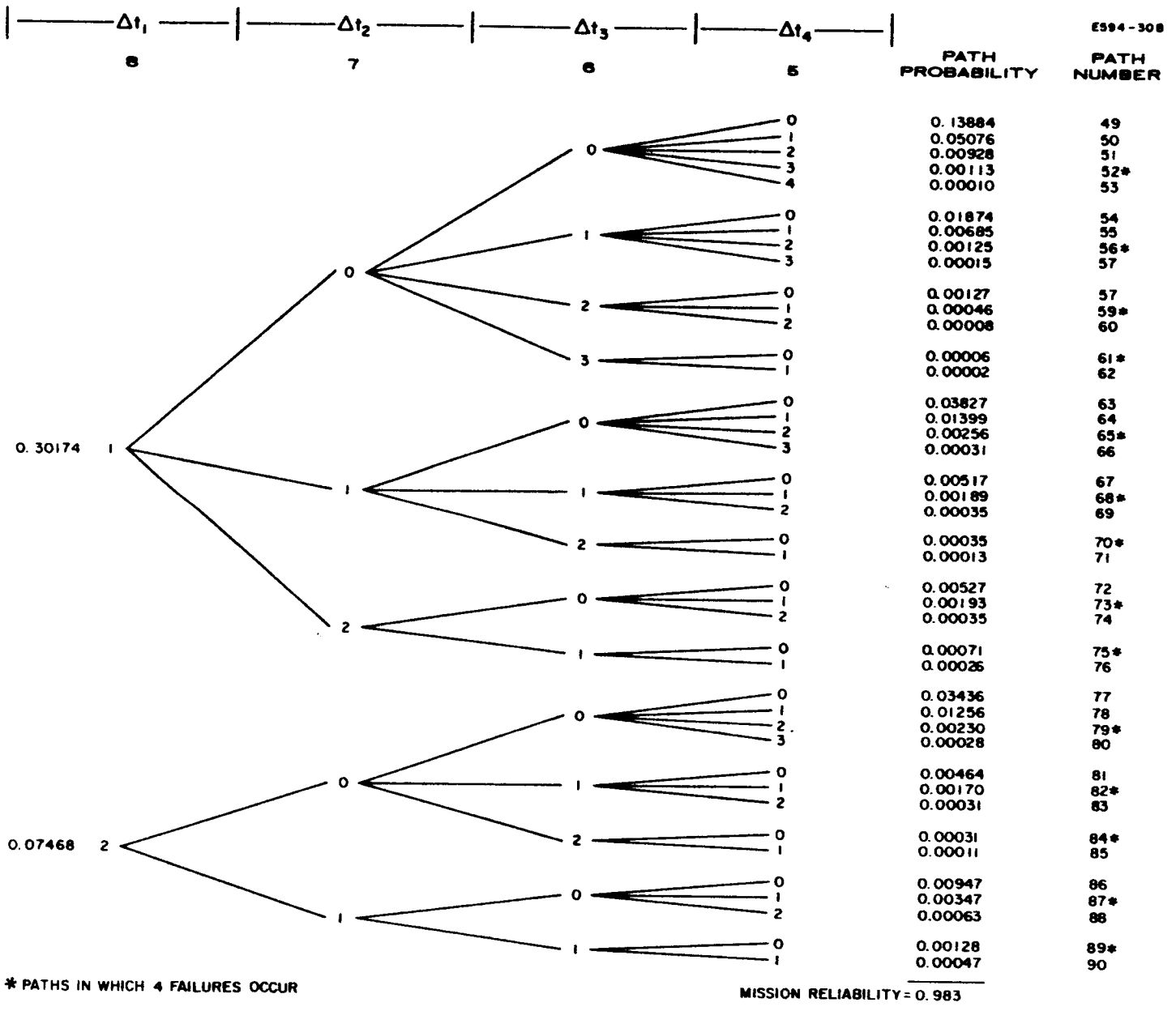

FIGURE B.4-6(b) Detailed Mission Reliability Chart
(continued)

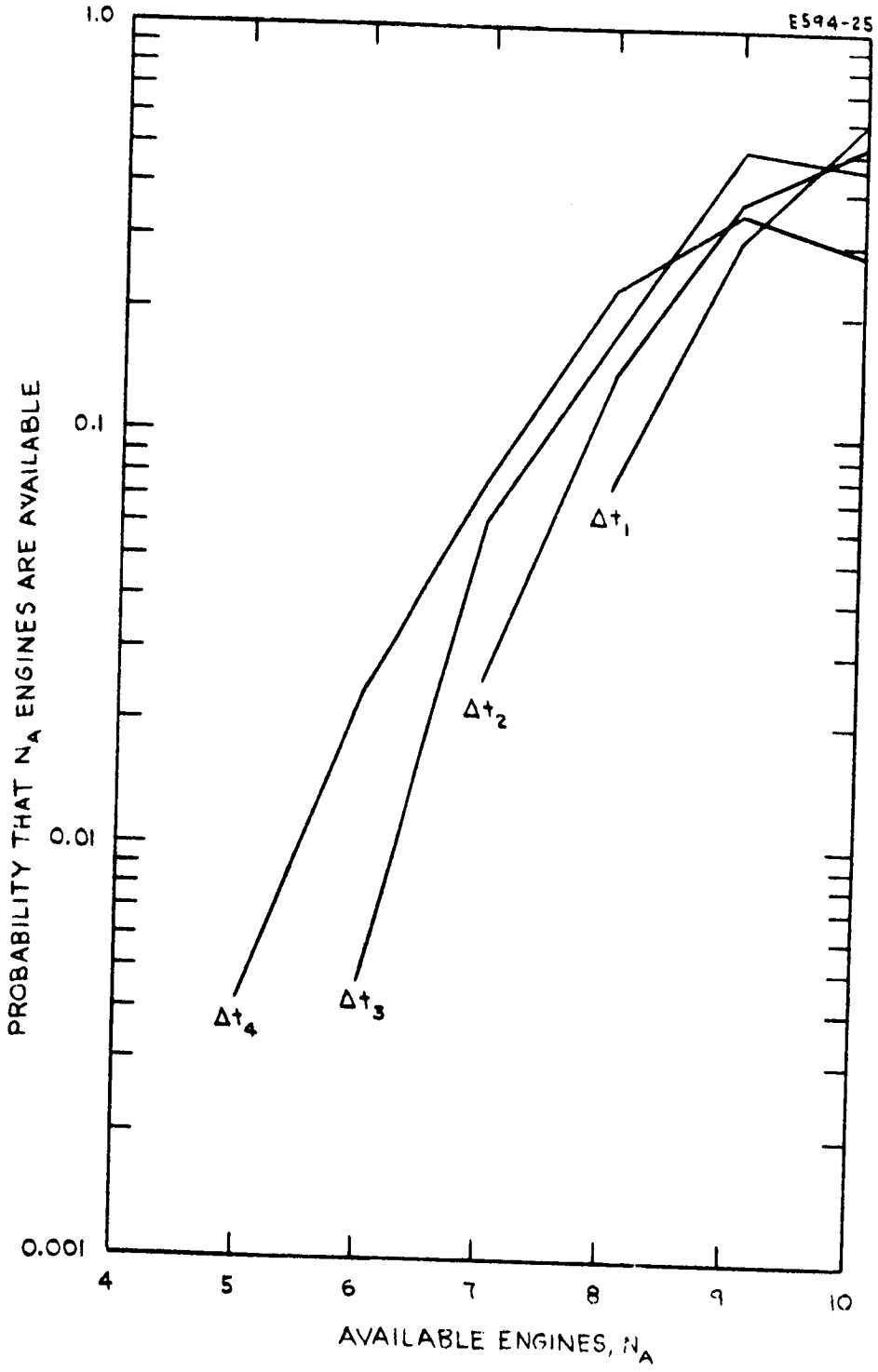

Fig. B.4-7. Probability of N_A engines being available during the mission.

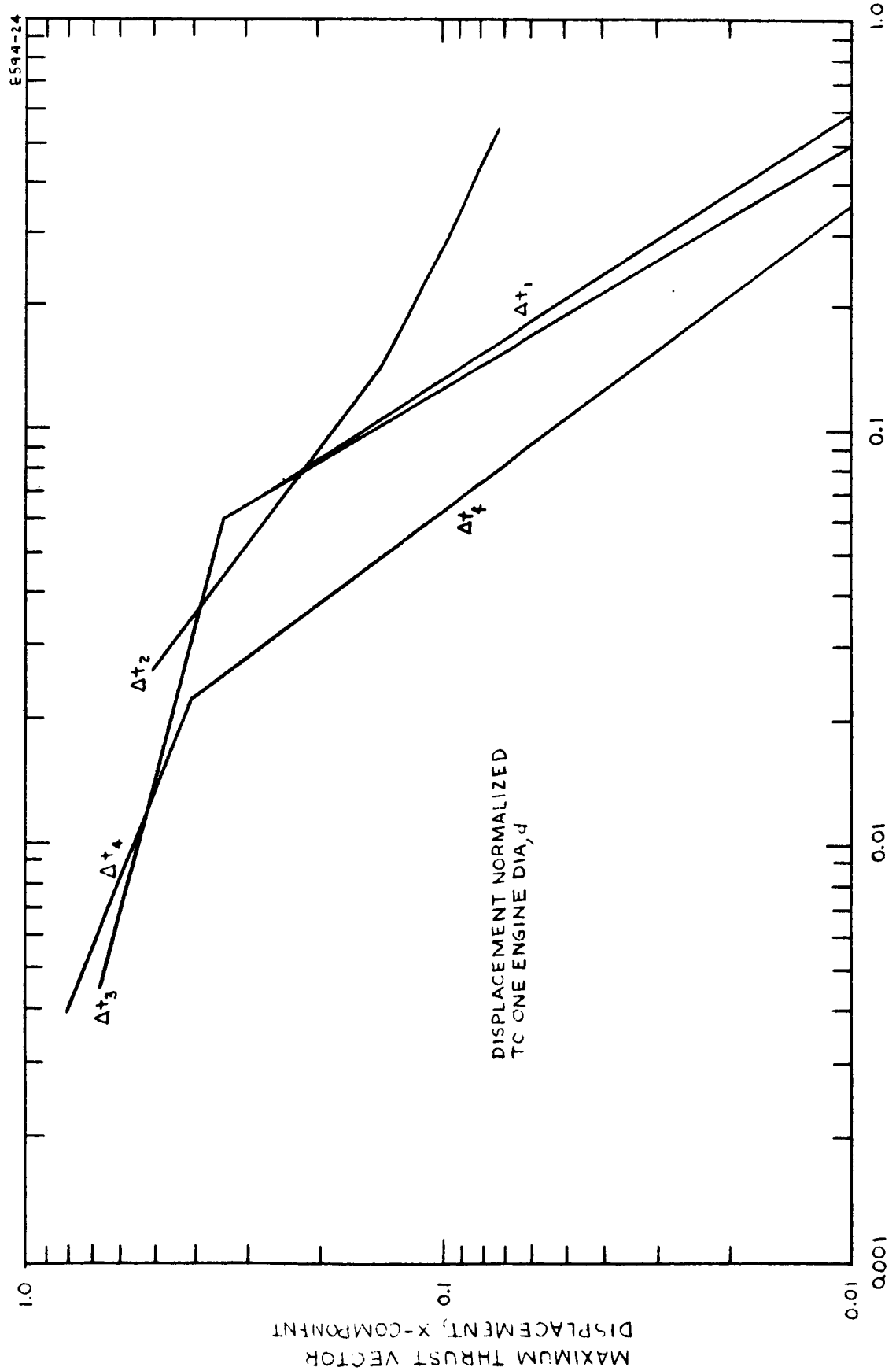

Fig. B.4-8. Thrust vector displacement probability.

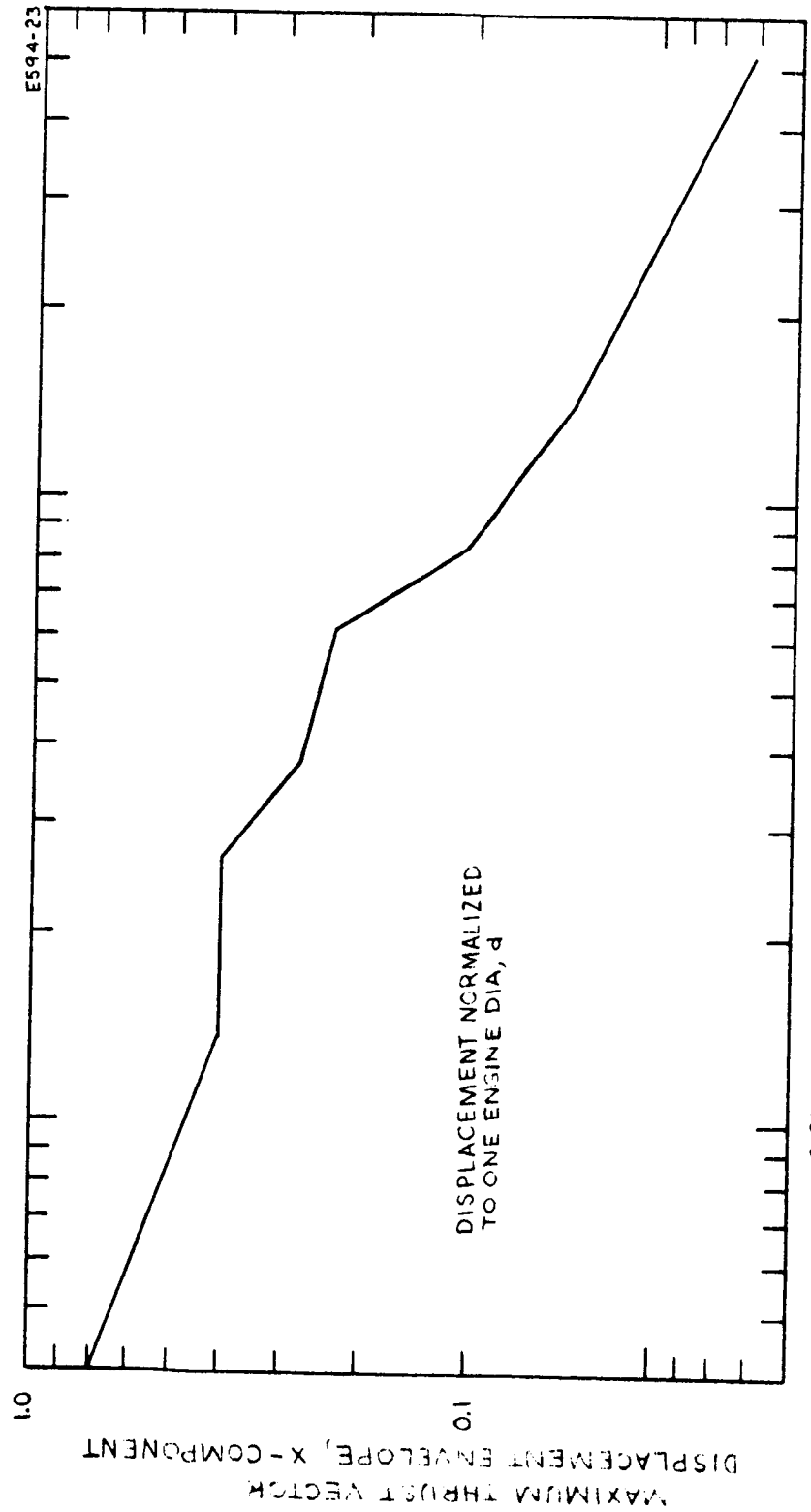

Fig. B.4-9. Maximum thrust vector displacement probabilities.

5. Design Verification Hardware

Outstanding progress has been made to date on the thrustor, feed system and power conditioning and controls to be used during the breadboard testing of the power conditioning and control system. The testing of the power conditioning and control system with a thrustor is planned for early next month.

a. Power Conditioning and Controls

The fabrication effort has produced 19 of the required 25 modules for the breadboard system. These units consist of 13 Main Drive modules (Fig. B.5-1), three Accelerator modules (Fig. B.5-2), and three Arc modules (Fig. B.5-3). The Main Drive and Accelerator modules have been fully tested and are now qualified for use in the system. The Arc modules have just finished fabrication and are awaiting test.

Design, breadboarding, and breadboard testing have been completed on the Cathode Heater module (two required) and the Master Oscillator module (one required). The required magnetic components for all system modules have been fabricated and tested. The module fabrication of the Master Oscillator has been initiated and the fabrication of the Cathode Heater modules will begin upon completion of the mechanical design.

The three modules for the Magnet, Evaporator Heater, and Neutralizer Heater supplies are awaiting definition prior to expending any real effort on them.

The system logic and control functions are packaged on three circuit cards (Fig. B.5-4). These circuits have been fabricated and tested. The control box containing the necessary switches and adjustments has been fabricated along with the system cable which provides the required interconnections between prime power, control box, logic and control circuitry, and power modules.

Testing has begun on the complete Main Drive supply (Fig. B.5-5). This effort is the first real test of the incrementally regulating, d.c. adding system and the results obtained to date are very encouraging. The following important milestones have been accomplished:

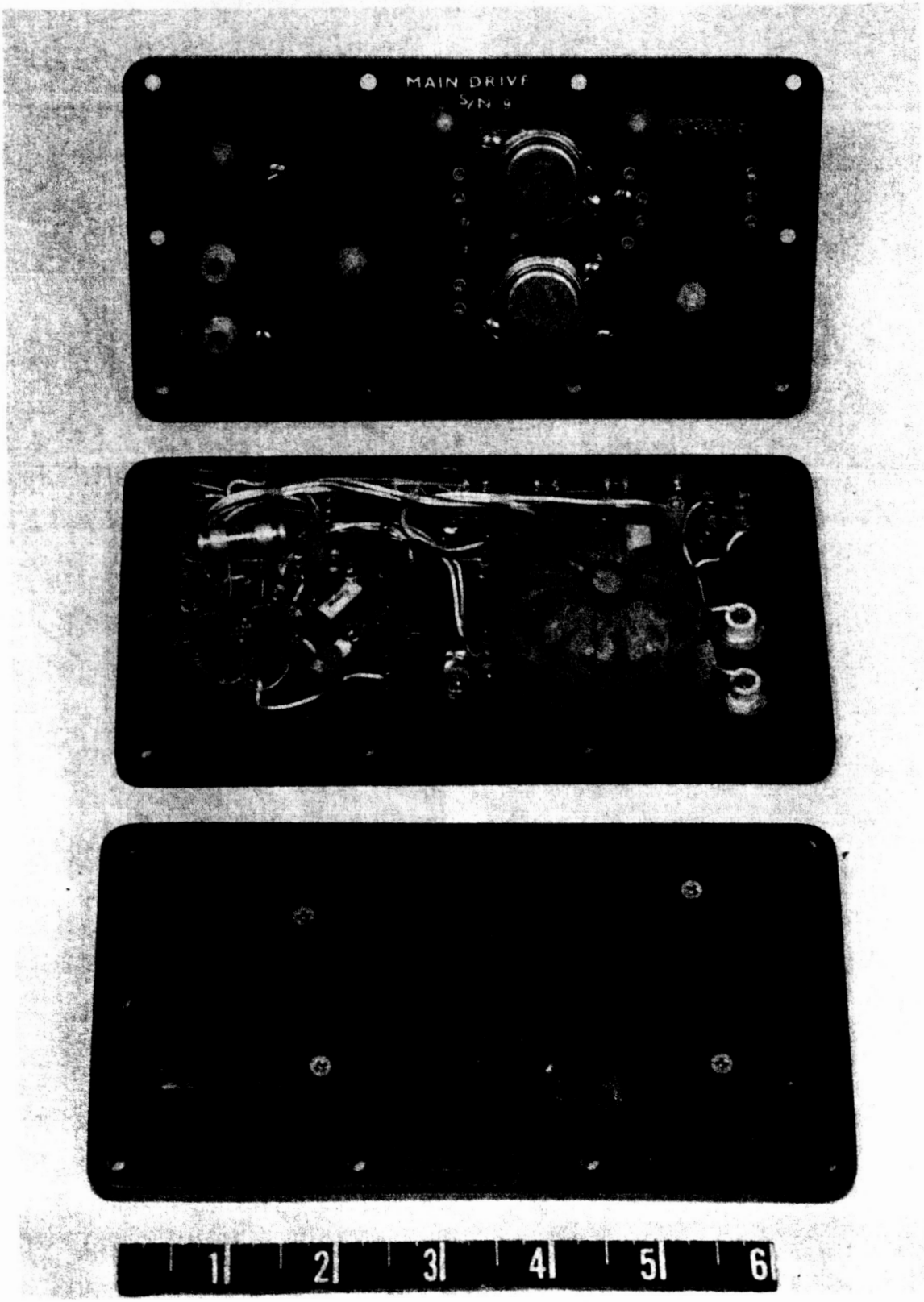

Figure B.5-1 Main Drive Supply Modules

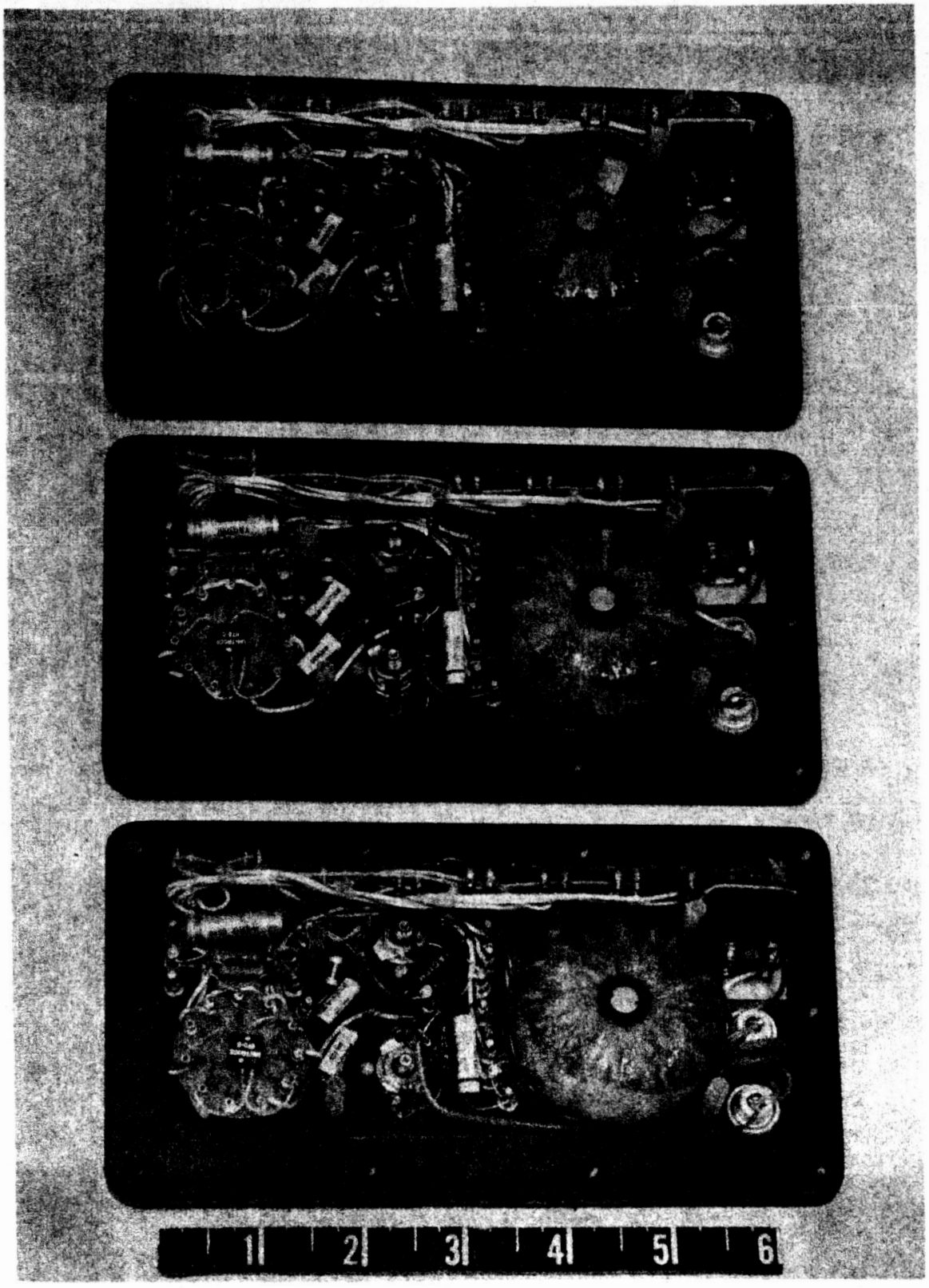

Figure B.5-2 Accelerator Supply Modules

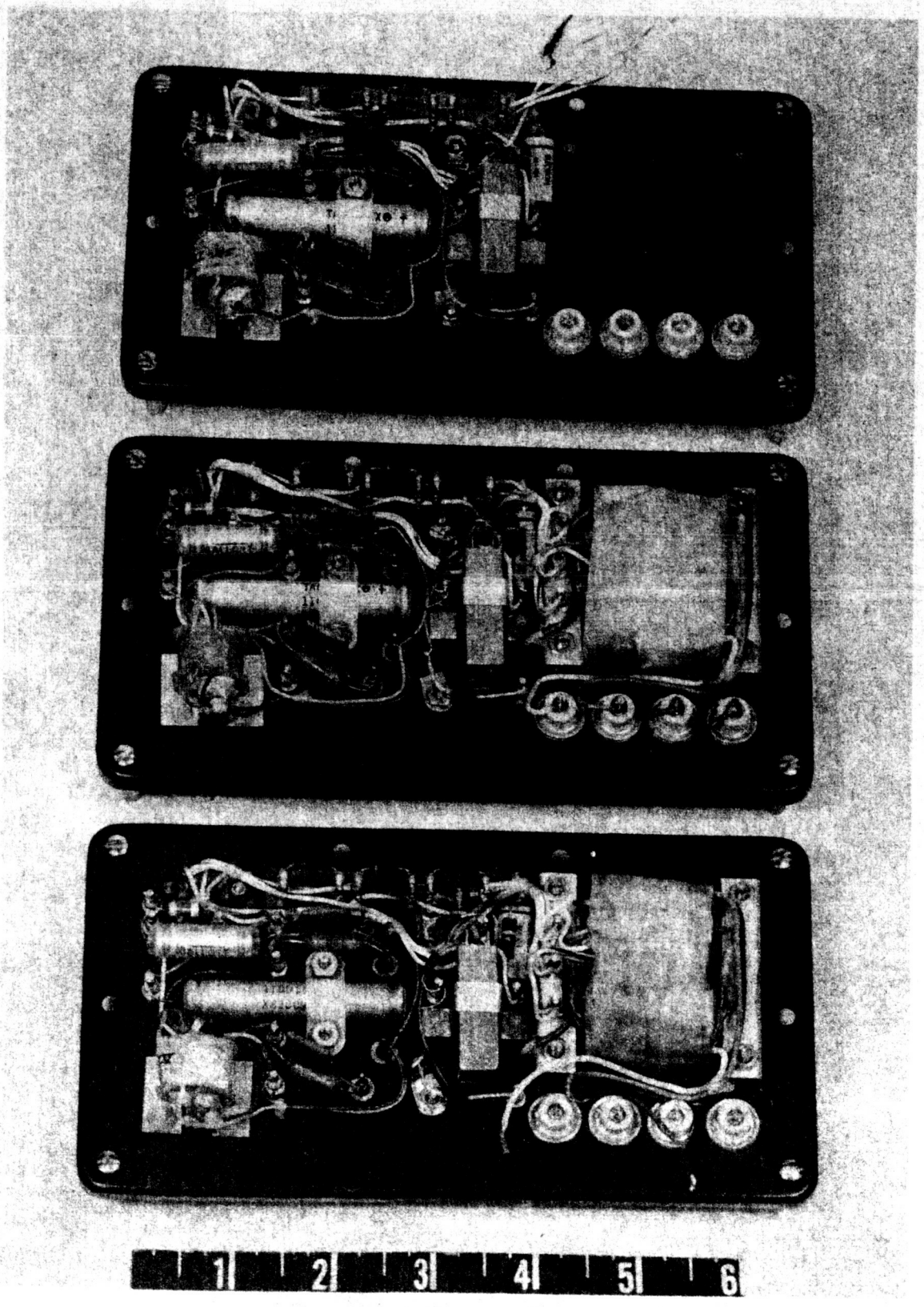

Figure B.5-3 Arc Supply Modules

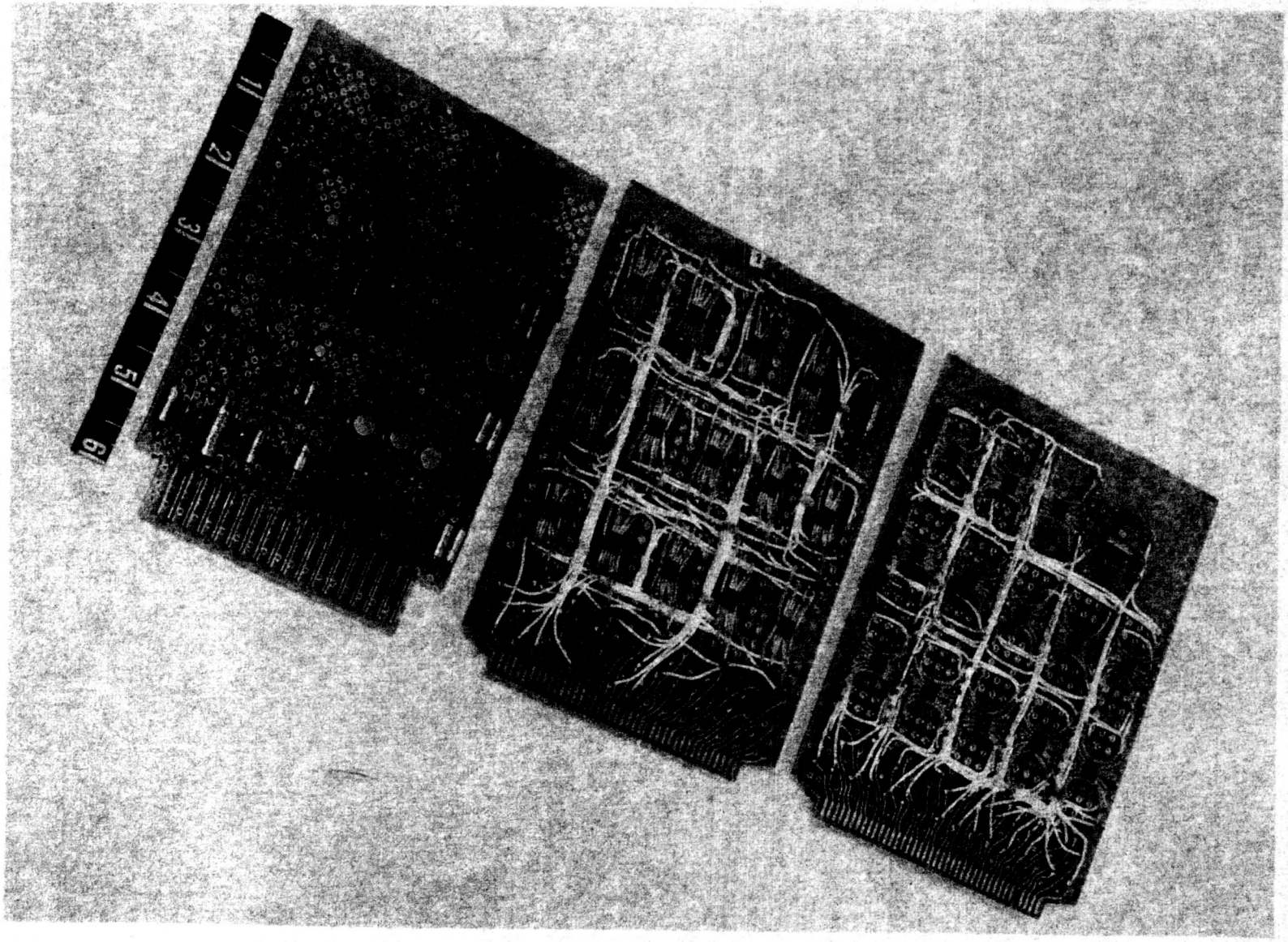

Figure B.5-4 System Logic and Control Circuit Boards

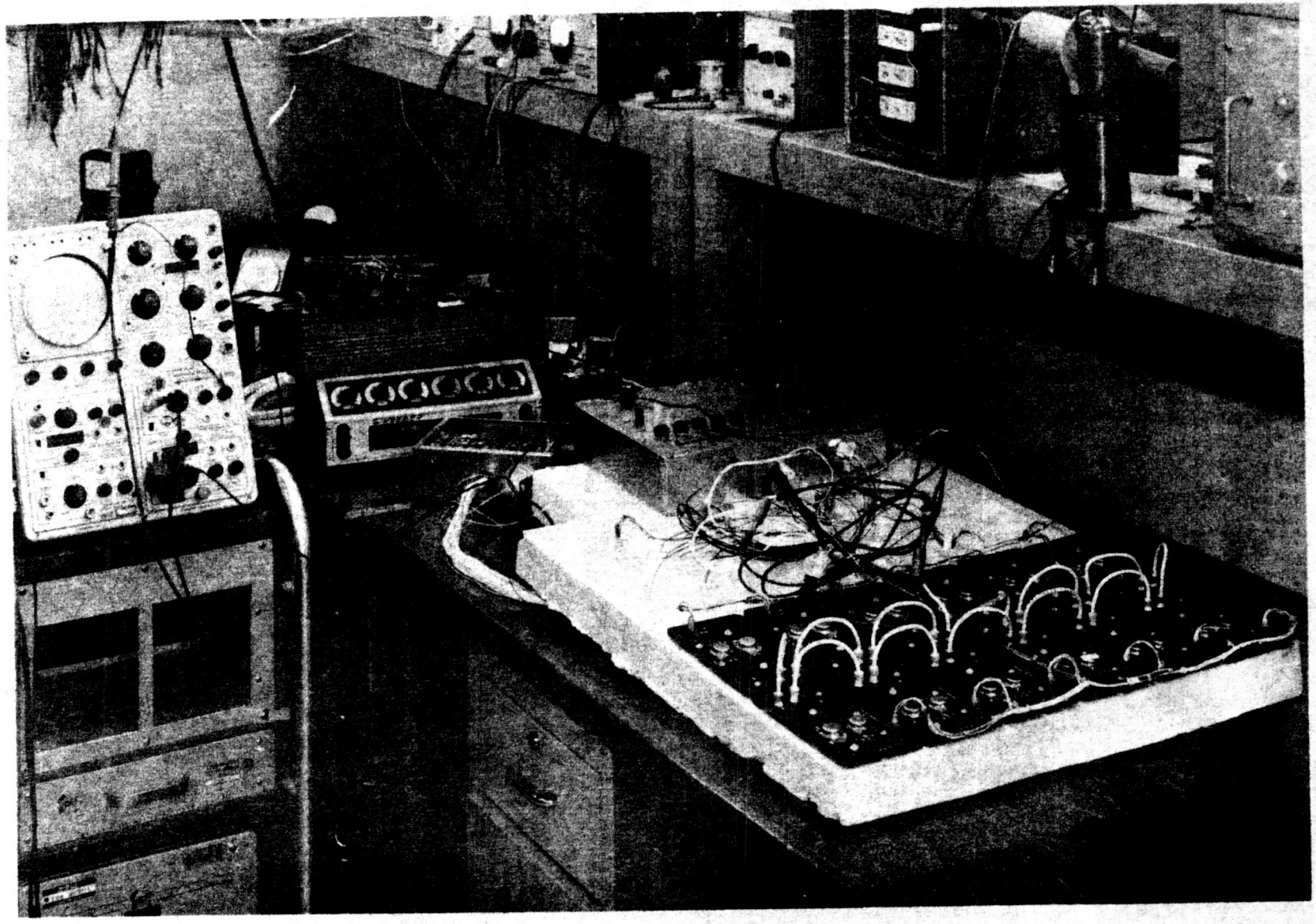

Figure B.5-5 Test Setup for Testing Main Drive Supply

A. Basic checkout and troubleshooting

B. Demonstration of incremental line regulation

C. Demonstration of correcting for a failed module

D. Measurement of unfiltered output ripple

The output ripple measurement has indicated that a completely unfiltered output may not provide satisfactory performance. Performance is very good at light loads but deteriorates to about plus zero, minus 20% under heavy load and has the form of very fast, narrow spikes of the above magnitude. It is thought that a small amount of capacitance across the total output will be sufficient to reduce the ripple to less than 5%. This problem is under investigation at present and is not considered to be serious.

The tests for arcing and overload protection are scheduled as the final step prior to qualifying the complete Main Drive supply. These tests will be performed following the installation of the changes required by the output ripple investigation.

The successful operation of the closed loop incremental regulator has been a major milestone in that virtually all of the concepts of the multi-module approach to power conditioning have been demonstrated. One concept that was not demonstrated by the Main Drive supply testing was that of a.c. adding. The a.c. adding concept has been demonstrated using two breadboard Arc modules. It was shown that the driven modules may be a.c. added and then rectified with only a small amount of filtering required. This shows that there is no appreciable phase shift between modules. It was further demonstrated that a series module may be turned off by shorting out the transformer primary and that the difference between the reflected short circuit at the secondary and an actual short circuit at the secondary is negligible. The relay shorting circuit was successfully life tested for 100,000 operations without a failure. Since a mission would require probably 100 operations at most, confidence in this approach is quite high.

b. Thrustor

1) Life Testing

The life test of the liquid-mercury cathode in a 20 cm electromagnetic thrustor has now passed the 1200 hour mark. The cathode and thrustor were removed after 1150 hours from the vacuum station and examined for mechanical deformation. No cathode erosion could be observed leading to the prediction of practically unlimited cathode life. Maximum erosion of the accelerator electrode was 0.006" which occurred between the apertures on the downstream side of the electrode. Extrapolating from this data, the predicted electrode life is of the order of 10,000 hours. The 750-hour average life test point is

$$I_B = 584 \text{ mA}$$
$$V_B = 6.2 \text{ kV}$$
$$I_K = 13.5 \text{ A}$$
$$V_D = 31.25 \text{ V}$$
$$\text{eV/ion} \quad 722$$
$$\eta_{mass} = 81.7\%$$
$$\eta_{pwr} = 89.0\%$$
$$\eta_{total} = 72.5\%$$

This test has been restarted and will be continued at least to the 1750-hour point under present funding. No deterioration of thrustor performance was observed to date. It is anticipated that the life limiting item will be the accelerator electrode. Further improvements in perveance matching the optical structure to the plasma density distribution will reduce this erosion and increase electrode lifetime.

2) Thrustor Efficiency

The life test point does not represent the utmost in overall thrustor performance. (This test is performed without any control circuits and the operating point fluctuates slightly due to

changes in line voltage and room temperature.) During the course of this test, several 5-hour points have been recorded with source energy per ion of approximately 600 eV/ion. (See Table B.5-I)

TABLE B.5-I

Average Engine Parameters During Three 5-Hour Periods

Engine Parameter	Average Values During Three 5-Hour Periods		
I_B, mA	604	599	619
V_B, kV	6.2	6.2	6.2
I_K, A	12.3	12.2	12.6
V_D, V	30.1	30.0	29.0
eV/ion	613	606	590
η_{mass}, %	84.6	83.4	79.4
η_{pwr}, %	91.0	91.0	91.5
$\eta_{tot.}$, %	77.0	75.7	72.5

Experiments are continuing to establish that combination of cathode geometry, magnetic field shape, baffle size and location and discharge chamber parameters which will give the best overall thrustor efficiency.

3) Permanent Magnet Thrustor

A permanent magnet thrustor has been successfully operated. To date, the source energy per ion has been approximately 100 eV/ion greater than the electromagnetic design, however, some differences still exist between the two magnetic field shapes, particularly at the cathode position. Mechanical modifications are underway to duplicate the electromagnetic field exactly.

4) Automatic Igniter

A solenoid-operated igniter for liquid-mercury cathodes has been constructed and tested. Two different circuits were used to demonstrate the electrical flexibility of this igniting method. The discharge was started immediately by this igniter every time the discharge voltage was turned on.

c. Feed System

A new feed system concept has been evolved. This system consists of two units; a reservoir consisting of a welded bellows or rolling diaphragm from which the mercury may be expelled by a mechanical force exerted on one end and a pressurizer consisting of another welded steel bellows surrounded by a vapor tight jacket. The region between the bellows and jacket contains a small quantity of liquid (i.e., H_2O) in equilibrium with its vapor. By heating this unit, the vapor pressure is increased and a force exerted which compresses the bellows (see Fig. B.5-6).

This force is mechanically transmitted to the reservoir and the mercury is expelled. The fundamental advantage of this design over similar systems is that the pressurizer and reservoir may be thermally isolated so that the mercury pressure is independent of the temperature of the mercury reservoir. The mercury pressure depends only on the temperature of the pressurizer which may be rapidly changed due to the small mass of the pressurizer components.

A prototype pressurizer has been built and found to operate satisfactorily in conjunction with a standard piston-type feed system. Design of a complete system (Fig. B.5-6) is underway and mechanical assembly should be complete within two to three weeks. An electrical circuit has been designed to couple the pressurizer temperature (hence the propellant flow) to the beam current. The principle is similar to that used successfully to stabilize the mercury vapor flow rate to the discharge chamber of the oxide cathode thrustor.

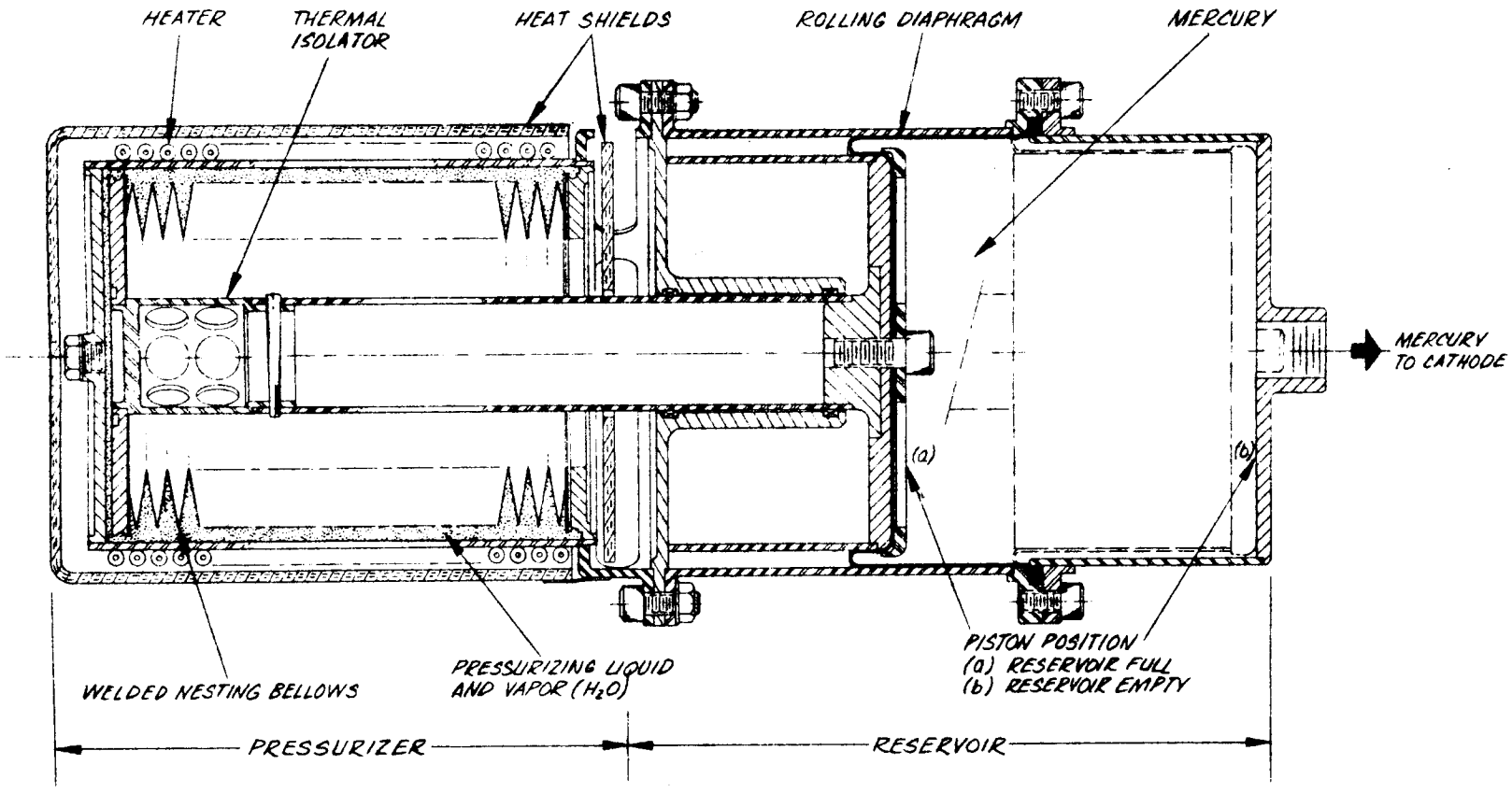

Fig. B.5-6. Vapor pressurized liquid mercury feed system.

C. SPACECRAFT SYSTEM DESIGN

All configurations presented herein are designed to be compatible with the original spacecraft envelope specifications (See HAC Bi-Monthly No. 2). Present efforts on the Saturn IB/Centaur version of the spacecraft are involved with the extension of the spacecraft bus to a 100 inch square cross section in lieu of the 100 inch cylindrical envelope. This decision has been cleared by JPL and is acceptable with the solar array contractor. Results of this change in spacecraft envelope design constraint plus details of the spacecraft design are being resolved and will be presented in the final report.

C.1 General Arrangement

The proposed general arrangement for the Saturn IB/Centaur Solar Electric Propulsion Spacecraft is shown in Figures C.1-1 and C.1-2. The major subsystems considered in the arrangement are as follows:

a. Lander Capsule (1000 lb "Discoverer" type
b. Ion Engine System (Thrustors, propellant reservoirs and Feed System)
c. Solar Cell Array (Boeing folding modular type with rectangular panels hinged at spacecraft base)
d. Power conditioning system
e. Retro Rocket System (liquid system)
f. Attitude Control N_2 gas tankage
g. Communication Antenna and Electronics
h. Mars Scanner platform and instruments

Other sub-systems such as low gain antenna, canopus tracker and miscellaneous electronic equipment were not included for the basic spacecraft configuration study since their weights and volumes are relatively insignificant in comparison to the major sub-systems noted above.

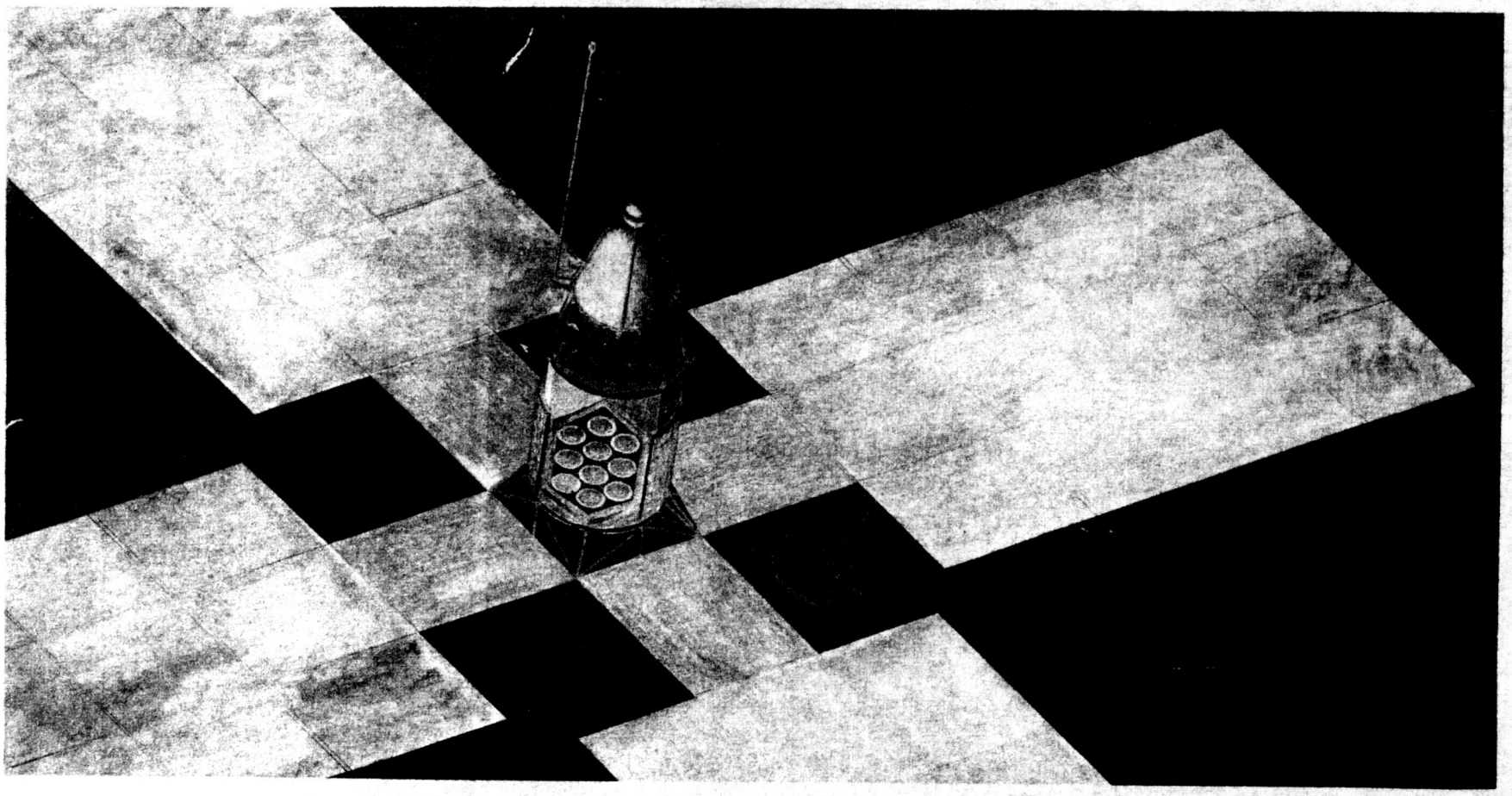

Figure C.1-1 Electric Propulsion Spacecraft
Saturn IB/Centaur Booster

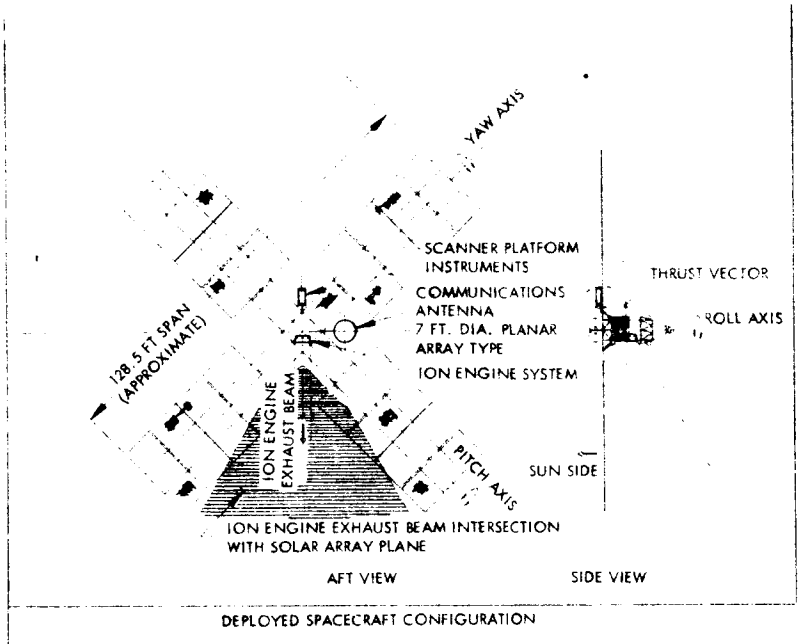

DEPLOYED SPACECRAFT CONFIGURATION

POWER CONDITIONING MOD
NOTE:
PREFERRED CONFIGURATION
OF 8 PANELS (2 EACH ON 4 F

67.0
OPEN
ION

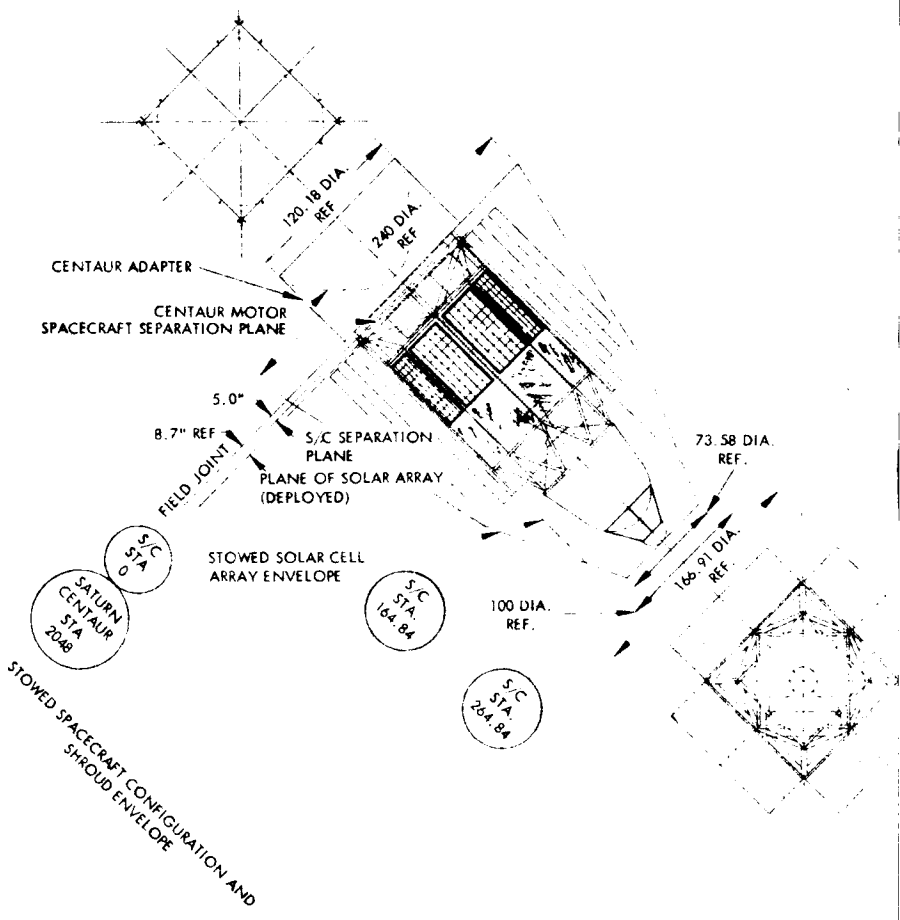

Figure C.1-2 Electric Propulsion Spacecraft

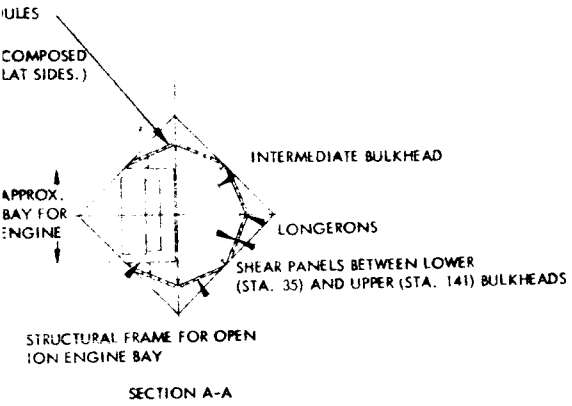

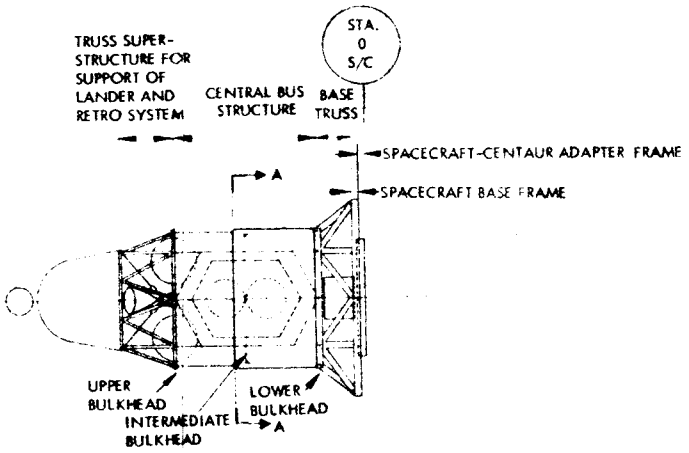

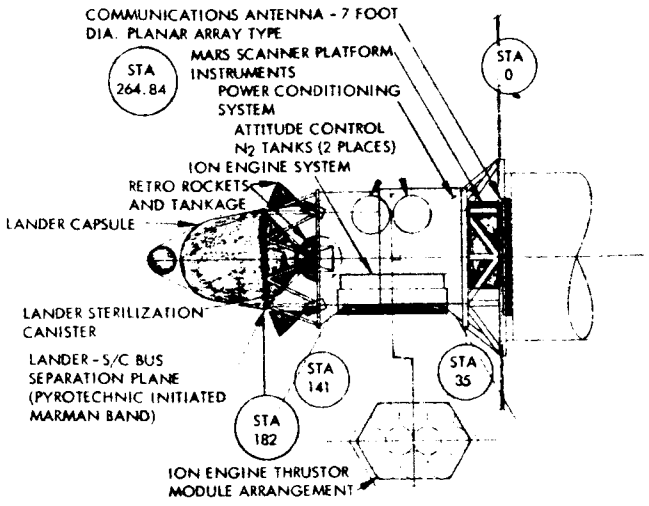

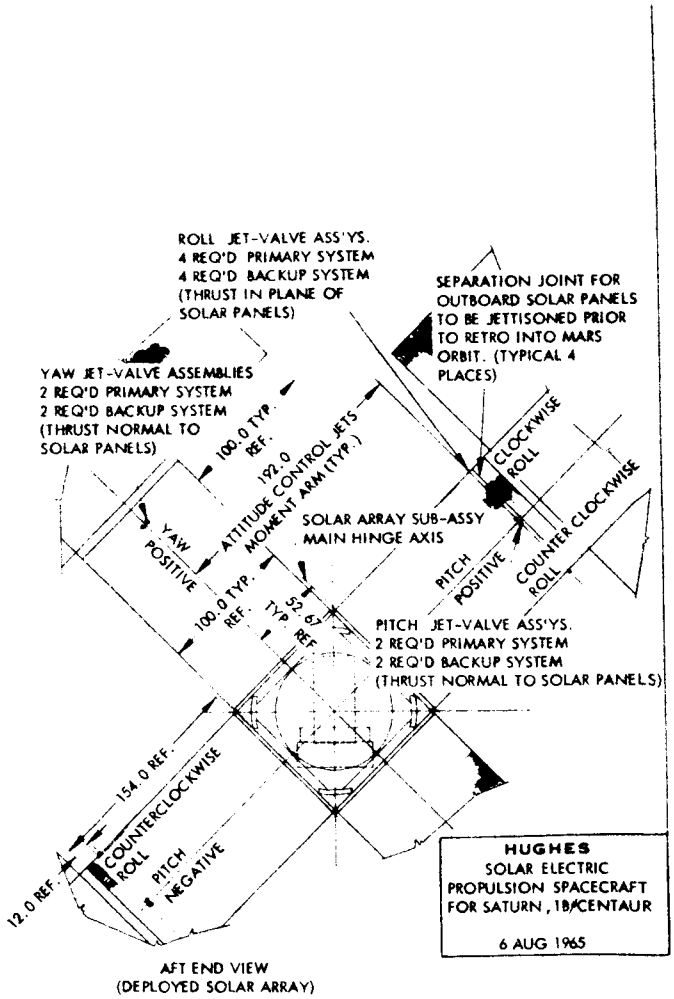

AFT END VIEW
(DEPLOYED SOLAR ARRAY)

The arrangement presented was arrived at by a number of iterations governed by envelope constraints, center of gravity constraints, stowed and deployed solar cell array configuration and envelope considerations, sub-system requirements and over all spacecraft structural considerations.

The spacecraft is attached to the Centaur forward adapter by a square base frame adapter at station zero. Station zero is designated as the field joint between the spacecraft and launch vehicle. Forward of the base frame (at approximately station 5) is located the spacecraft launch vehicle separation plane. The base of the spacecraft is also a square frame which serves as the mounting structure for the four solar array fold-out panel assemblies. The 100 inch square spacecraft base makes a transition to the octagon shaped central bus structure utilizing an open truss structure. The seven (7) foot diameter planer array antenna and the Mars scanner platform are stowed within the open base truss frame, and they may be deployed readily through the base after spacecraft separation.

The central bus structure is essentially an octagon cross section contained with the 100 inch diameter spacecraft cylindrical envelope constraint. Longerons and structural panels enclose the central portion of the bus with the exception of one quadrant left void of structure, but reinforced around its perifery, to permit passage of the ion engine thrustor array and exhaust beam. The octagon shear panels also serve to mount eight (8) power conditiong modular panels, thereby maintaining proximity with the solar arry. Within the bus is mounted the attitude control gas tanks and electronic components. A large volume is available within the bus for additional sub-systems.

A lightweight open truss to support the lander capsule extends forward of the central bus. Dual retro rockets and associated tankage are mounted within the lander support truss. The retro rockets are oriented to fire forward after lander capsule-spacecraft separation.

The overall spacecraft (including the lander capsule) extends 265 inches forward of station zero and does not violate the 100 inch cylindrical envelope allotted for the stowed configuration. The placement of the lander capsule at the forward end of the spacecraft is desirable and has least affect on spacecraft configuration should a different lander configuration be selected by JPL.

A preliminary weight breakdown applicable to the foregoing configuration is presented in Tabel C.1-I.

TABLE C.1-I

Solar-Electric Propelled Saturn IB/Centaur Mars Orbiter Spacecraft Weight Breakdown

	Wt.	lbs.
PAYLOAD		1525
o Orbiter	475	
o Lander	1000	
o Data Automation System	50	
TELECOMMUNICATIONS		200
GUIDANCE & CONTROL		525
ELECTRIC PROPULSION SYSTEM		4919
o Solar Array	2720	
o Power Conditioning	280	
o Thrusters(including Controls)	235	
o Propellant & Tankage	1684	
RETRO-ROCKET		1021
STRUCTURE		1600
AUXILIARY POWER		60
ELECTRIC HARNESS		250
SPACECRAFT-CENTARU ADAPTER		800
		10,900

Figures C. 1-3 and C. 1-4 illustrate the general arrangement of an Atlas-Centaur booster spacecraft designed to meet the requirement of forward mounted solar cell panels.

The proposed structure is an assembly of light alloy tubular weldments and is fully turssed at each bay with the exception of open frames around the electric engine cluster and the scanner package. Fabricated light alloy frames are provided in these areas.

All components are positioned in the vehicle within the space limits defined in Bi-Monthly Report Number 2, Figure D. 2.1-1, and are arranged to ensure minimum displacement of the spacecraft CG from the boost vehicle center-line while in the stowed configuration. Component location is also influenced by the desirability of positioning the CG of the spacecraft in the transit configuration as far aft as possible from the solar panel plane in order to minimize the impingement of the ion beam on the solar cell panels.

The solar cell panels are attached by hinged brackets and deployment actuators to the forward truss frame. The power conditioning panels are mounted circumferentially around the forward truss section adjacent to the solar panel attachment brackets.

The electric engine cluster is caged to the box frame during boost and is provided with two axis translatory motion and 30° rearward thrust line rotation while in operation. An ejection devise is provided to jettison the complete engine cluster and fuel system prior to retro-fire.

The scanner platform is caged to the box frame during boost. It is extended aft on a rotating mast prior to the electric engine start-up. This serves the duel purpose of repositioning the deployed vehicle CG on the electric engine thrust line and provides the scanner with an unobstructed hemispherical field view. The scanner platfrom is retracted and re-caged during retro-fire.

The retro-motor, propellant tanks, attitude control nitrogen tank, together with spacecraft instrumentation and communication electronics are mounted in the aft thrust bay. The C. G. shift during the transit phase

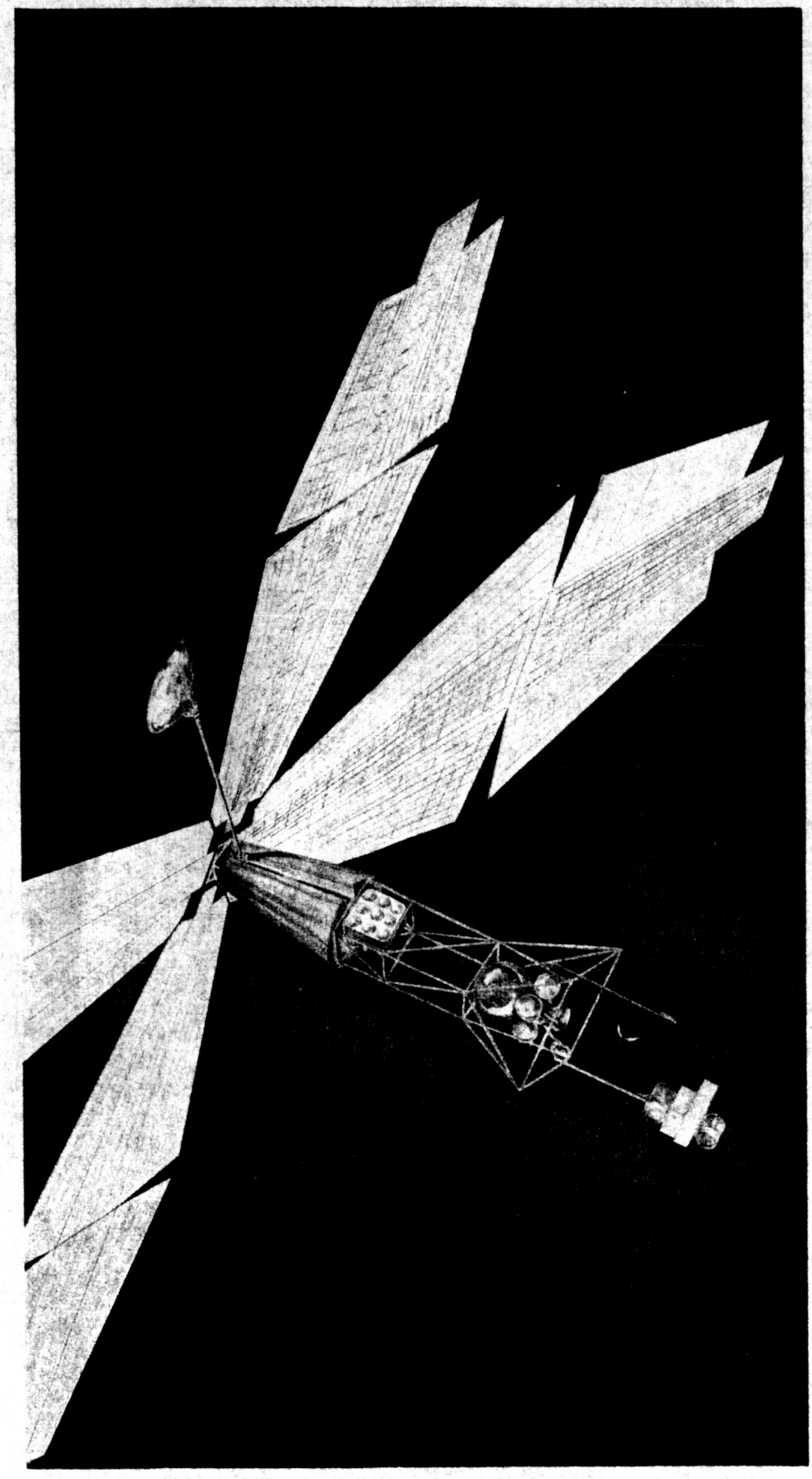

Figure C.1-3 Electric Propulsion Spacecraft
Atlas-Centaur Booster

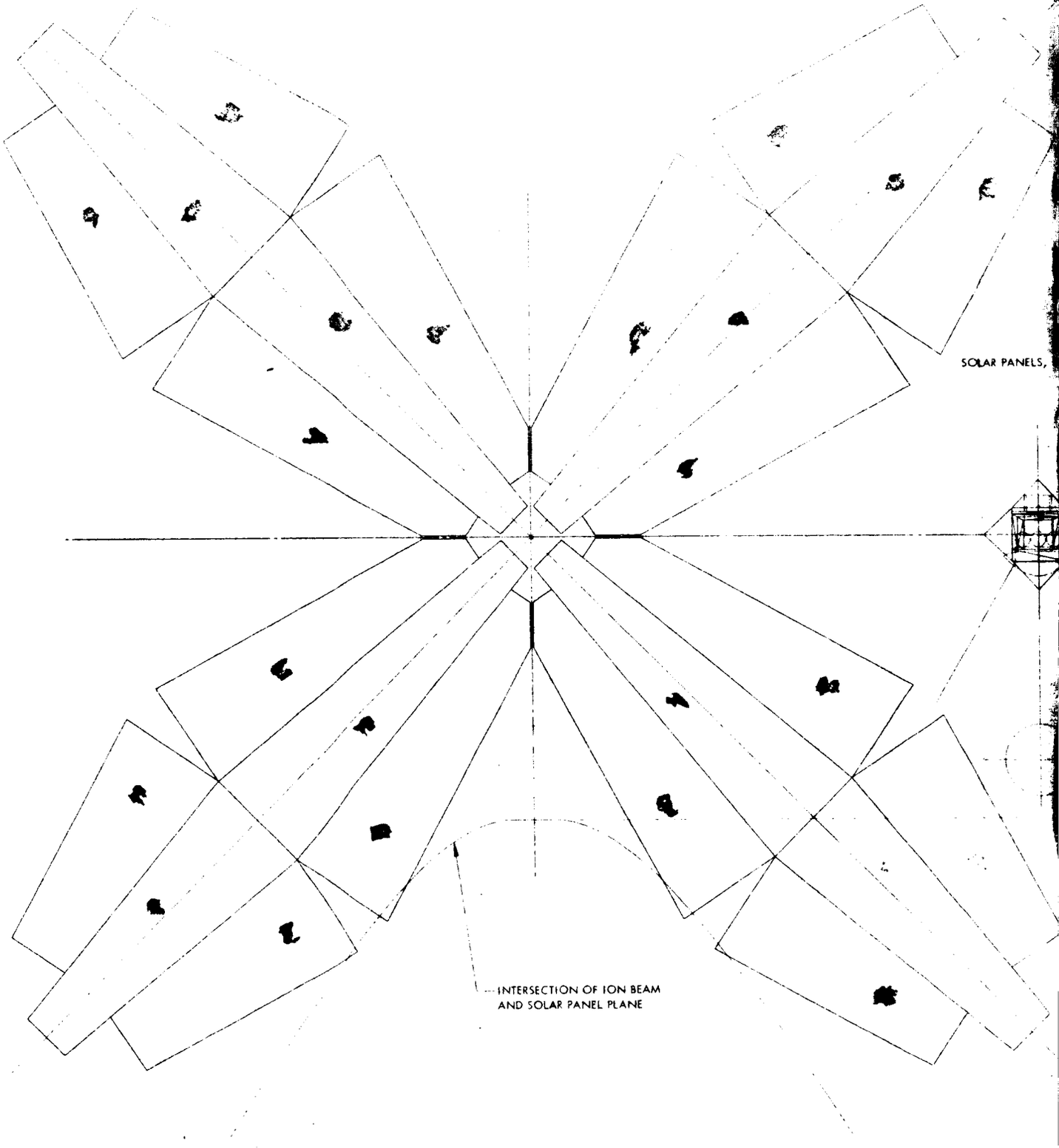

Figure C.1-4 Electric Propulsion Spacecraft

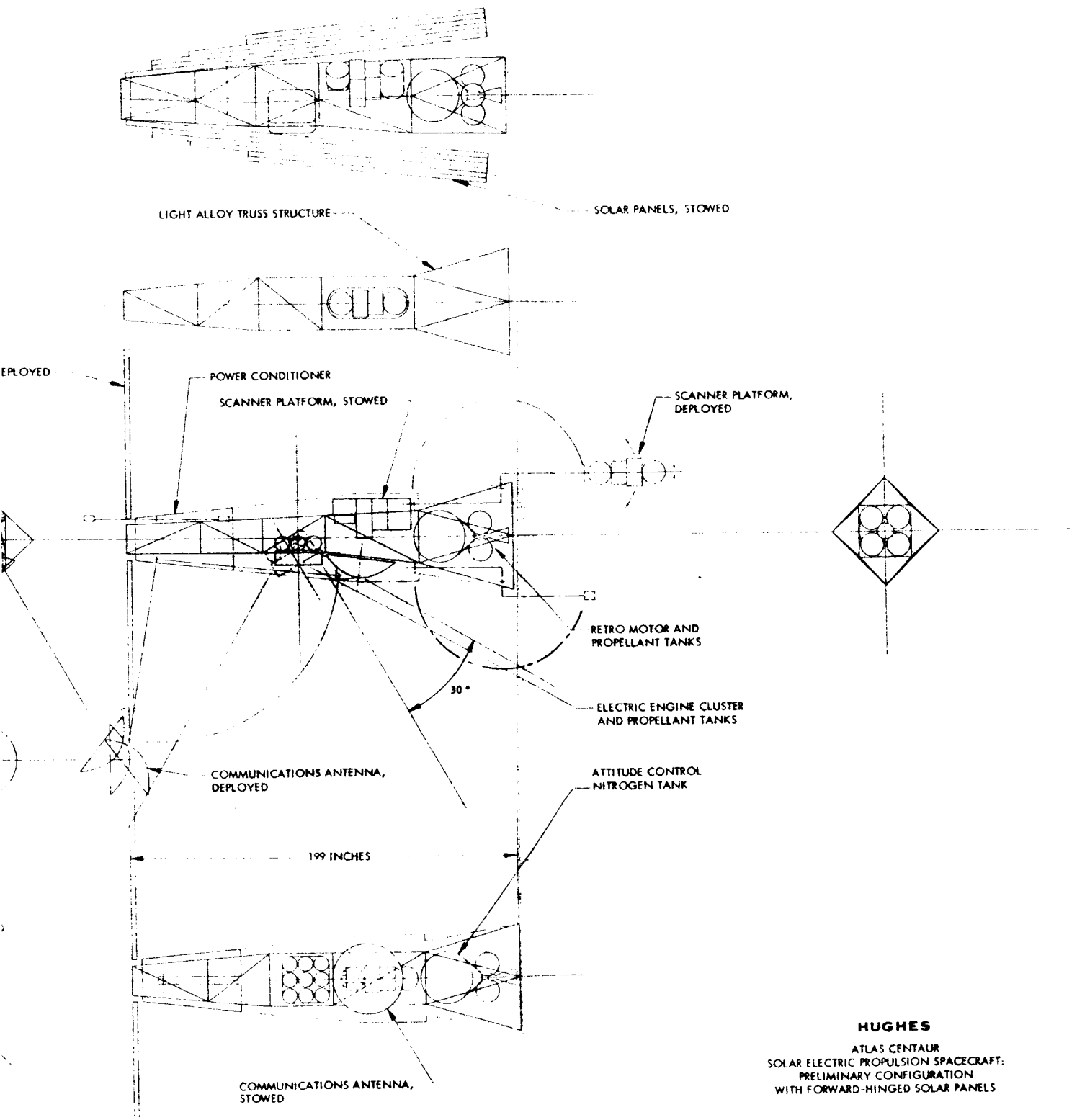

HUGHES

ATLAS CENTAUR
SOLAR ELECTRIC PROPULSION SPACECRAFT:
PRELIMINARY CONFIGURATION
WITH FORWARD-HINGED SOLAR PANELS

due to expenditure of attitude control nitrogen may be compensated by translation of the electric engine cluster.

The communication antenna is stowed at approximately the same station as the scanner platform and is rotated on an extendable mast to a deployed position between two solar panel arms. The antenna is retracted and recaged during retro-fire.

A preliminary weight breakdown applicable to the foregoing configuration is presented in Table C. 1-II

TABLE C. 1-II
Solar-Electric Propelled Atlas/Centaur Mars Orbiter
Weight Breakdown

	Wt.	Lbs.
PAYLOAD		133
TELECOMMUNICATIONS		165
GUIDANCE & CONTROL		221
ELECTRIC PROPULSION SYSTEM		1037
o Solar Array	550	
o Power Conditioning	85	
o Thrustors, Propellant, and Tankage	402	
RETRO-ROCKET		157
STRUCTURE		250
Total		1963

C.2 Thermal Control

During this reporting period several spacecraft configurations with different vehicle-thrustor relationships have been considered. The thermal aspects of the mercury pool cathode engine in both a remote position from the spacecraft and an integral position with respect to the spacecraft have been examined. The corresponding effects of the engine array on the thermal energy balance of the spacecraft has also been investigated.

The oxide cathode engine thermal characteristics are such that the vehicle temperatures can be made relatively independent of the location of the engine. Unlike the mercury pool cathode engine, no requirement exists to cool the cathode and in fact heat is added for the purpose of heating the cathode. The basic system thermal philosophy will therefore be to isolate the engine cathode from the spacecraft in order to limit heat losses from the engine to the spacecraft. Regardless of the positioning of the engine array with respect to the spacecraft proper thermal control of the spacecraft will be accomplished completely independent of the thermal control of the engines.

The mercury pool cathode engine requires the dissipation of approximately 130 watts of thermal energy from the engine cathode at temperatures no higher than 100°C. Several different vehicle-thrustor orientations have been examined from the point of view of total system thermal control. They are:

a. Engine array mounted integral with spacecraft-cathodes radiating into spacecraft.

b. Engine array mounted integral with spacecraft-cathodes radiating through spacecraft directly to space, and

c. Engine array mounted semi-remote from spacecraft-cathodes radiating from side radiators to space.

Configuration (a) allows for the cathode radiators to radiate the required 130 watts each into the spacecraft. The spacecraft will then re-radiate the energy to space. If it is assumed that the spacecraft

outer surface is all at 70°C (the expected temperature of the power conditioning panels which cover approximately 50% of the outer surface), the cathode radiators will be able to transfer only 60 watts each to the spacecraft outer surface even assuming that the spacecraft internal volume is relatively open and thus the cathode radiators are geometrically free to radiate in all directions. Since the 60 watts represents only about one half the required dissipating capability of the radiating system, the cathodes would rise to greater than the 100°C allowable maximum temperature. If the assumption is made that the spacecraft outer surfaces can be made to run at 30°C (excluding the power conditioning panels), the radiating capability of the cathode radiators is approximately the required 130 watts at 100°C. The system then, in light of the assumptions, appears marginally feasible.

Configuration (b) allows for the engine array to be mounted integral with the spacecraft but reserves a volume through the spacecraft as a "radiating corridor". The engine cathode radiators in this case can radiate through the corridor directly to space as well as radiate indirectly to space by multiple reflection from the corridor walls. The required 130 watts of thermal energy can then easily be radiated from each cathode and maintain maximum cathode temperatures well below the maximum allowable 100°C. The major disadvantage of this configuration, like configuration (a), is that a sizable portion of the spacecraft internal volume is non-usuable due to thermal radiation requirements.

The third configuration locates the engine array in a position semi-remote from the spacecraft. The cathode radiators are then configured as side radiators (instead of flat back radiators): thus, the dissipated energy is conducted to the peripheral side radiators and then radiated directly and by reflection from the spacecraft indirectly to space. The engine array will be thermally isolated from the spacecraft by a reflecting-radiating surface located between the engine array and the spacecraft structure.

Spacecraft thermal control is essentially obtained through balance of the energy dissipated in the power conditioning panels, other spacecraft internal power dissipation, and the radiating characteristics of all the spacecraft outside surfaces. In order to at least partially accommodate the relatively large change in energy balance on the spacecraft during transit from Earth to Mars, it is expected that a portion of the spacecraft outer surface will be utilized for an active thermal control, variable emittance device. This device will consist of movable vanes or louvers to change the emitting power of the controlled area by up to approximately one order of magnitude in response to changes in spacecraft internal temperature. A preliminary thermal analysis of the complete spacecraft system is currently in progress and is expected to determine the required extent of the active thermal control system.

C. 3. Spacecraft Attitude Control

Bi-Monthly Progress Report No. 2 described a study which indicated the feasibility of reducing the thrust misalignment disturbance torque of the solar electric propulsion vehicle by rotating or translating the ion engine bank until the thrust vector is closely aligned to the vehicle center of gravity and net disturbance torques reduced to tolerable levels.

Presented here is a study of the detailed operation of the ion engine bank translation mechanism in two modes. Also presented herein is a single axis acquisition analysis.

a. Operation of the Ion Engine Positioning Mechanism for the Solar Electric Propulsion Spacecraft.

Operation of the ion engine bank translation mechanism was investigated in two modes. First, reduction of the disturbance torque by force vector alignment was shown to require time periods up to two days for completion. This was due to long settling before steady state operation was obtained after corrections were made. Primary control in this case is assumed to be furnished by a separate reaction control system.

Secondly, use of the mechanism to provide primary control in two attitude channels was investigated and shown to be a feasible approach. Implementation of the engine bank positioning controller was chosen using a stepper motor driving frequency proportional to the error signal. This system requires an auxiliary control system for acquisition, attitude maneuvers, for control about the third axis, and for 3 axis control during orbit. This hybrid approach will be sized and compared with the other attitude control system alternatives in the next reporting period.

Uncertainty in alignment of the ion engine bank thrust vector with the spacecraft c. g. and subsequent movement of each during the mission results in an applied torque on the vehicle. If attitude control fuel is expended to cancel this disturbance torque, an inordinately large amount of control fuel would be required for the mission. To alleviate this requirement, the

engine bank is mounted through a motordrive mechanism which provides translational control in two degrees of freedom. The thrust vector to spacecraft c. g. misalignment can be computed from measurement of the steady-state limit cycle characteristics. This technique for generating translational commands is described in detail in Reference 1. The mechanism proposed for this function is described in Section C-1.

The engine alignment mechanism can be utilized in either of two modes. First, a separate attitude control channel can be used to maintain attitude while the thrust misalignment is treated as a disturbance torque. The correction procedure of Reference 3 would then be utilized. Second, the applied torque capability of the engine could be used to directly control 2 of the 3 attitude channels. Using this option, the motordriven engine bank would replace the gas jets during the transit phase of the mission.

1) Moment Arm Reduction

Requirements - The procedure for reducing the undesired moment arm as described in Reference 1, can be implemented as shown by the single axis block diagram of Figure C. 3-1. By periodically measuring the steady state limit cycle characteristics, a command would be generated only when the computed disturbance torque is greater than a maximum permissable level. The specified maximum level for this mission is 10^{-3} ft-lbs. This level is the maximum expected disturbance from sources other than misalignment, as discussed in reference 3. The maximum expected moment arm due to misalignment is currently $\pm$5inches. A nominal engine thrust level of .35 lbs. yields a disturbance of .146 ft-lbs. Hence a moment arm reduction to less than .0343" is required of the translation mechanism.

Iteration Time- One area of data missing from the analysis of reference 1 is the amount of time required for the attitude channel to return to steady state after a change in disturbance torque. This information determines how often successive moment arm corrections can be made. An analog simulation was made of the single attitude channel of Figure C. 3-1 with a function generator to vary the disturbance moment arm.

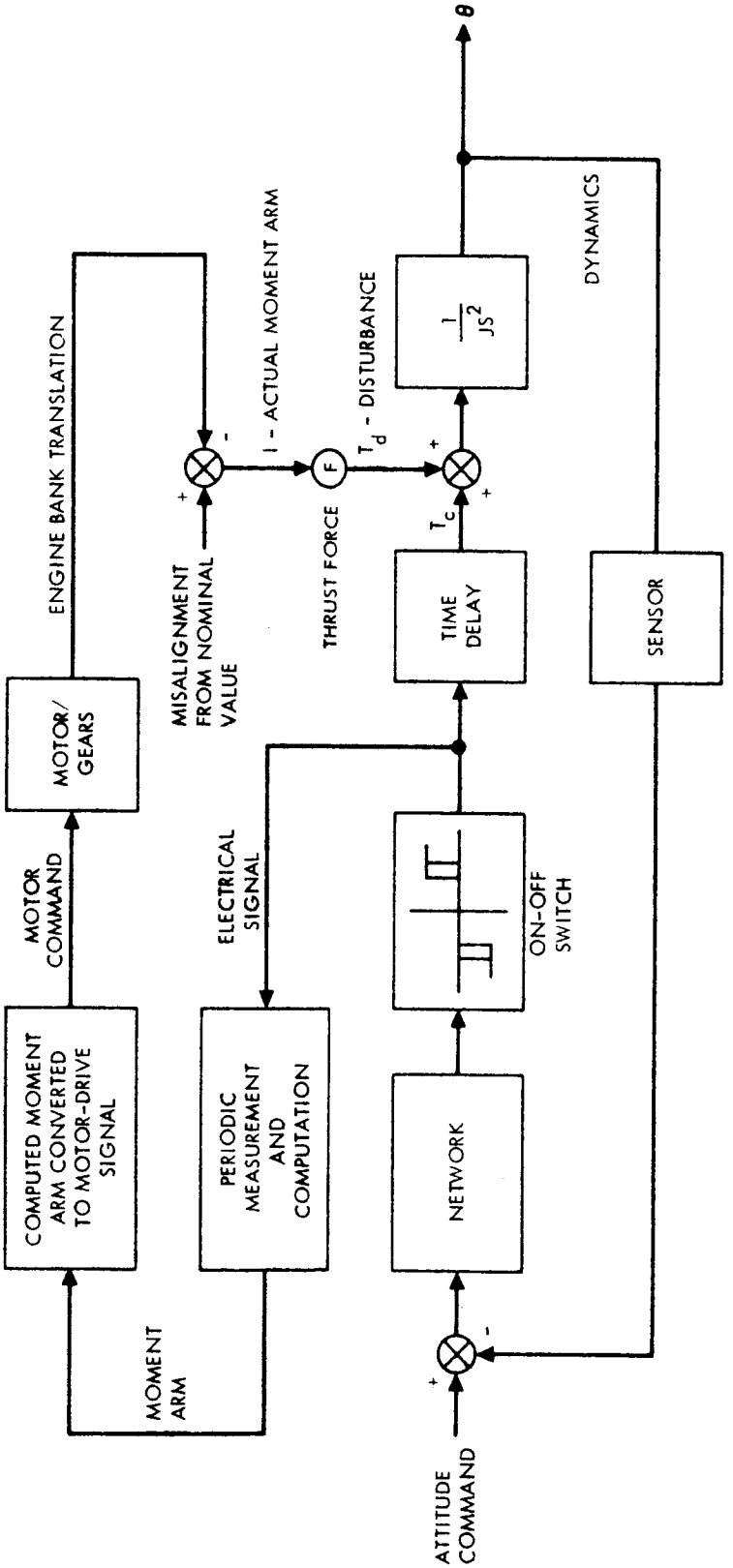

Figure C.3-1 Single Axis Block Diagram for Moment Arm Reduction

The behavior was observed when changing the disturbance from a maximum expected value to some percentage of maximum. This represented a computation of moment arm with an error; hence a second iteration would be required in normal operation. The elapsed time for settling to steady state would represent the time required before another accurate measurement could be taken. The settling time is shown as a function of percentage error in Figure C. 3-2. As the adjustment becomes more accurate the disturbance torque is being reduced from a maximum to a lower value. The soft duty cycle period consequently becomes longer and the settling time increases. In addition, as the disturbance is made smaller, the number of limit cycle oscillations before steady state is reached increases. This also increases the settling time.

It can be concluded from Figure C. 3-2 that a time between computations and corrections of about one day (86, 400 seconds) is required as small disturbance levels are approached. Since there is no way to predict the disturbance after corrections until accurate measurements are made, all reduction cycles should allow one day for settling time. Since at least two corrections must be provided, two days to reach an acceptable disturbance are required.

2) Continuous Control

Axis Configuration - The ion engine translation mechanism can be utilized to provide primary attitude control in 2 axes. The other axis would require a reaction jet system for control. Translation occurs in the coordinates of the engine bank while control is exercised in the spacecraft axes. The angle φ relates the two systems as shown by Figure C. 3-3. For an Earth-Mars trajectory, the nominal range of φ centers closely about 90° such that control about the body x (roll) and z (yaw) axes is suggested.

Loop Design Alternates - The discussion here is limited to roll and yaw since the pitch channel is cold gas which has been discussed before (reference 3). The means of moving the ion engine bank can be accomplished using a very low torque level motor. It appears that from

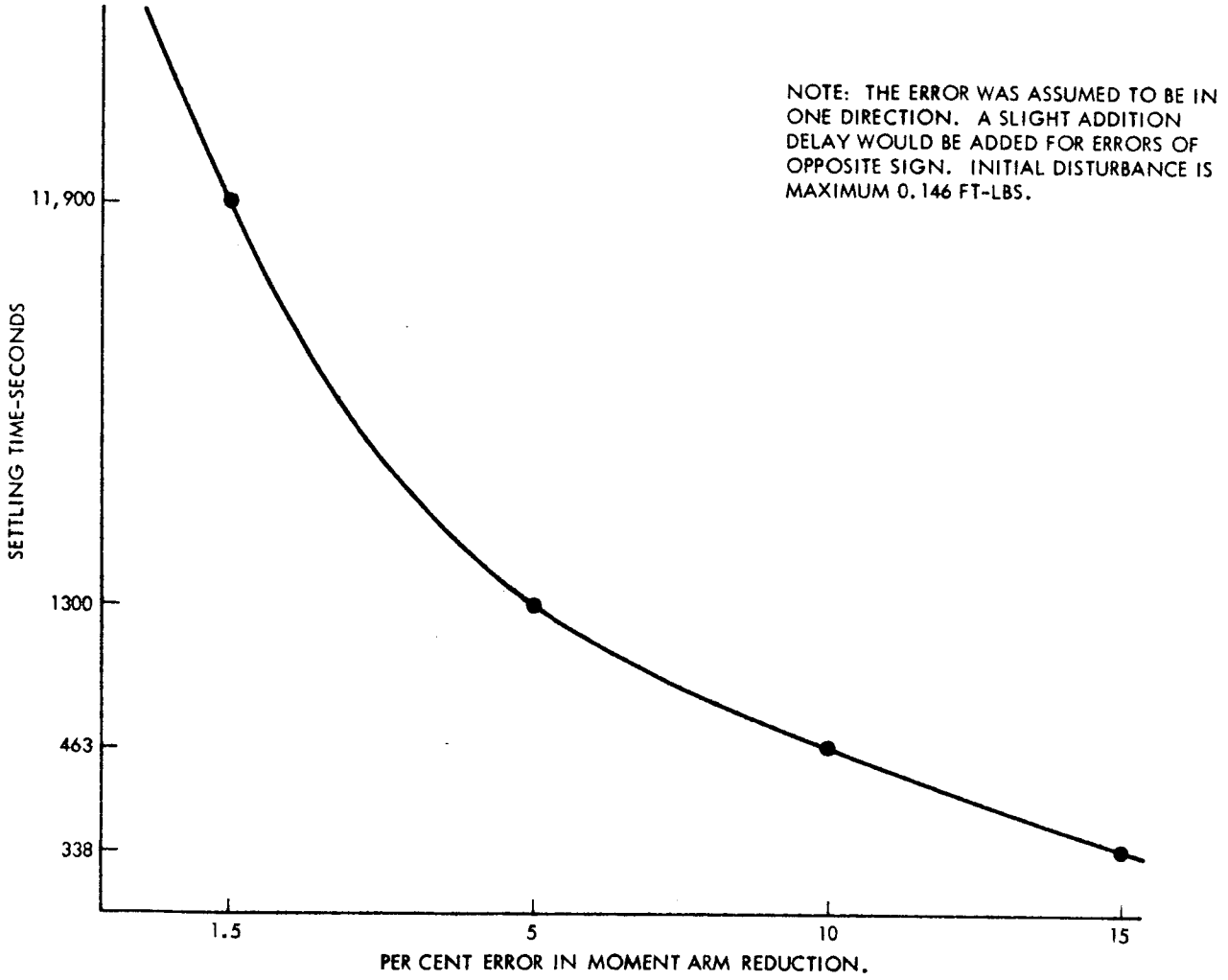

Figure C.3-2 Time to Return to Steady State After Moment Arm Change

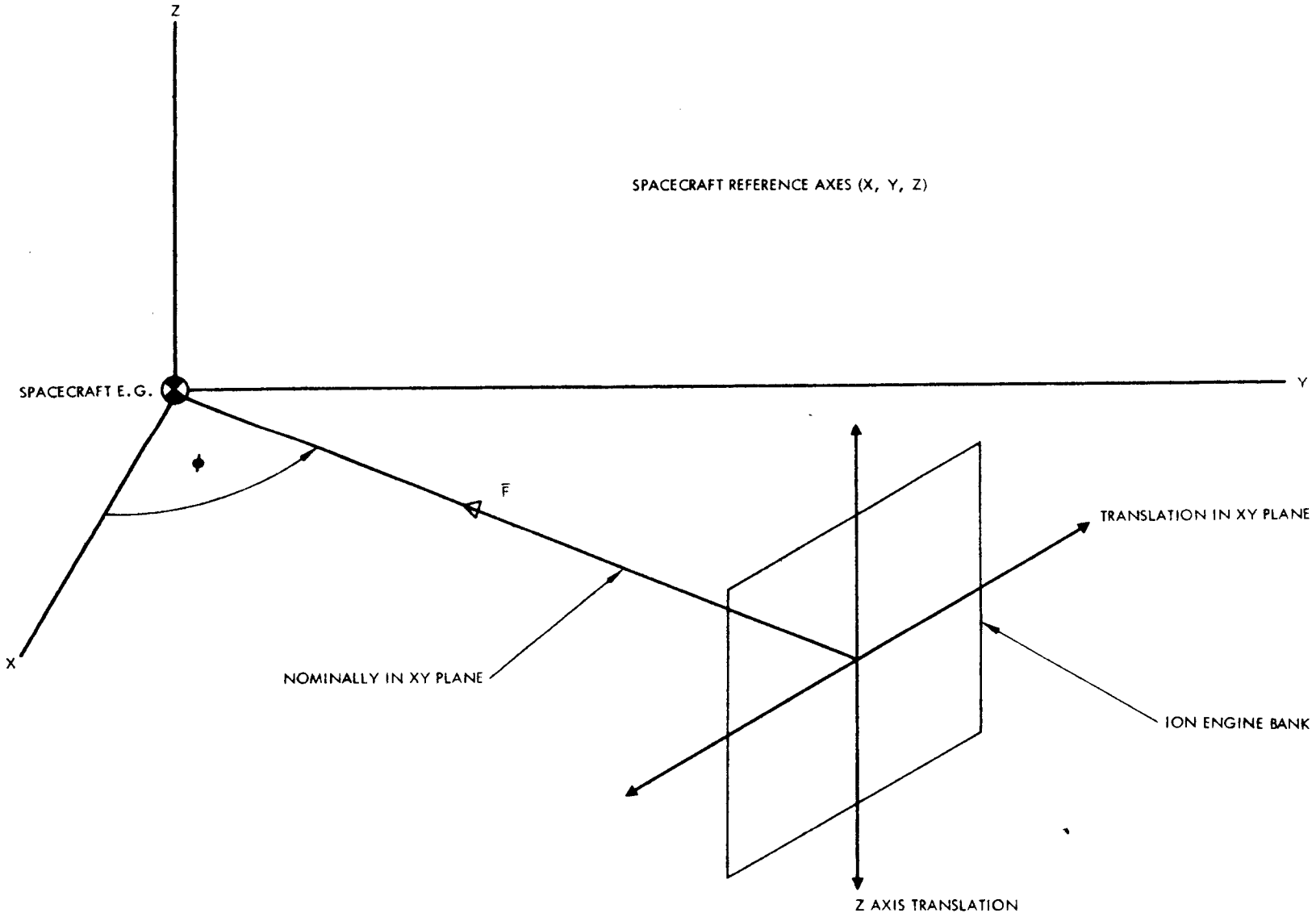

Figure C.3-3 Spacial Relationship of Spacecraft and Ion Engine Bank

the analytical standpoint either a stepper motor, dc torque motor, or ac servo motor would be suitable for use in a continuously operating servo loop. A stepper motor was chosen in reference 2 and is well qualified for a long duration spacecraft application. A potentiometer to measure the engine bank position provides a signal for closed loop servo controller operation. Two possible mechanizations for the stepper motor position controller are shown in Figure C. 3-4. The only significant difference is an on-off switch in 4a) while 4b) operates linearly. Since the stepper motor, unlike a torque or servo motor, does not operate in an energy storing mode, it is easier to stabilize and the shaping network is not required. In the case of the on-off controller, a pulse train of either polarity, but of constant frequency, is generated. For linear operation, the pulse converter can be mechanized using a voltage control oscillator (VCO), such that the motor is driven by pulses whose frequency is proportional to the input voltage. To make a choice of position loop mechanization the overall attitude channel must be considered. Figure C. 3-5 shows the commanded distance ℓ_c to be the output of a compensation network. To acheive adequate loop operation the shaping network (discussed in the following section) is predominately a lead network, i. e. higher frequencies are amplified. Hence the signal ℓ_c contains a large amount of inherent noise from the networks, sensors, etc. The on-off positioner is very sensitive to noise due to its poor filtering qualities, i. e. the first order motor transfer function is the only filter in the loop. This conclusion was verified by an analog computer simulation of the Figure C. 3-5 channel. Unintentional noise from the computer electronics made on-off operation difficult due to relay chatter. This had the effect of causing the system to respond slowly with poor stability characteristics. Consequently the linear system (Figure C. 3-4b) is chosen for the positioner mechanization.

Linear Design - To linearize the controller of Figure C. 3-4b two assumptions are made: First, each increment of the stepper motor is small compared to the total motion of interest. Second, the pulse rate for significant motions is fast compared to the response times of interest.

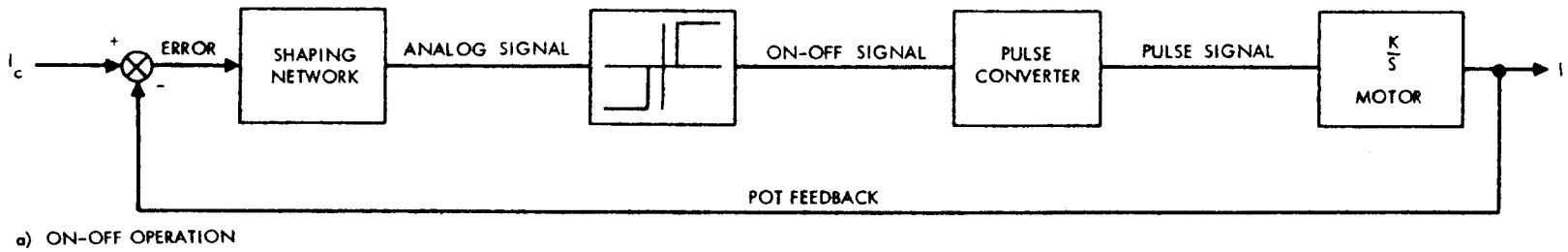

a) ON-OFF OPERATION

K - MOTOR GAIN, FT/PULSE

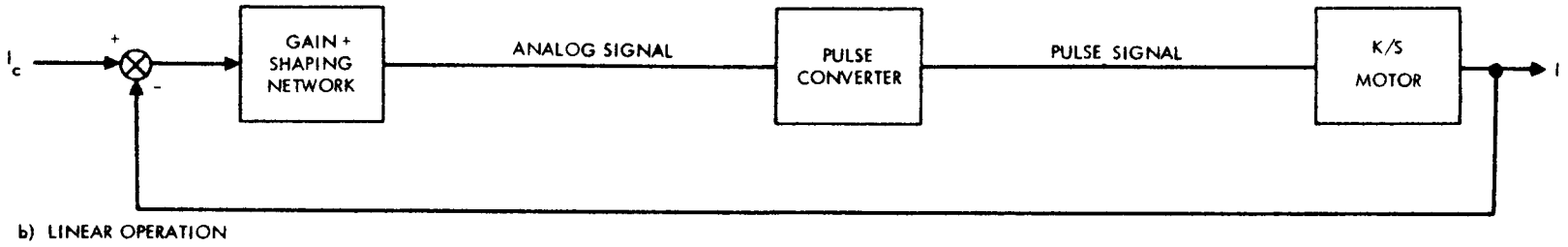

b) LINEAR OPERATION

Figure C.3-4 Position Controller Mechanization Alternatives

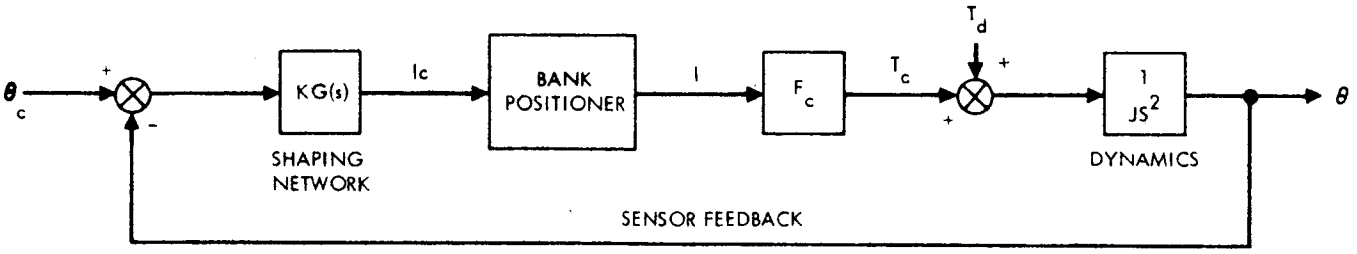

A) FUNCTIONAL BLOCK DIAGRAM

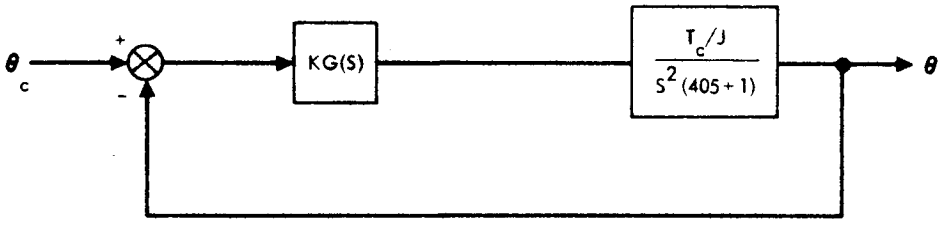

B) SIMPLIFIED LINEAR BLOCK DIAGRAM

Figure C.3-5 Attitude Channel Block Diagram

Hence, the motion resulting from a series of many small steps is assumed to be a smooth curve. If the network is assumed to be unity the resulting simplified loop and its equivalent transfer function are given by Figure C. 3-6.

The basic limitation on the position response time constant is fixed by the pulse frequency limit of the motor. To avoid trouble here the time constant $\tau_m = \frac{1}{K_1 K_2}$ is taken as 40 seconds. A double lead - lag network of $(30s+1)^2/(3s+1)^2$ is chosen for compensation of the attitude channel given by Figure C. 3-5b. For this network a root locus diagram is shown in Figure C. 3-7. A damping ratio of . 4 is used as a criterion for adequate operation. Hence a range between points 1 and 2 is suitable. The upper limit for which the root locus gain is . 0151 is chosen since faster time response is thus obtained. The time response is also affected by the two real roots at approximately . 03 and . 17. The . 03 root is of low residue and doesn't contribute significantly to principle time constant. Lead zeros at $\frac{1}{30}$ radians/second were chosen because this represents a realizable network. Better characteristics are realized with this network.

System Operation - A single attitude channel was simulated on the analog computer. The primary purpose was to investigate the positioning motor in an on-off mode of operation. This mechanization was shown to be extremely noise susceptible as discussed previously. Hence the linear mechanization was chosen. The simulation was then used to verify the straightforward linear analysis and evaluate the loop performance under various conditions.

Using the engine bank for primary control during transit can only be accomplished after deployment and acquisition are accomplished. Hence an auxiliary reaction jet system is required. Analog results showed that vehicle rates should be less than . 02 deg/sec. when engine bank control is initiated and acquisition control terminated. The attitude error is reduced to zero by the linear system and a steady state limit cycling mode is no longer used.

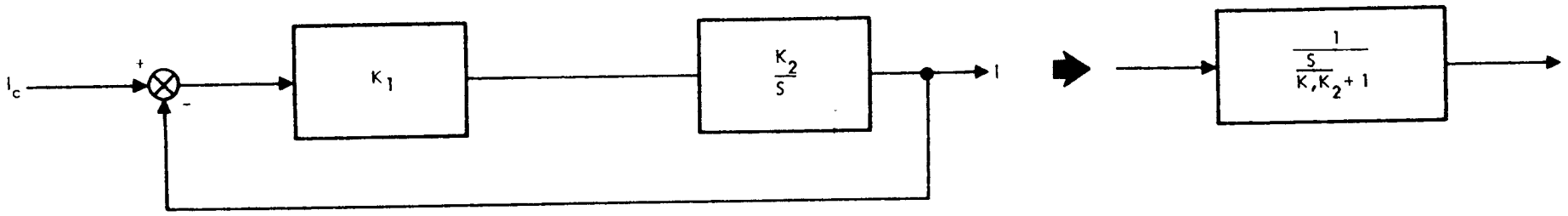

K_1 - $\frac{\text{PULSES/SEC}}{\text{FT}}$

K_2 - FT/PULSE

Figure C.3-6 Simplified Positioner

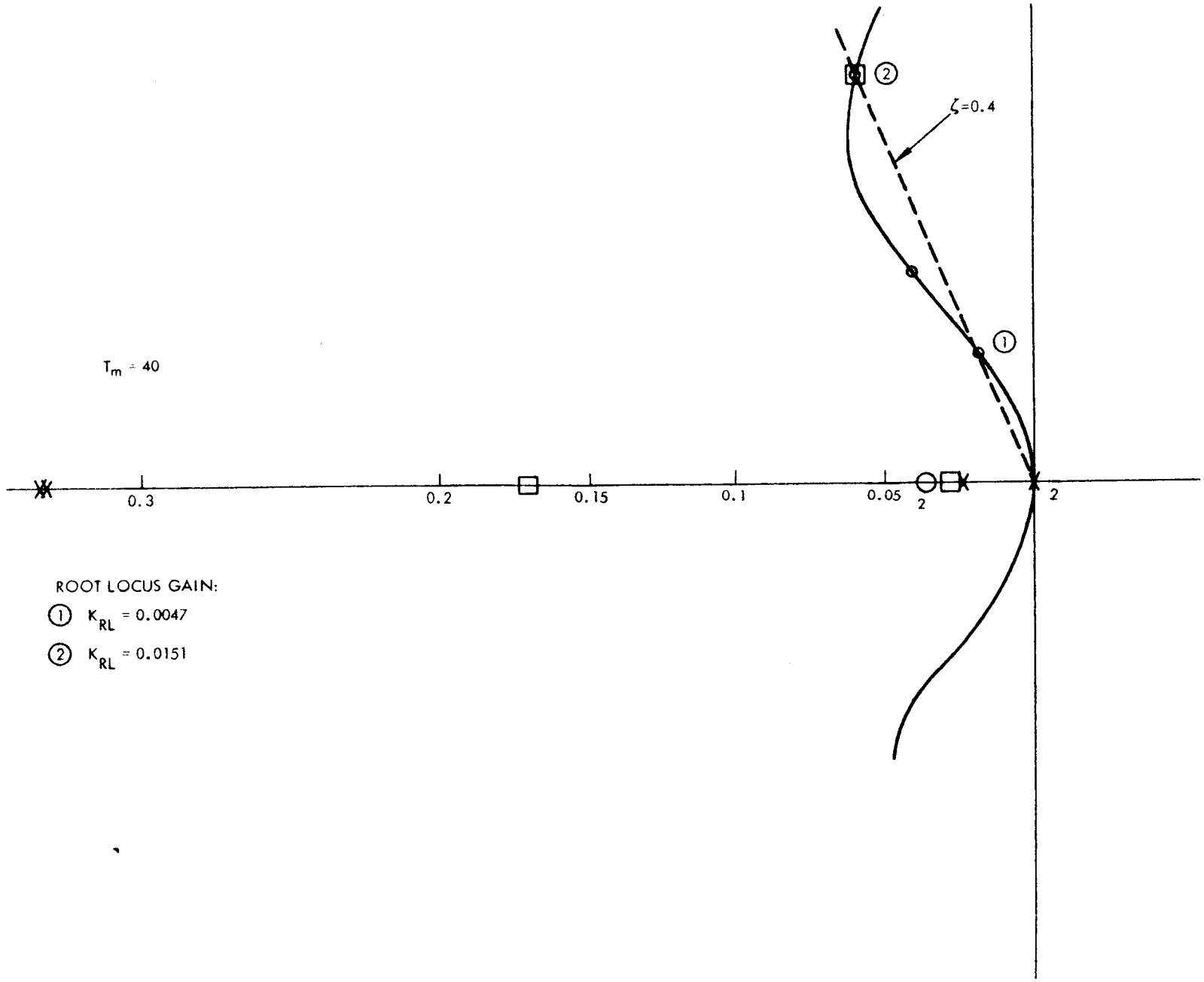

Figure C.3-7 Root Locus of Attitude Channel

The response to a simultaneous application of disturbance torque (10^{-3} ft-lbs max.) and engine bank misalignment (5 inches max.) was favorable under worse case conditions. The resulting transient was well damped and settled out within 50 seconds. Under these conditions, the maximum pulse repetition rate into the stepper motor was well within its capabilities.

Referring to Figure C. 3-3, if φ is 90° the z axis translation provides control in roll (x axis). If φ is some small angle ($\pm 10^{\circ}$ max.) away from 90° then roll control signals present a disturbance torque into pitch (y axis). Since large roll control signals only exist for a short time they will not cause an undue expenditure of fuel in the pitch channel. During the steady-state cruise phase this disturbance is consequently negligible.

b. Single Axis Acquisition Analysis

Typical (single axis) acquisition thrust-time profiles are presented here utilizing phase plane and rate diagram techniques. Initial tumble rates of 1 deg/sec or less are assumed prior to solar array deployment, and the preliminary system parameters given in Reference 3 are utilized. In addition, the deadband is relaxed from $\pm$ 1 degree to ± 2 degrees. Acquisition thrust-time profiles are determined keeping all other system parameters fixed. The purpose of these preliminary analyses was to provide representative thrust-time profiles in order that dynamic interactions with the large flexible solar panels may be evaluated.

A performance tradeoff is also presented for the disturbance-torque free limit cycle fuel consumption (duty cycle) as a function of the lead-lag network parameters. The results indicate that a larger effective lead time constant will produce less fuel consumption in the hard limit cycle; however, due to the expected existence of significant disturbance torques throughout the mission, the system fuel capacity must be sized to accommodate the peak expected disturbance torque. Therefore, the only requirement on the hard limit cycle is that duty cycle must be less than that due to the peak disturbance torque duty cycle. This condition is not quite met by the system parameters of Reference 3 for $\theta_d = \pm 2$ degrees. The lead-lag parameters are therefore increased to meet this requirement for both $\theta_d = \pm$ 1 degree and $\theta_d = \pm 2$ degrees.

The preliminary control system evaluation (Reference 3) for the solar-electric spacecraft resulted in the selection of a cold gas (N_2) attitude control system. This system is represented in Figure C. 3-8. System parameters (from Reference 1) are given in Table I

TABLE I

Preliminary Control System Parameters

Moment of Inertia, I	
Pitch Yaw	30,000 slug-ft^2
Roll	60,000 slug-ft^2
Control Thrust, T_C	.025 lb.
Control Moment Arm	20 feet
Control Acceleration, $T_C/I = \lambda$	
Pitch-Yaw	1.67×10^{-5} rad/sec^2
Roll	$.833 \times 10^{-5}$ rad/sec^2
Hysteresis, h	2% θ_d
Deadband, θ_d	$\pm$ 1 deg
Lead, τ_1	7.25 sec
Lag, τ_2	0.60 sec

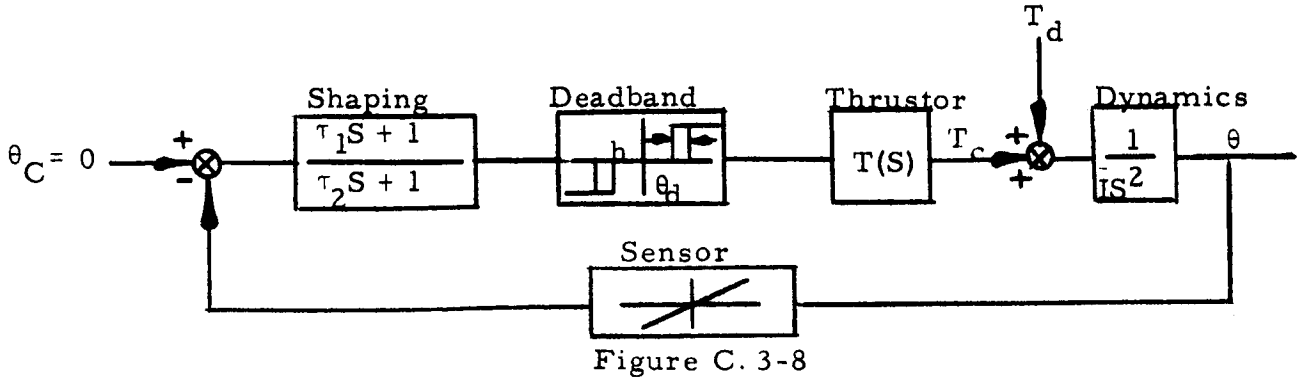

Figure C. 3-8

Representative Attitude Control Channel

The initial acquisition maneuver may be evaluated for a single axis via the rate diagram technique described in Reference 4. This technique results in a plot of the final vehicle rate, $\dot{\theta}_f$, as a function of the initial vehicle rate, $\dot{\theta}_o$, assuming that all transients die out between thrustings and that disturbance torques may be neglected. From the rate diagram, a phase plane portrait may be constructed for any given vehicle initial condition, and the system limit cycle may also be determined by the condition $\dot{\theta}_o = -\dot{\theta}_f$.

The rate diagrams for the pitch-yaw channels and the roll channel are illustrated in Figure C. 3-9, utilizing the parameters of Table I. The convergence to limit cycle operation will be somewhat slow, as evidenced by the closeness of the rate diagrams to the minus one line; i. e. the rate diagram for large rates may be approximated by the equation:

$$\dot{\theta}_f = -\dot{\theta}_o + \Delta\dot{\theta} \qquad (1)$$

where the $\Delta\dot{\theta}$ per correction is small for a relatively slowly converging case. The value of $\Delta\dot{\theta}$ is a function of the effective lead time constant of the system $(\tau_1 - \tau_2)$, and faster convergence to low duty cycle operation can be achieved by increasing $(\tau_1 - \tau_2)$ if desired.

From the rate diagrams of Figure C. 3-9, the phase plane portraits representing convergence to low duty cycle operation from an initial tumble rate are illustrated in Figures C. 3-10 and C. 3-11. Tumble rates of 1 deg/sec in all axes were assumed prior to solar array deployment, and due to assumed deployment inertial increases of 8 in pitch-yaw and 16 in roll, the initial tumble rates become 0.12 deg/sec in pitch yaw and 0.06 deg/sec in roll. The typical single axis thrust-time characteristics from Figures C. 3-10 and C. 3-11 are summarized in Table II for the purposes of estimating possible coupling between the attitude control system and the flexible solar arrays. These characteristics represent only estimates, since neither inertial cross-coupling between the axes nor possible non-linear sensor characteristics were included in the preceding single axis analysis.

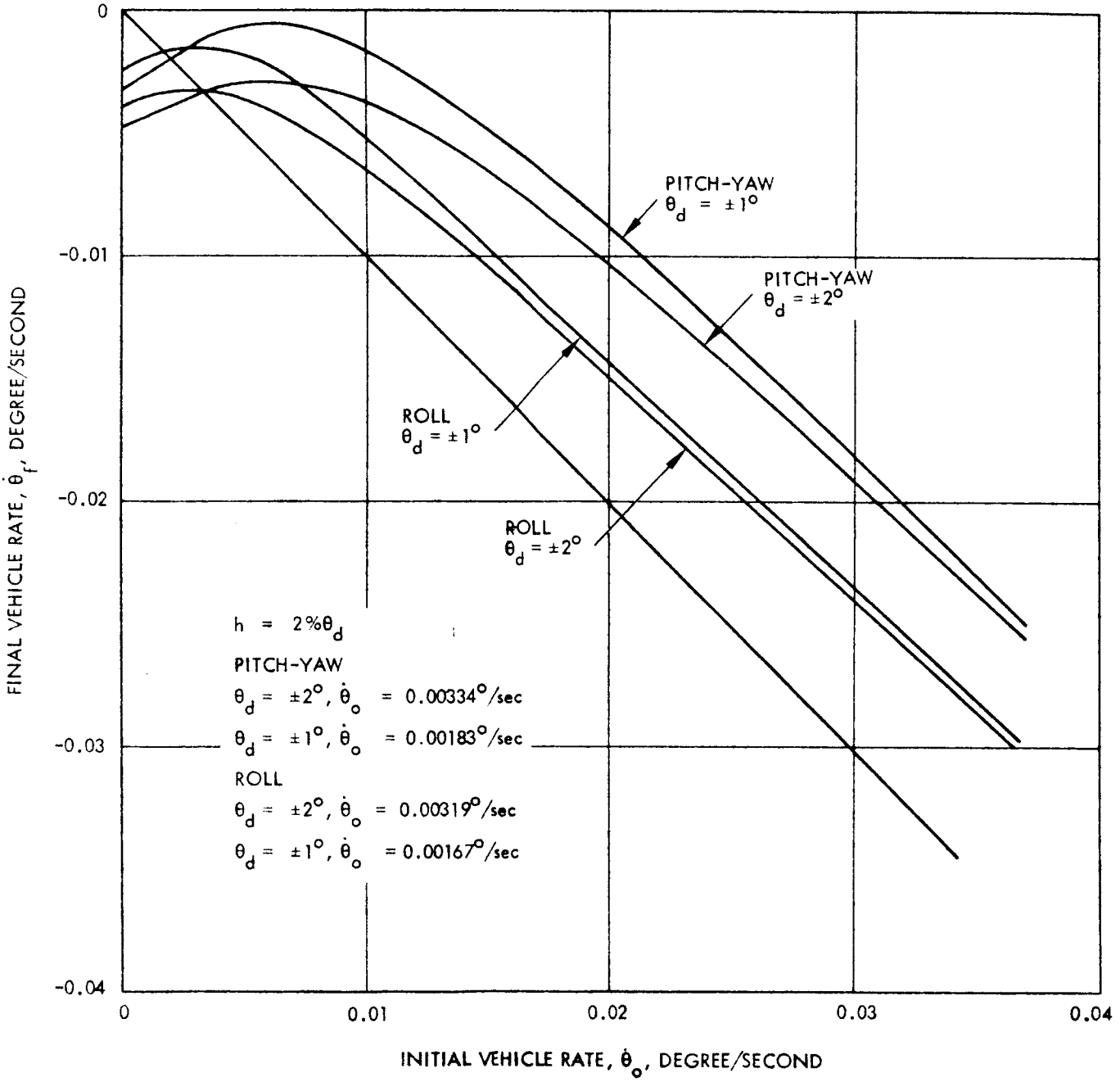

Figure C.3-9 Roll and Pitch-Yaw Rate Diagrams

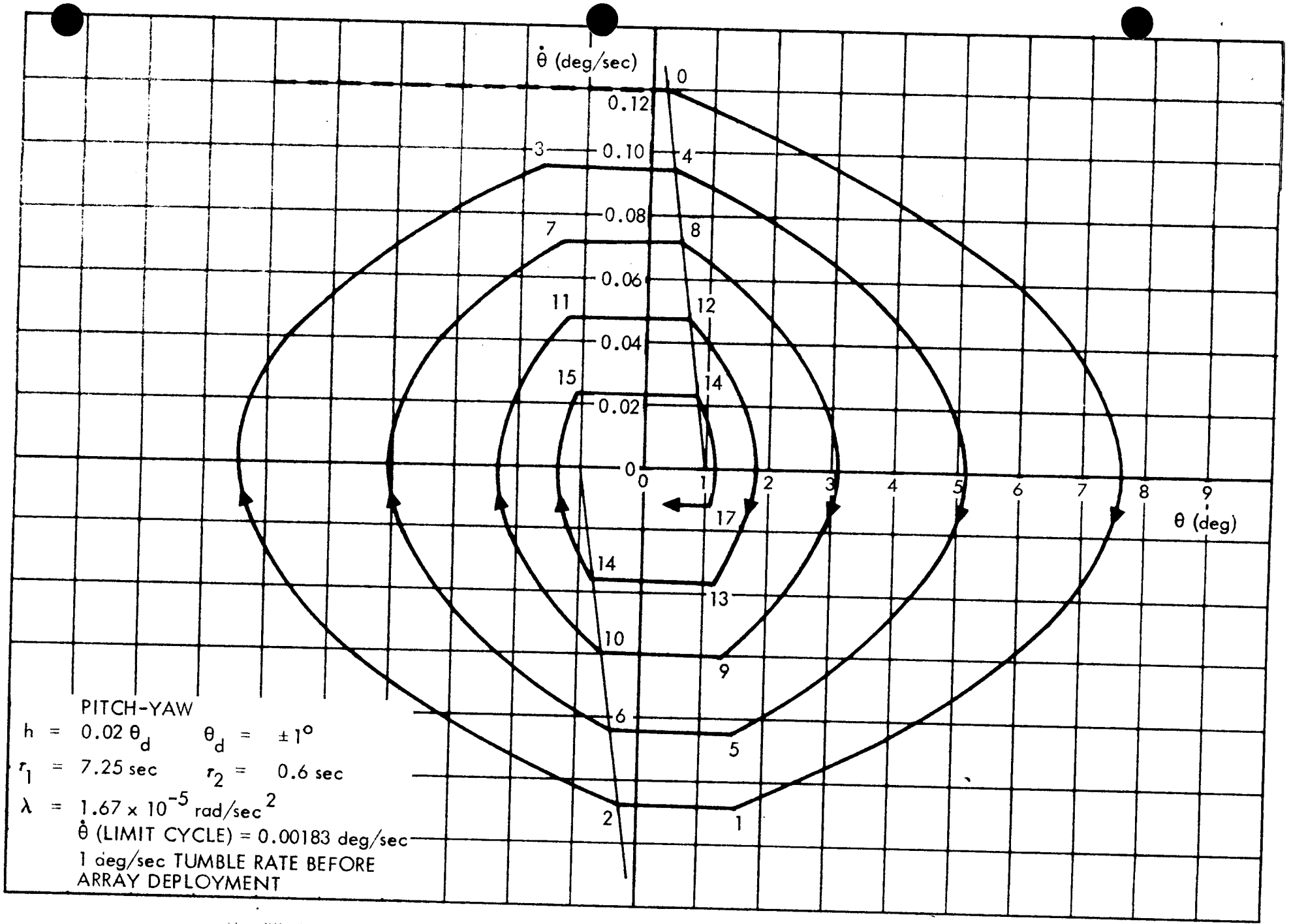
$\dot{\theta}$ (deg/sec)
0.12
0.10
0.08
0.06
0.04
0.02
0
θ (deg)
0 1 2 3 4 5 6 7 8 9
PITCH-YAW
h = 0.02 θ_d θ_d = ±1°
r_1 = 7.25 sec r_2 = 0.6 sec
λ = 1.67 x 10^{-5} rad/sec^2
$\dot{\theta}$ (LIMIT CYCLE) = 0.00183 deg/sec
1 deg/sec TUMBLE RATE BEFORE ARRAY DEPLOYMENT

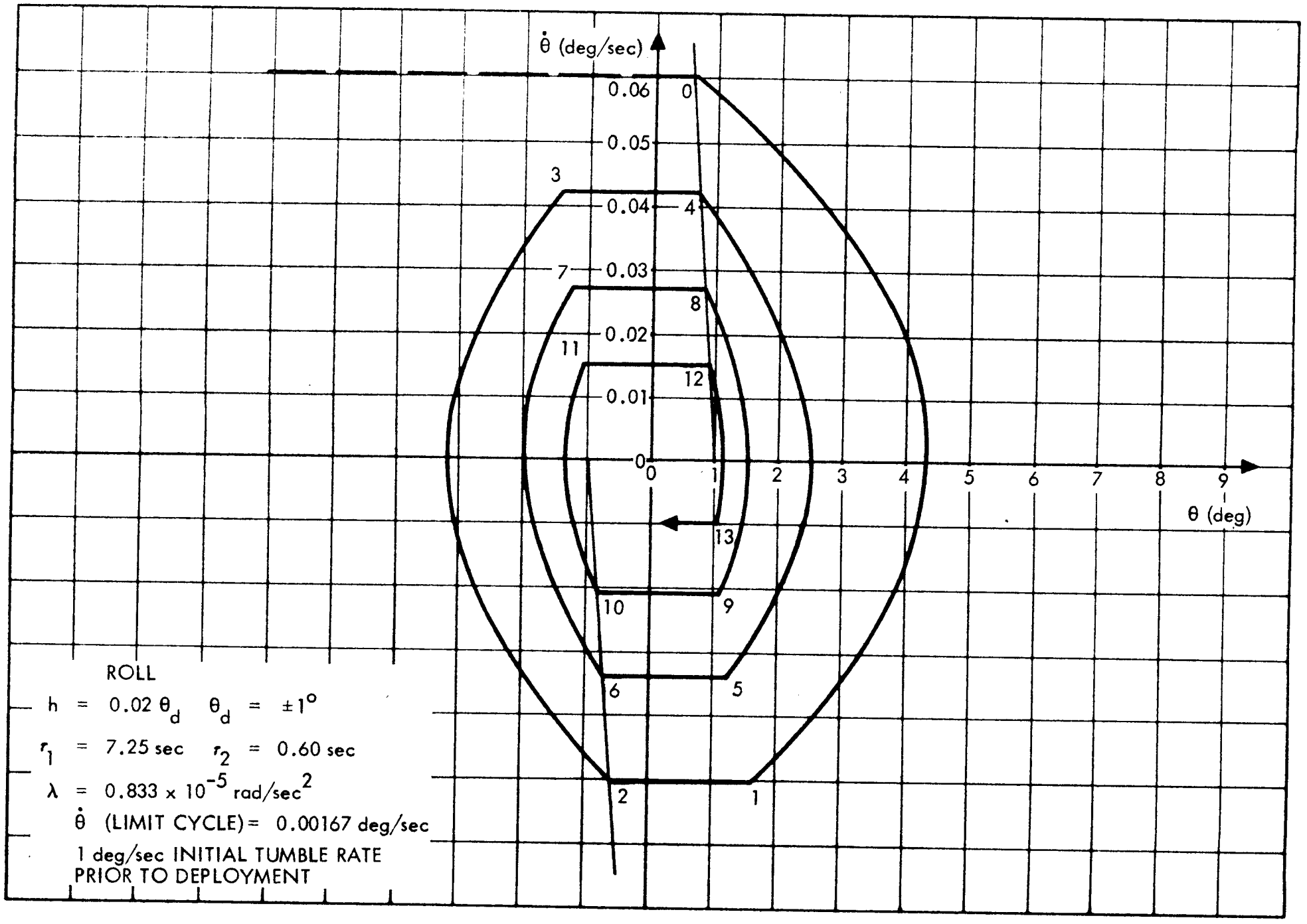

Figure C.3-11 Phase Plane Portrait of Roll Transient Response, $\theta_d = \pm 1^\circ$

The system acquisition performance was also evaluated for an attitude deadband of $\pm$ 2 degrees, utilizing all other system parameters of Table I. The rate diagrams are illustrated in Figure C. 3-9, and the resulting phase plane portraits for roll and pitch-yaw are illustrated in Figures C. 3-12 and C. 3-13. The thrust-time histories for this system are given in Table III, and are seen to be similar to those for $\theta_d = \pm$ 1 degree (Table II), except that initially the coast times are twice as long due to the larger deadband.

Although acquisition performance is acceptable for $\theta_d = \pm$ 2 degrees keeping all other system parameters identical with those of Table I, the lead-lag network parameters may not necessarily represent an "optimum" system design in the sense of minimum fuel usage in a hard limit cycle mode. Since fuel capacity is actually based upon operation with a maximum expected disturbance torque of 10^{-3} ft-lb, minimization of hard limit cycle fuel consumption is not a rigid requirement. However, hard limit cycle fuel consumption (disturbance-torque-free) should be required to be equal to or less than that for the soft limit cycle under the maximum expected disturbance torque.

For the system parameters of Table I (including $\theta_d = \pm$ 1 degree), the limit cycle rates in the pitch-yaw and roll axis are 1.83×10^{-3} deg/sec and 1.67×10^{-3} deg/sec respectively, and the corresponding limit cycle thrust times are 3. 78 seconds and 6. 96 seconds respectively. The (disturbance torque free) limit cycle duty cycles for a $\pm$ degree deadband are then 0. 35% in pitch-yaw and 0. 58% in roll (fuel consumption is proportional to duty cycle). Therefore, for $\theta_d = \pm$ 1 degrees, the requirement that hard duty cycle is not quite met (a disturbance torque of 10^{-3} ft-lb results in a duty cycle of 0. 20% for the assumed control torque of 0. 5 ft-lb). For $\theta_d \pm$ 2 degrees, the requirement is again not met, as the roll and pitch-yaw hard limit cycle rates are respectively 3.34×10^{-3} deg/sec and 3.19×10^{-3} deg/sec, and resulting hard duty cycles are respectively 0. 58% and 1. 06%. Hence, a reselection of system parameters is desirable in order to meet the hard duty cycle design requirements.

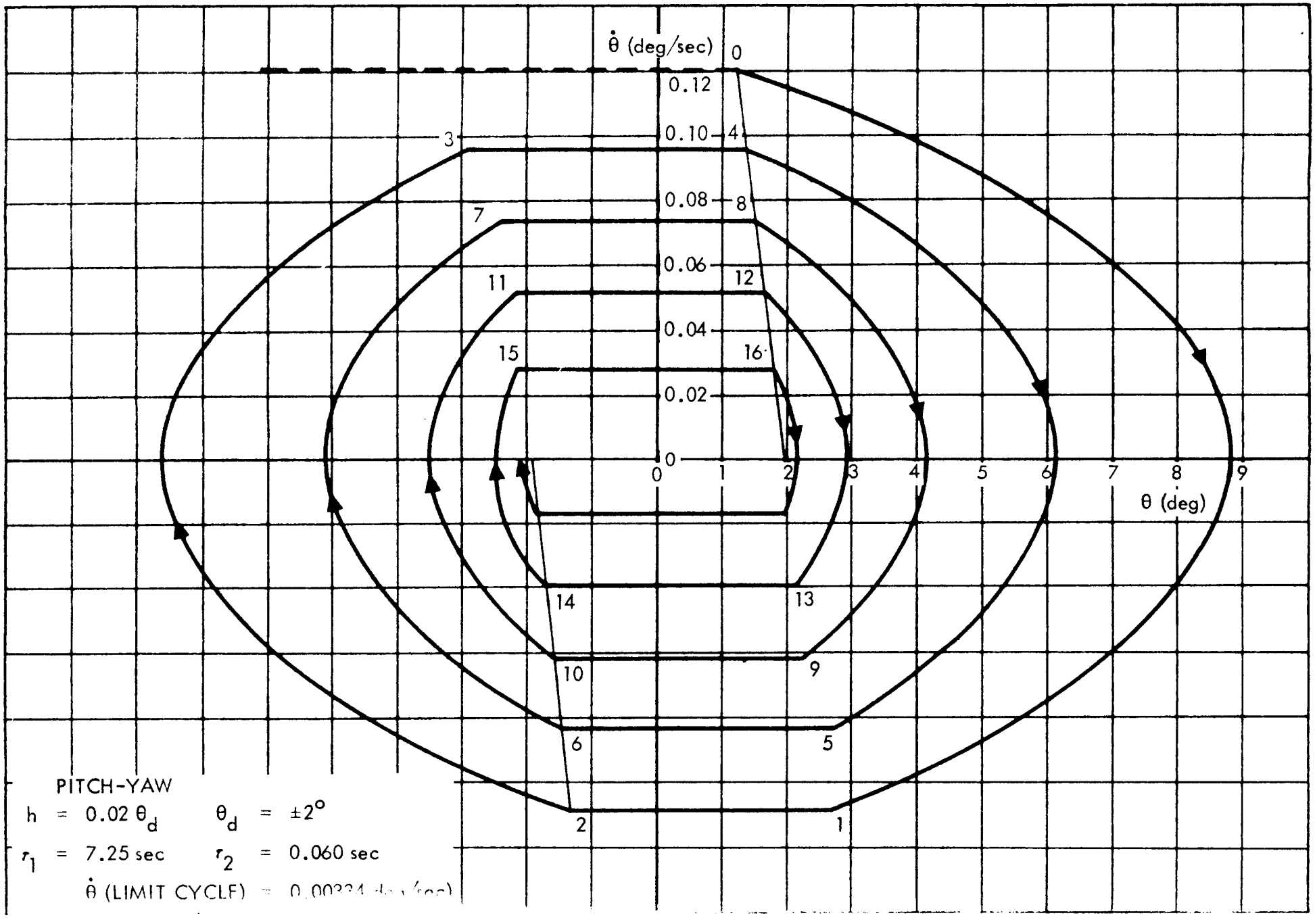

FIGURE C.4-1 Phase Plane Portrait of Pitch-Yaw Transient Response, $\theta_d = 2^\circ$

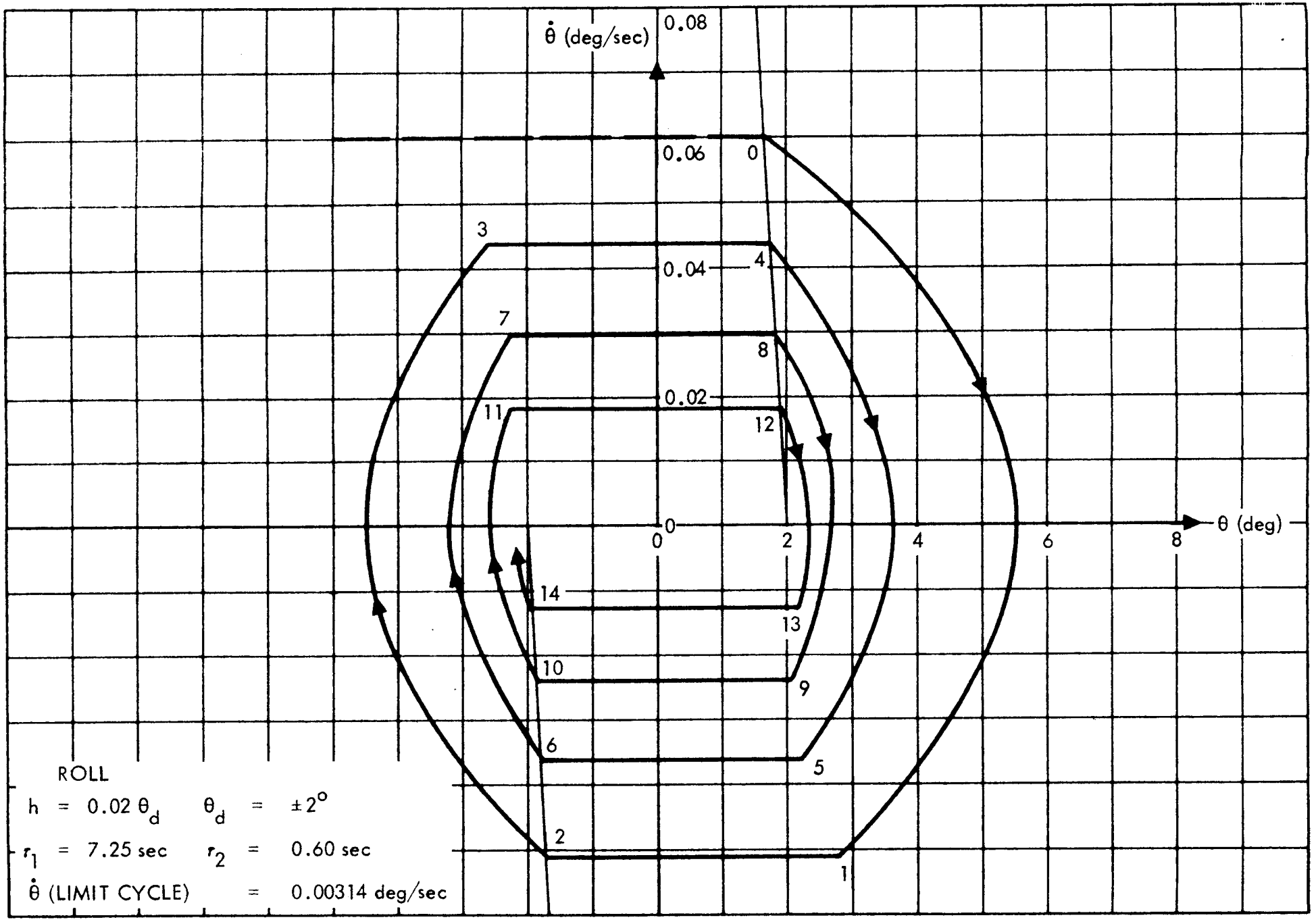

FIGURE C.3-13 Phase Plane Portrait of Roll Axis Transient Response, $\theta_d = \pm 2^\circ$

Table II

Thrust-Time Histories, $\theta_d = \pm 1$ Degree

	Roll	Pitch-Yaw
t_{01} (thrust)	231 seconds	238 seconds
t_{12} (coast)	39.6	18.5
t_{23}	193	213
t_{34}	47.6	20.8
t_{45}	159	188
t_{56}	58.5	23.8
t_{67}	128	163
t_{78}	73.3	27.8
t_{89}	101	138
t_{9-10}	95.3	33.4
t_{10-11}	75.5	113
t_{11-12}	132	41.7
t_{12-13}	52.6	87.4
t_{13-14}	200	55.9
t_{14-15}	31.4	62.1
t_{15-16}	400	84.3
t_{16-17}	14.2	37.5
t_{17-18}	111.1	164
t_{18-19}	•	15.9
t_{19-20}	•	666
	•	
t (thrust) limit cycle	6.96	3.78
t (coast) limit cycle	1200	1092

Table III

Thrust-Time Histories, $\theta_d = \pm 2$ degrees

	Roll	Pitch-Yaw
t_{01} (thrust)	233 seconds	239 seconds
t_{12} (coast)	87.9	36.9
t_{23}	198	210
t_{34}	98.9	41.2
t_{45}	167	191
t_{56}	110.2	46.8
t_{6-7}	138	167
t_{7-8}	134.3	54.1
t_{8-9}	112.2	143
t_{9-10}	167.2	64.0
t_{10-12}	87.7	118.8
t_{11-12}	221	78.4
t_{12-13}	64.5	94.7
t_{13-14}	31.3	101.2
t_{14-15}	43.9	70.7
t_{15-16}	48.7	143
t_{16-17}	27.6	47.3
t_{17-18}	1800	231
t_{18-19}	17.75	26.3
t_{19-20}	114.4	512
t_{20-21}	•	11.4
t_{21-22}	•	1332
t (thrust) limit cycle	13.31	6.95
t (coast) limit cycle	1255	1198

For a system of the type shown in Figure C. 3-8, the hard duty cycle can be minimized if desired by selection of a large ($\tau_1 - \tau_2$) for a fixed ratio τ_1/τ_2. This minimization for $\theta_d = \pm 1$ degree is illustrated in Figure C. 3-14 * for both roll and pitch-yaw, and selection of larger values of τ_1, τ_2 than those of Reference 1 will reduce the hard duty cycle to the desired value ($< .20\%$). The flatness of the curve as τ_1 increases indicates little improvement of duty cycle occurs for $\tau_1 > 25$ seconds; hence $\tau_1 = 22$ seconds, $\tau_2 = 2.2$ seconds is selected for $\theta_d = \pm 1$ degree, resulting in acceptable hard duty cycles of .16% and .19% in pitch-yaw and roll respectively.

It can be shown that the values of $\tau_1 - \tau_2$ required for $\theta_d = \pm 2$ degrees for a fixed hard duty cycle will be larger than for $\theta_d = \pm 1$ degree, due to the proportionality of hysteresis to attitude deadband and resulting proportionality of hard duty cycle to deadband. The variation of $\dot{\theta}_o$ with τ_1 is also illustrated in Figure C. 3-14, for $\theta_D = \pm 2$ degrees, the flatness of the curves indicating negligible reduction of hard duty cycle for $\tau_1 > 30$ seconds. Hence, selection of $\tau_1 = 30$ seconds and and $\tau_2 = 3$ seconds for all three axes will provide an acceptable design, with a relatively small size and weight capacitor required for mechanization of the lead-lag network. The resulting hard limit cycle rates are 1.78×10^{-3} deg/sec in pitch-yaw and 1.37×10^{-3} deg/sec in roll, with hard duty cycles of 0.16% and 0.19%, approximately equalling the maximum soft duty cycle of 0.20%.

---

* Hard duty cycle (d_H) is proportional to the square of limit cycle rate, i.e., $d_H \cong \dot{\theta}_o{}^2/\lambda\theta_d$; hence, for a fixed λ and θ_d, a minimum of $\dot{\theta}_o$ (τ_1, τ_2) will also be a minimum of d_H.

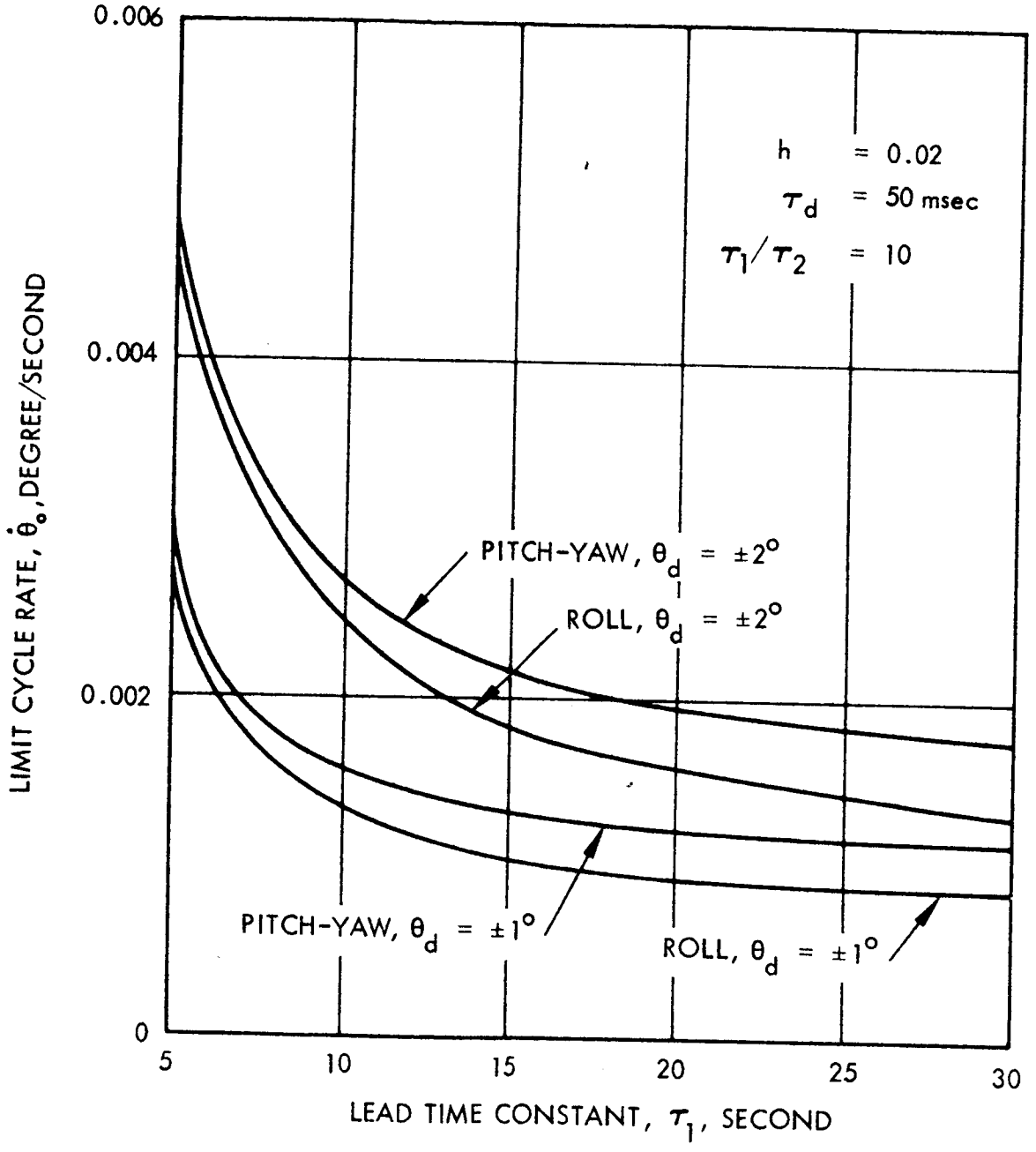

Figure C.3-14 Variation of Hard Limit Cycle Rate with Lead Time Constant

It can be shown that the values of $\tau_1 - \tau_2$ required for $\theta_d = +2$ degrees for a fixed hard duty cycle will be larger than for $\theta_d = \pm 1$ degree, due to the proportionality of hysteresis to attitude deadband and resulting proportionality of hard duty cycle to deadband. The variation of $\dot{\theta}_o$ with τ_1 is also illustrated in Figure C. 3-14, for $\theta_D = \pm 2$ degrees, the flatness of the curves indicating negligible reduction of hard duty cycle for τ_1 30 seconds. Hence, selection of $\tau_1 = 30$ seconds and $\tau_2 = 3$ seconds for all three axes will provide an acceptable design, with a relatively small size and weight capacitor required for mechanization of the lead-lag network. The resulting hard limit cycle rates are 1.78×10^{-3} deg/sec in pitch-yaw and 1.37×10^{-3} deg/sec in roll, with hard duty cycles of 0.16% and 0.19%, approximately equalling the maximum soft duty cycle of 0.20%.

Concluding Remarks

Although optimization of the hard duty cycle is not a requirement of the present study, the optimization techniques do present valuable insight into the tradeoffs between system parameters for systems of the type illustrated in Figure C. 3-8. The basic requirement for the present study is that hard limit cycle fuel consumption be less than or equal to the peak soft limit cycle fuel consumption for the maximum expected disturbance torque. Several interesting observations can be drawn as a result of the study of the system rate diagrams and phase planes:

For fixed system parameters and a hysteresis proportional to θ_d, hard limit cycle fuel consumption will <u>increase</u> with θ_d;

Conversely, in order to maintain a fixed hard limit cycle fuel consumption (duty cycle), the effective lead time constant must be increased as θ_d increases.

These observations, of course, apply only for a system which hysteresis is proportional to θ_d. It is interesting to note, however, that convergence to low duty cycle operation during initial acquisition will be more rapid for the larger lead required by increased θ_d.

REFERENCES:

1. Bi-Monthly Report No. 2, dated July 1965, "Solar-Powered Electric Propulsion Spacecraft.

2. S. Klein to R. J. McElvain, 2223/892, dated 8-4-65, "Conceptual Study of Mechanization for Thrust Misalignment Control-Mars Ion Engine Probe" HAC Memo

3. Bi-Monthly Report No. 1, dated May 1965, "Solar-Powered Electric Propulsion Spacecraft

4. "Rate Diagram Method of Analysis of an On-Off Control System," by H. Patapoff presented at the ARS Guidance and Control Conference, Stanford, California, August 1961

C. 4 Telecommunications

Emphasis in this study area during the last reporting period was directed to the exploration of telecommunication interface aspects of electric propulsion for the heliocentric transfer phase of the mission.

A contracted study conducted at HAC (Reference 1) in 1961 - 1962 indicated the following: little probability of degrading the downlink since the transmitter aboard the spacecraft would overpower all incidental noise; there would probably be no difficulty with the uplink if a contact-ionization type thrustor were used; and there was likely to be some constraint on the uplink with an electron-bombardment type thrustor.

In particular, expected and actual noise power spectra up to 1 kmc were reported, which indicated high noise generation at VHF (and hence in the IRIG VHF telemetry band).

The 1965 SERT I spacecraft (Reference 1) which used IRIG VHF telemetry frequencies reported no degradation of the downlink, but noted a somewhat degraded uplink, which, however, in the context of a near-earth telecom system was tolerable. The SERT data as reported are not sufficiently detailed to permit a quantitative determination of actual noise power (although this could presumably be reconstructed with access to NASA and RCA/Astroelectronics notebooks and calibration records); however, such information would cover a single frequency, and one which probably was not an optimum choice at that. NASA/Lewis had proposed that a wideband microwave radiometer be flown aboard SERT I to make a sensitive spectrum analysis in situs covering the frequency range to 1 kmc . To this end, an in-house development was in fact initiated at Lewis. Unfortunately, subsequent weight and flight schedule problems forced progressive cutbacks in this experiment, until only the VHF command receiver remained, resulting in the meager information derived from its (telemetered) AGC-bus voltage. Thus, on the basis of present data and in the context of a Mars mission, it appears that further investigation is warranted to assure that the uplink will remain operational to the desired range.

It is the consensus of opionion, at this time, that it is not possible to meaningfully simulate the noise mechanisms in a ground environment (such as a combination vacuum chamber plus shielded room), since ion thrustors in general and plasma oscillation frequencies in particular are highly sensitive to environment factors. Only a microwave radiomenter experiment flown aboard an ion-propelled spacecraft would provide the needed answers. Thus, on the basis of present data and in the context of a Mars mission, it seems dangerous to assume that the uplink will remain operational to the desired range without further experimental verification.

REFERENCES:

1. R. D. Wanselow and H. L. Wiser, "Investigation of RF Noise Genration from Space Vehicles," final report Contract NAS 8-862.

2. NASA Technical Memorandum, NASA TM X-1077, page 10.

C. 5 Structural and Dynamics Analysis

Two studies of spacecraft dynamics were completed during the report period. Both were restricted to the boost phase because the vibration environment during boost designs the sturcture.

The purpose of the first study were:

a. To estimate the axial and lateral deflections of the top of the spacecraft for shroud interference considerations.

b. To obatin a preliminary estimate of the maximum expected axial force, shear, and bending moments for a vehicle of this general shape.

c. To estimate the nature and magnitude of vibration coupling between the vehicle and the solar panels.

The results were used in both the Saturn/Centaur and Atlas/Centaur of the spacecraft design shown in Figures C. 5-1 and C. 5-2

The conclusions from the study were

a. The spacecraft sturcture should be designed so that its fundamental lateral frequency is as high as possible. This is to avoid both coupling with the booster and excessive deformation and thus possible interference problems.

b. Damping in the structure should be made as large as possible in order to avoid large deformations and thus large stresses induced by the vibration environment. Welded connections should be avoided if feasible. The possibility of providing artificial damping should not be overlooked.

c. The fundamental natural frequency of the stowed solar panels should be kept above 30 cps to avoid coupling with the spacecraft.

d. Care should be taken in the design of the bottom hinge point to avoid a resonant condition with the booster or spacecraft.

e. Additional care should be taken in the design so that the fundamental natural frequency of the spacecraft is not the same as the fundamental natural frequency of the booster system.

The second study analyzed the structural behavior of three alternate spacecraft designs that have been partially detailed. The first configuration shown in Figure C. 5-1 was exclusively a framed structure. The second configuration employed a combination of shell and frame structural elements, and it was assumed that the opening required for the ion engine exhaust was supported by a jettisonable panel. This configuration is shown in Figure C. 5-2. A third configuration investigated was a structure having the same strength and stiffness properties as the structure of Figure C. 5-2, with the exception that the ion engine exhaust opening remained unobstructed. To compensate for stiffness lost by removing the panel, additional bracing around the periphery of the opening was provided.

This table summaries the more significant results.

TABLE

	Structural Weight lbs.	Lateral Displacement 0 to peak, inches	Fundamental Frequency, cps
I	1325	3.0	9.5
II	1100	1.0	15.0
III	1580	1.0	15.0

Some observations resulting from the study are:

a. If the solar array were to have a fundamental frequency, in the stowed position, lower than about 15 cps, vibration coupling could occur between the spacecraft and the solar array resulting in possible damage to both.

b. The relatively low fundamental frequency of the frame is more likely to match a booster frequency at MACH 1 or maximum q. Severe aerodynamic disturbance could excite the boost vehicle which would in turn drive the spacecraft at its fundamental frequency resulting in larger stresses than have been predicted.

c. A smaller value of the fundamental frequency will result in a larger displacement in the upper part of the spacecraft.

d. The frame end connections or joints must be machined. The cost of manufacturing these should be considered.

e. The weight of the end connections will be a significant percentage of the total primary structure weight. It was assumed in the weight summary that the connection weight will be 50 percent of the weight of the tubes, based on Surveyor experience.

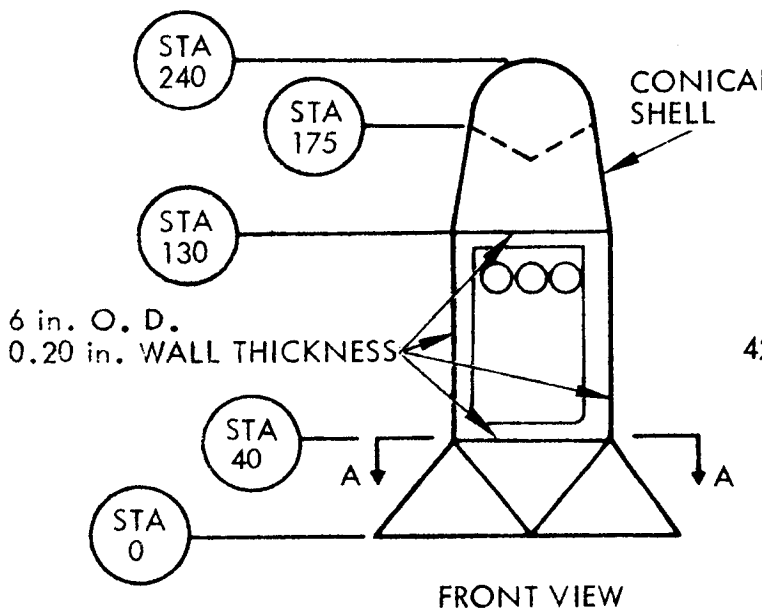

FRONT VIEW

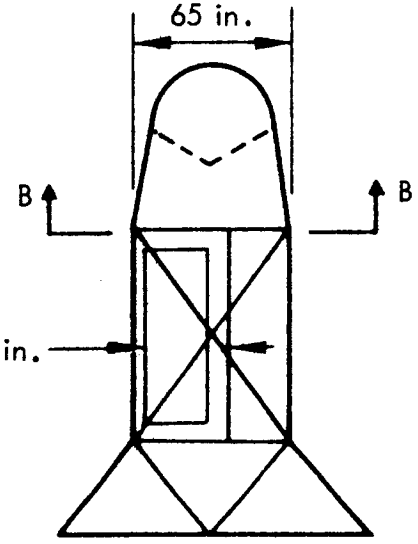

SIDE VIEW

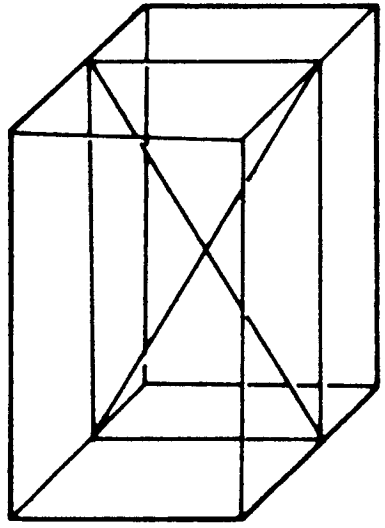

PICTORIAL VIEW OF BRACING BEHIND ENGINE BANK

ALL TUBES HAVE 4 in. O. D. AND 0.20 in. WALL THICKNESS EXCEPT THOSE NOTED.

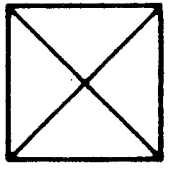

SECTION A-A

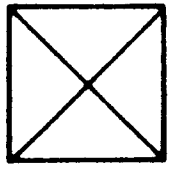

SECTION B-B

FIGURE C. 5-1 Framed Structure (all joints are rigid)

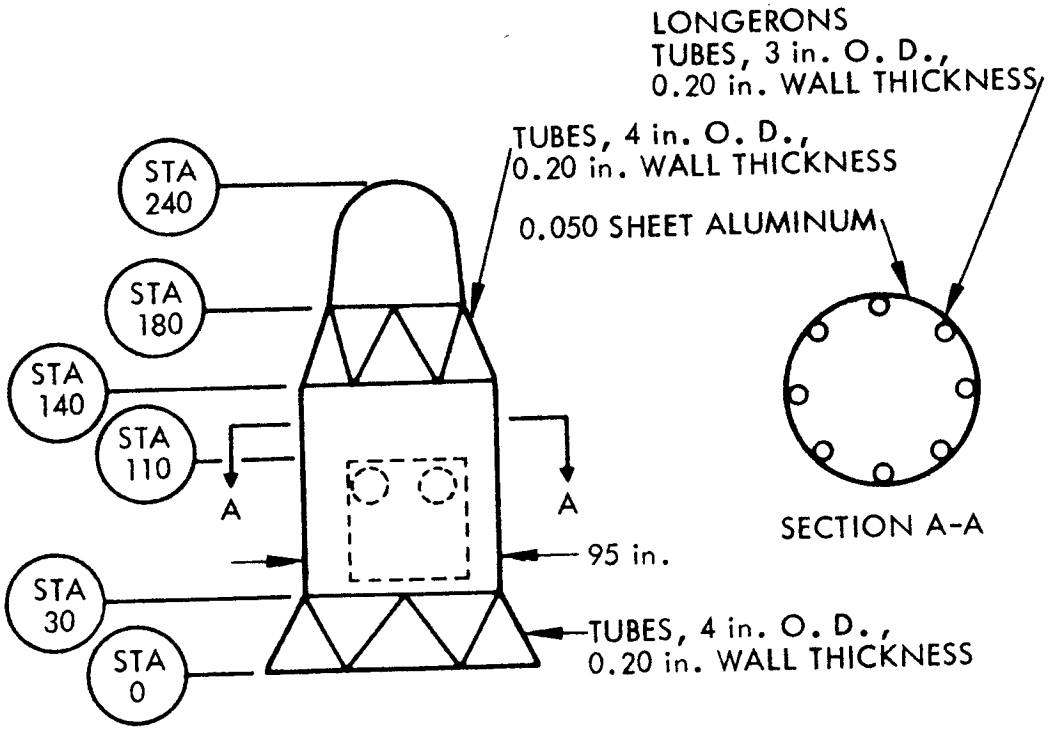

FIGURE C. 5-2 Combination Frame and Shell Structure

C. 6 Systems Integration

The effects of design of the various subsystems on the spacecraft are now quite clearly understood. Current status of the spacecraft system is briefly discussed below in relation to specific subsystems.

a. Control System

Analysis has shown that several types of control systems are feasible for this vehicle. The particular type or combination of types chosen therefore depends primarily on reliability and secondarily on weight. Accordingly, a comparative reliability study of the several control systems and combinations thereof is being undertaken.

At present the most attractive arrangement appears to be a combination with primary attitude control during the transfer phase by means of engine translation and cold gas control available as a back-up. However, one unresolved problem remains concerning use of engine motion for primary control. This is the distance the engine must move. The distance is determined by the probability of failure of thrustors. The maximum required motion would be 21 inches (the diameter of one engine) with the current thrustor configuration. The probability of occurrence of a combination of thrustor failures that could produce this is small. If the probability were significant there would be a problem of holding engine control motion tolerances when used as a primary control.

The question of how many nitrogen tanks are needed for reliability has arisen. The failure probability of a tank due to weak construction must be considered very close to unity. A puncture by a meteorite very likely would case an explosion, so that two tanks would be less reliable than one tank. The main source of failure in the gas system lies in the valves. By means of redundant plumbing design, the gas system can be so arranged that in case of a leak, a pressure detector would cause sealing of that outlet and opening of an alternate outlet.

A comparison of the above arrangement with a control system similar to Mariner 4 will be made on a reliability basis.

The spacecraft in its present form is desinged to carry a complete duplicate nitrogen gas control system.

b. Structure and Dynamics

A rather thorough dynamic analysis of two quite different structural arrangements of the spacecaft has shown the feasibility of vehicles of these types from the viewpoint of structural dynamics. According to the computer results both versions of the structure were stressed within acceptable limits and deflections under boost conditions remained within shroud limits. Structural weight of both designs was less than 12% of total spacecraft weight.

The one remaining possible problem with vehicle dynamics concerns interaction between the solar panels and control system. The amount of interaction depends on the type of control system finally chosen, i.e., control forces applied out on the solar panels or control of thrust line, and on the time constants of the control circuit. Three factors militate against any difficult problem arising here. 1) The ratio of lowest panels vibration frequency to vehicle limit cycle control frequency is currently about 30:1 for the cold gas system. 2) This ratio can be varied over a large range by changing control system time constants and design, with no resultant degradation in spacecraft performance. Hence the effective gain on solar panel vibration in its lowest mode can be maintained arbitrarily small. Therefore destabilizing influences can also be maintained negligible. Higher frequency panel vibration modes are so far removed from control system frequencies as to cause no concern. 3) Magnitude of the control forces is so small that the deflection of the solar panel tips due to application of a control jet thrust is less than 0.1 inches. The resulting angular deflection is well below reference instrument sensitivity.

c. Thermal Control

With one exception, no special thermal control problems were anticipated, hence detailed analysis in this area awaited the establishment of final design specifications. With final approval of the design specifications, the thermal studies were initiated and include the following:

a. Design of radiators to dissipate the heat generated by the power conditioning equipment.

b. Comparison of methods of maintaining heat balance within the vehicle as distance from the sun increases.

c. Determination of method of thermal control during engine-off condition,

d. Determination of the method of thermal control of the landing capsule, canopus tracker, retro motor, and other critically temperature sensitive components of the spacecraft.

The exception mentioned above is the problem of mounting the ion engine cluster (mercury pool cathode version) on the spacecraft so that heat generated within the engine can be removed without penalizing the available internal volume. Calculations indicated that it is feasible from the temperature control viewpoint to either cool the engines by direct radiation from the rear or sides of the engine cluster, or to conduct the heat from the engines to the spacecraft shell and let the spacecraft shell radiate to free space. The latter alternative presents the problem of electrical isolation of the engines. Configuration investigations indicated that radiating out the sides of the engine cluster proved to be the most attractive alternate from general arrangement considerations and this thermal control method will be incorporated into the final spacecraft design.